

REPORT DOCUMENTATION PAGE

Public reporting burden for this collection of information is estimated to average 1 hour per response, including the time for reviewing data needed, and completing and reviewing this collection of information. Send comments regarding this burden estimate or any other burden to Department of Defense, Washington Headquarters Services, Directorate for Information Operations and Reports (0704-4302). Respondents should be aware that notwithstanding any other provision of law, no person shall be subject to any penalty for failing to provide valid OMB control number. PLEASE DO NOT RETURN YOUR FORM TO THE ABOVE ADDRESS.

AFRL-SR-AR-TR-05-

0056

; the
ing
2-
ently

1. REPORT DATE (DD-MM-YYYY) 30 October 2004		2. REPORT TYPE Final		4/01/01 - 9/30/04	
4. TITLE AND SUBTITLE Investigation of Adhesive Joints for Nano-Engineering And Modeling				5a. CONTRACT NUMBER	
				5b. GRANT NUMBER F49620-01-1-0318	
				5c. PROGRAM ELEMENT NUMBER	
				5d. PROJECT NUMBER	
				5e. TASK NUMBER	
				5f. WORK UNIT NUMBER	
7. PERFORMING ORGANIZATION NAME(S) AND ADDRESS(ES) South Dakota School of Mines and Technology 501 E. Saint Joseph St. Rapid City, SD 57701				8. PERFORMING ORGANIZATION REPORT NUMBER	
9. SPONSORING / MONITORING AGENCY NAME(S) AND ADDRESS(ES) Charles Y-C Lee AFOSR/NL, 4015 Wilson Blvd Room 713 Arlington, VA 22203-1954				10. SPONSOR/MONITOR'S ACRONYM(S)	
				11. SPONSOR/MONITOR'S REPORT NUMBER(S)	
12. DISTRIBUTION / AVAILABILITY STATEMENT Approve for Public Release: Distribution Unlimited					
13. SUPPLEMENTARY NOTES					
14. ABSTRACT This report discusses the aluminum/epoxy interface effects on the global performance of aluminum adhesive joints. Four areas have been discussed: evaluation of the reliability of finite element analysis (FEA) on fracture mechanics, nano-indentation and FTIR tests for aluminum/epoxy interface properties, and FEA models including the interface effects. The reliability of FEA fracture mechanics analysis was studied by comparing the FEA results and the theoretical results of the energy release rate for a crack in a rectangular bar. Two kinds of FE analysis were performed: the Virtual Crack Closure method and the J-Integral method; both report accurate results. Nano-indentation tests were performed with an Interfacial Force Microscope (IFM) and Fourier Transform Infrared (FTIR) tests were performed to interpret the physical meaning of the IFM results. The test results show that the elastic modulus of epoxy changed gradually around the interface, probably due to cure history. The gradually changing elastic modulus was then introduced into FEA models. The results show that the interface effects on the energy release rate of the whole aluminum adhesive joint are significant. It is thus necessary to take the interface effects into consideration in joint design. Finally, different adhesive modulus designs were examined as promising alternatives to current configurations.					
15. SUBJECT TERMS adhesive joints, finite element analysis (FEA), fracture mechanics, nano-indentation					
16. SECURITY CLASSIFICATION OF:		17. LIMITATION OF ABSTRACT	18. NUMBER OF PAGES	19a. NAME OF RESPONSIBLE PERSON C. H. M. Jenkins	
a. REPORT	b. ABSTRACT	c. THIS PAGE	179	19b. TELEPHONE NUMBER (include area code) 605-394-2406	

Final Report

INVESTIGATION OF ADHESIVE JOINTS FOR NANO-ENGINEERING AND MODELING

AFOSR Award no. F49620-01-1-0318

Christopher H. M. Jenkins, Ph.D., P.E.
Professor, Mechanical Engineering Dept.
South Dakota School of Mines and Technology
501 E. Saint Joseph St.
Rapid City, SD 57701
(605) 394-2406 (voice); (605) 394-2405 (fax)
christopher.jenkins@sdsmt.edu
Compliant Structures Lab: www.compliantlab.sdsmt.edu
Mechanics/Materials/Design: <http://mmd.sdsmt.edu>

Robb M. Winter, Ph.D.
Camille and Henry Dreyfus Scholar
Chair, Department of Chemistry and Chemical Engineering
Co-Director Polymer Technology, Processing, and Composites Laboratory
Professor of Chemical Engineering
Department of Chemistry and Chemical Engineering
South Dakota School of Mines and Technology
501 East St. Joseph Street
Rapid City, SD 57701-3995
605-394-1237 (Voice)
605-394-1232 (FAX)
robb.winter@sdsmt.edu
<http://www.sdsmt.edu/mse/chemE/winter/index.htm>
<http://www.sdsmt.edu/mse/chem-che/chemE/reu/info.html>

October 30, 2004

20050223 181

ABSTRACT

This report discusses the aluminum/epoxy interface effects on the global performance of aluminum adhesive joints. Four areas have been discussed: evaluation of the reliability of finite element analysis (FEA) on fracture mechanics, nano-indentation and FTIR tests for aluminum/epoxy interface properties, and FEA models including the interface effects. The reliability of FEA fracture mechanics analysis was studied by comparing the FEA results and the theoretical results of the energy release rate for a crack in a rectangular bar. Two kinds of FE analysis were performed: the Virtual Crack Closure method and the J-Integral method; both report accurate results. Nano-indentation tests were performed with an Interfacial Force Microscope (IFM) and Fourier Transform Infrared (FTIR) tests were performed to interpret the physical meaning of the IFM results. The test results show that the elastic modulus of epoxy changed gradually around the interface, probably due to cure history. The gradually changing elastic modulus was then introduced into FEA models. The results show that the interface effects on the energy release rate of the whole aluminum adhesive joint are significant. It is thus necessary to take the interface effects into consideration in joint design. Finally, different adhesive modulus designs were examined as promising alternatives to current configurations.

TABLE OF CONTENT

- 1 SIGNIFICANCE OF ADHESIVELY BONDED JOINTS**
 - A. Introduction to Bonded Joints
 - B. Advantages of Adhesive Joints
 - C. Disadvantages of Adhesive Joints
- 2 RESEARCH OBJECTIVES**
- 3 LITERATURE SURVEY**
 - 3.1 INTRODUCTION
 - 3.2 DESIGN PARAMETERS OF ADHESIVE JOINTS
 - A. Visco-Elasticity of Adhesive
 - B. Behavior of composite adherends
 - C. Effects of bond defects
 - D. Fatigue
 - E. Simplified FEA Elements
 - F. Moisture and Temperature Effects
 - 3.3 FRACTURE MECHANICS
 - 3.4 NEW DESIGN OF ADHESIVE JOINTS
 - 3.5 INTERFACIAL FORCE MICROSCOPY (IFM)
 - 3.6 Fourier Transform Infrared Spectroscopy (FT-IR)
 - A. Fundamental Working Principle of FT-IR
 - B. FT-IR Microsampling Techniques
 - 3.7 NANO-CLAY/EPOXY COMPOSITE ADHESIVE
 - A. Structures of Clay

- B. Reaction Routes in Layered Polysilicates
- C. Intercalation of Kaolinite
- D. Intercalation Property of Layered Double Hydroxide (LDH)
- E. Types of polymer-clay nanocomposites

4 THE LAYER MODEL FOR COMPOSITE MATERIALS

- 4.1 VALIDATION OF THE LAYER MODEL
- 4.2 NECESSITY OF LAYER MODEL
- 4.3 THEORY OF THE ITERATIVE METHOD TO SOLVE THE LOCAL MATERIAL PROPERTIES IN COMPOSITE
- 4.4 STEPS OF THE ITERATIVE METHOD
 - A. Initial Values of Material Properties
 - B. Iterative Loop to Get the Accurate Material Properties
- 4.5 RESULTS OF THE ITERATIVE METHOD TO SOLVE THE LOCAL MATERIAL PROPERTIES IN COMPOSITE
- 4.6 LOCAL SHEAR MODULUS OF COMPOSITE MATERIALS
- 4.7 CONCLUSION

5 FRACTURE MECHANICS ANALYSIS FOR ADHESIVE JOINTS

- 5.1 STRESS DISTRIBUTION IN ADHESIVE LAYER OF SINGLE STRAP JOINTS
- 5.2 MESH DENSITY SENSITIVITY STUDY OF FEA FRACTURE MECHANICS
 - A. Model of Rectangular Bar
 - B. Model of Single Strap Adhesive Joint
- 5.3 EFFECTS OF EXTERNAL CRACKS ON THE SINGLE STRAP JOINT

- A. Effects of the Initial External Crack Directions
- B. Effects of initial crack lengths and positions

5.4 EFFECTS OF INTERNAL CRACKS ON SINGLE STRAP JOINTS

- A. Effects of the Initial Internal Crack Directions
- B. Effects of initial crack lengths and positions

5.6 CONCLUSION

6 EFFECTS OF ADHESIVE/ADHEREND INTERFACE

6.1 NANO-INDENTATION TESTS FOR ADHESIVE JOINT SAMPLE

- A. Experiments
- B. Nano-Indentation Test Results and Discussion

6.2 FT-IR ANALYSIS FOR ALUMINUM/EPOXY ADHESIVE JOINTS

- A. Preparation of Temperature Gradient Cured Samples
- B. FT-IR Microspectroscopy Results

6.3 FEA ANALYSIS INCLUDING INTERFACE PROPERTIES

- A. Step Representation of Elastic Modulus Distribution across Adhesive Layer
- B. FEA Modeling for External Parallel Crack
- C. FEA Modeling for Internal Parallel Crack

6.4 CONCLUSION

7 NANO-ENGINEERED ADHESIVE JOINTS DESIGNS

7.1 CLOISITE® 30B ORGANIC NANOCLAY

7.2 MEAN FIELD METHOD TO CALCULATE EQUIVALENT MECHANICAL PROPERTY OF NANO-CLAY/EPOXY COMPOSITE SYSTEMS

7.3 LOW/HIGH/LOW 3 LAYERED ADHESIVE JOINT

- A. FEA Model in Simulating Low/High/Low 3 Layered Adhesive Joint
- B. Experimental Test of Low/High/Low 3 Layered Adhesive Joint

7.4 LOADING DIRECTION DISTRIBUTED MODULUS (LDDM) ADHESIVE JOINTS

- A. Static Stress FEA for LDDM Joints
- B. Fracture Mechanics FEA for LDDM Joints

7.5 CONCLUSION

8 CONCLUSION

9 FUTURE WORK

10. ACKNOWLEDGEMENT

REFERENCES

APPENDIX

1 SIGNIFICANCE OF ADHESIVELY BONDED JOINTS

A. Introduction to Bonded Joints

The joining of composite materials or metals is essential for most structures. At the same time, joints often have lower strength than the bulk material and lead to stress concentration. There are mainly two kinds of joining methods: mechanically bonded joints and adhesively bonded joints. Mechanically bonded joints are bonded using mechanical methods, such as rivets or bolts; adhesively bonded joints (also called simply adhesive joints) are bonded using an adhesive layer. An adhesive joint is a structure in which two or more materials are solidly and permanently assembled using an adhesive.

B. Advantages of Adhesive Joints

Compared with mechanically bonded joints, adhesive joints have advantages as follows:

- (a) less weight
- (b) more uniform stress distribution
- (c) better aesthetics
- (d) lower production cost

Low weight is especially important for airplane structure, because the joint weight affects not only the fuel efficiency, but also the balance of the airplane. Traditionally, engineers have used mechanical joining in the manufacture of new airplanes, but the situation is changing. Klenner^[1] points out that it is because of the wide use of composite materials that the airbus A380 can be so fuel efficient, and adhesive joining is one of the key technologies which made the wide use of composite materials possible. The A380 is the only type of airplane that can fly from Singapore to Los Angeles without stopping. As gas prices go up, airline companies have a strong interest in such technology. Adhesive joints have already been widely used in light airplanes. Figure 1

shows a photo of ultra light, two-seat DEKO.5 airplane with a composite fuselage adhesively joined [2].

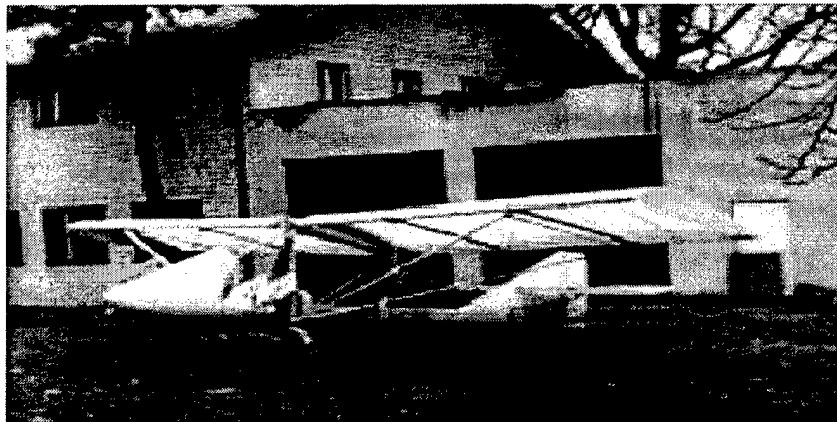


Figure 1. Ultra-light, two-seat DEKO.5 airplane [2].

C. Disadvantages of Adhesive Joints

The most serious disadvantage of adhesive joints is the prediction of their reliability. There are many factors that can affect the performance of polymer adhesives: temperature, sunlight, moisture, and environmental chemicals can cause fatigue and aging; load and temperature can affect viscoelasticity and polymer mechanic properties. Lack of predictability makes engineers hesitant to use adhesive joints in important cases. For example, in the airplane industry, where low weight should be very necessary, they use mechanically fastened joints (rivets) to bond different aluminum plates in building new airplanes. Although mechanical bonding usually has a serious stress concentration, some designers prefer this way because the properties and mechanical behaviors of metals are well determined. Correspondently, some design parameters for adhesive bonding are not yet fully developed.

2 RESEARCH OBJECTIVES

The factors in determining the useful life of adhesive joints are mainly ductile adhesive response, effects of composite adherends, bond defects, fatigue, simplified FEA elements for adhesive joint model, visco-elasticity, load rate, and the effects of moisture and temperature. There are already many reports on the effects of joint geometries, load rate, aging and fatigue, visco-elasticity and temperature and moisture constant. This dissertation focuses on the interface effects and nano engineering design for adhesive joints. The aim of this research is to improve the reliability of adhesive joints. This research contains two sections: 1. detailed finite element (FE) simulations including interface effects are carried out to achieve a more accurate analysis; 2. nano-scaled material design was applied for adhesive joints to improve the performance of adhesive joints.

In this research, Interfacial Force Microscope (IFM) was used to detect the local material properties, especially the properties close to the interfaces. Fourier Transform Infrared (FTIR) Spectroscopy was applied to detect the local chemical distribution. The performance of adhesive joints was characterized using standard test methods. The finite element analysis software used in this research was ABAQUS and FEMAP. This research was performed co-operatively with Chemistry and Chemical Engineering Department. Nano indentation, FTIR testing and manufacture of nano-clay reinforced adhesives were carried by the Chemistry and Chemical Engineering Department.

3 LITERATURE SURVEY

3.1 INTRODUCTION

There are different types of adhesively bonded joints in practice use. Some typical bonded joint configurations are shown in Figure 2. Among these adhesive joints, tapering of the adherends (Figure 2 – Joint (c) and (d)) can reduce peeling stresses. Madenci et al.^[3] studied the effects of fillets with different angles. It was proved that a smaller angle fillet could reduce the stress concentration more effectively. Scarf joints (Figure 2 – Joint (h)) are theoretically the most efficient, having the potential for complete elimination of stress concentrations. In theory, any desirable load capability can be achieved in the scarf joints by making the joint long enough and thick enough. However, practical scarf joint may be less durable because of a tendency toward creep failure. Step joints (Figure 2 – Joint (g)) represent a practical solution to the challenge of bonding thick members. These types of joints provide manufacturing convenience by taking advantage of the layered structure of composite laminates. Joints (a), (b), (e), and (f) are the least efficient joint types, but they are usually low cost in manufacturing. They are suitable primarily for thin structures with low running loads (load per unit width).

This research specially focuses on Joint (a), single strap joint, and Joint (b), double strap joint. This is because Joint (a), single strap joint, is the model to simulate crack repairing, and Joint (b), double strap joint, is a kind of typical adhesive joints with a wide use. It was used in this research for establishing a suitable material model for composite adherends in adhesive joint structures.

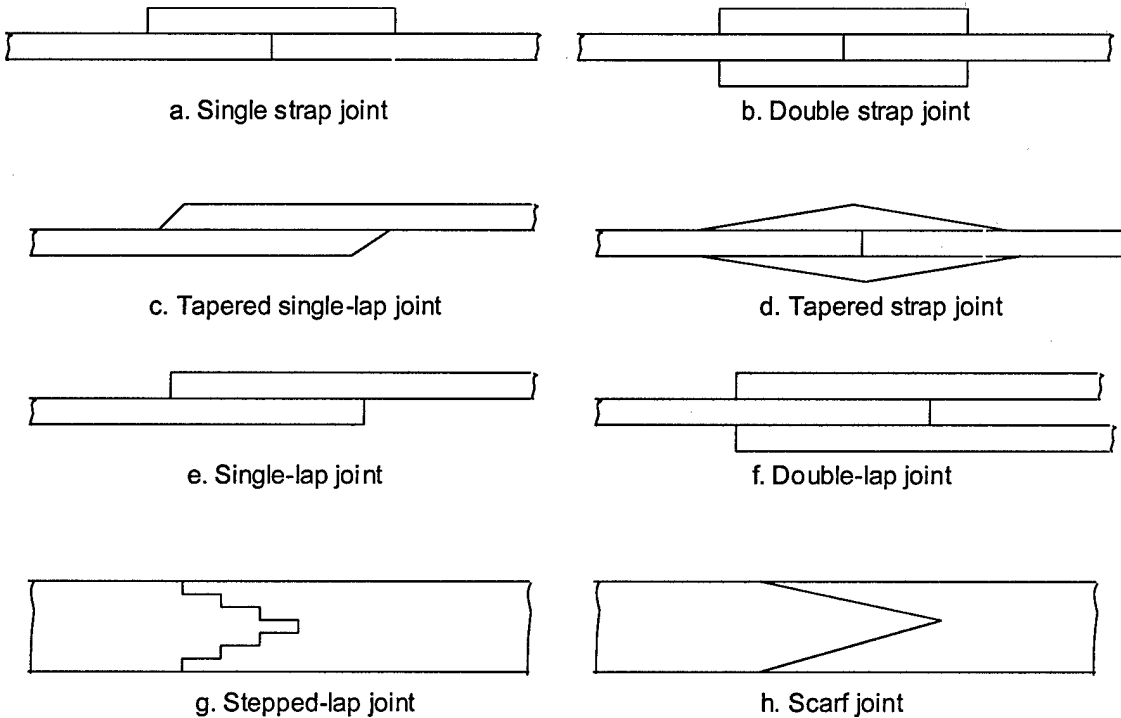


Figure 2. Typical adhesive joints ^[4, 5].

There are three basic approaches to analyze adhesive joints: experimental analysis, closed-form and finite element solutions. Experimental analysis characterizes the strength and life time of adhesively bonded using direct experiments, such as tensile tests, shear tests, creep tests, fatigue tests, etc. Experiment can provide the most reliable results, but it is also expensive. In the closed-form approach, a set of differential equations and boundary conditions is formulated. The solutions of these equations are analytical expressions which give values of stresses at any point of the joint. This approach is low cost, but difficult to be used for complex geometry. In the finite element analysis approach, solutions of differential equations are obtained by numerical methods. Consequently, no general expressions are obtained for the solution, and, stresses are given at specific points, such as Gauss points. Finite element analysis is more expensive than the closed-form approach, but much cheaper than the experimental analysis method. Its accuracy is

relatively high and suitable for complex geometry structures. Because of these merits, Finite Element Analysis (FEA) becomes more and more popular in adhesive joint design. The rapid development of computers has also made the use of FEA more appealing and feasible. The method used in this research is a combination of finite element solution and experimental test methods together, which can achieve reliable analysis results at a relatively low cost.

2.1 DESIGN PARAMETERS OF ADHESIVE JOINTS

There are many articles studying different design parameters of adhesive joints, such as ductile adhesive response, effects of composite adherends, bond defects, fatigue, simplified FEA elements for adhesive joint model, visco-elasticity, and the effect of moisture and temperature. FEA is a powerful tool in studying the effects of multiple design parameters.

A. Plasticity of Adhesive

The plasticity of adhesive is important for stress analyses design of adhesive joints because it is a key factor in minimizing the adverse effects of shear and peel stress peaks in the bond layer. If peel stresses can be eliminated from consideration by such approaches as adherend tapering, strain energy to failure of the adhesive in shear has been shown by Hart-Smith^[6] to be the key parameter controlling joint strength. The square root of the adhesive strain energy density at failure determines the maximum static load that can be applied to the joint. The work of Hart-Smith has also shown that for predicting mechanical response of the joint, the detailed stress-strain curve of the adhesive consists of a linear rise followed by a constant stress plateau, that is a plastic response. Once the equivalent elastic to plastic stress-strain curve has been identified for the selected adhesive in the range of the most severe environmental conditions (temperature and humidity) of interest, the joint design can proceed through the use of relatively simple one-dimensional stress analysis. This research provided a method to make adhesive joint design

using closed form calculations. Even the most complicated joints, such as the step lap joints designed for root-end wing and tail connections for F-18 and other aircraft, have been successfully designed using this method [7-9].

Plasticity is not included in the calculation of our research because our research focuses on fracture mechanics, not stress analysis. The effects of plasticity have already been taken into account by determining the fracture toughness.

B. Visco-Elasticity of adhesive

Visco-elasticity is the tendency of plastics to respond to stress as if they were a combination of elastic solids and viscous fluids. This property, possessed by all plastics to some degree, dictates that while plastics have solid-like characteristics such as elasticity, strength and form stability, they also have liquid-like characteristics such as flow depending on time, temperature, rate and amount of loading [10]. In many cases, it can't be ignored.

With the development of computer technology and FEA software, visco-elasticity can be studied more accurately using FEA method. Roy and Reddy [11] modeled adhesive joints based on Schapery's non-linear viscoelastic constitutive equation for the adhesive. They also used a non-linear generalized Fickean diffusion model and an updated Lagrangian formulation of a two-dimensional stress state. They pointed out the effect of moisture diffusion, and the coupling between moisture concentration and dilatational strains, on stress distributions in bonded joints should not be ignored. Yadagiri et al. [12] presented a direct formulation using Prony series for the visco-elastic analysis of adhesive joints. They also developed a six-noded quadratic isoparametric element.

Usually, visco-elasticity can be modeled using Prony series. It is assumed that relaxation shear modulus can be expressed as:

$$G(\tau) = G_\infty + \sum_{i=1}^n G_i e^{-\tau/\tau_i} \quad (1)$$

where $G(\tau)$ is relaxation shear modulus, a function of time (τ). G_∞ is the long-term shear modulus, τ_i is the relaxation time, and G_i the relaxation modulus of term i . G_∞ , τ_i and G_i can all be determined from the creep test curve. n is decided by the accuracy desired.

In our research, visco-elasticity is not included. There are two reasons allowing us to do this:

(1) our design is based not on stress analysis, but energy release rate from fracture mechanics analysis; (2) visco-elasticity is not significant for highly cross-linked adhesives at room temperature.

C. Behavior of composite adherends

Polymer matrix composite adherends are affected by interlaminar shear and peel stresses, so there is a need to account for such effects in stress analysis of joints. Transverse shear and through thickness deformations of the adherends have an effect analogous to the bond layer, corresponding to a lowering of both shear and peel stress peak. At the same time, the adherend matrix is often weaker than the adhesive. Visco-elastic behavior of the adherend matrix is similar to that in the adhesive.

The effect of the stacking sequence of the laminates making up the adherends in composite joints is significant. For example, 90° layers, which is in the transverse direction of the loading direction, placed adjacent to the bond layer theoretically act largely as additional thickness of adhesive, leading to lower peak stress. While 0° layers (in the loading direction) next to the bond layer give stiffer adherend response with higher stress peak. In practice, it has been observed that 90° layers next to the adhesive layer tend to seriously weaken the joint because of transverse cracking [13].

D. Effect of bond defects

Defects in adhesive joints include surface preparation deficiencies, voids and porosity, and thickness variations in the bond layer.

Of the various defects which are of interest, surface preparation deficiencies are probably the greatest concern. These are particularly troublesome because there are no current nondestructive evaluation techniques that can detect low interface strength between the adhesive and the adherends. Most joint design principles assume good adhesion between the adherends and adhesive. Hart-Smith, Brown and Wang [14] gave an account of the most crucial features of the surface preparation process. They suggest that the surface preparation which is limited to removal the surface layer of adherends may be suspect.

Porosity is usually associated with over-thickened areas of the bond, which tends to occur away from the ranges where most of the load transfer takes place, and thus has relatively small effect, especially if peel stresses are minimized by adherend tapering. Hart-Smith^[15] indicates that in such case, porosity can be represented by a modification of the assumed stress-strain properties

of the adhesive as determined from thick-adherend tests. If the peel stresses are significant, as in the case of over-thick adherends, porosity may grow catastrophically.

In the case of bond thickness variations, these usually take place in the form of thinning due to excess resin bleed at the joint edges, leading to overstressing of the adhesive in the vicinity of the edges. Tapering the adherends at the joint edges can be used to compensate for this condition [16]. Common practice involves the use of film adhesives containing scrim cloth, which helps to maintain bond thickness. It is also common to use mat carriers of chopped fibers to prevent a direct path for access by moisture to the interior of the bond.

E. Fatigue

Fatigue is an important field for adhesive joints. Romanko and Jones [17] did fatigue tests of single lap joints under several different loads, frequencies, humidities and temperatures revealing damage initiating in the high stress regions as interface cracks with plane crazing. They concluded that the fatigue effects in adhesive joints are significant. Reedy and Guess [18] used both finite element analysis and experimental analysis to study tubular lap joints. They found that measured fatigue resistance is a strong function of the applied load. Bassler et al. [19] used both finite element analysis and experimental analysis to evaluate the effects of adhesive type, bondline thickness, steel gauge and type, and environmental exposure on the adhesive's strength. They concluded that usually adhesive joints are safe and reliable for vehicle use and adhesive joints can reduce the noise levels of a vehicle body structure. Imanaka et al. [20] applied cyclic tensile fatigue tests on adhesively bonded butt and scarf lap joints with different lap length and adhesive layer thickness. They found that fatigue strength of lap joints evaluated from the

maximum tensile stress of the adhesive layer agrees with the fatigue strength of adhesively bonded butt joints of thin wall tubes under cyclic tensile load conditions.

The researches above show that fatigue is a complex problem for adhesive joints. It is a function of load, moisture, temperature, bondline thickness, the geometry of adhesive joints, and time.

F. Simplified FEA Elements

Detailed FEA models are expensive and time consuming, especially for dynamic analysis. Some researchers developed special element types to elevate the FEA efficiency. Romanko and Jones [21] developed a three-element linear viscoelastic model for the adhesive behavior. Kim and Griffin [22] used special finite elements (composite elements and joint elements) and the modal strain energy method to calculate the loss factor for each vibratory mode of interest. The special element represents a section of the composite beam or the overlap joint as an element with four nodes. Its properties were calculated by using a generalization of the shape function concept in the special elements. The resulting special element has only a small number of degrees of freedom but accurately represents the geometrically complex substructure. Habib et al. [23] suggested axisymmetric interface finite elements, which take into account the interface conditions due to geometrical continuity and interface equilibrium. This research provided a method to simulate imperfect interfaces in FEA models.

Static mechanical analysis is the main part of our research, and the high performance personal computers available today are already powerful enough for our research purpose. At the same time, our research focuses on the effects of adhesive/adherend interfacial properties. We prefer to use a widely-accepted FEA method to avoid possible argument. Thus we have used 2-

dimensional continuum FE elements in the ABAQUS code without any simplification in our research.

G. Moisture and Temperature Effects

Large disparity of thermal expansion characteristics between the adhesive and the metal or composite adherends can lead to severe problems. Adhesives with high curing temperature may be unsuitable for some use below room temperature because of large thermal stresses which develop as the joint cools below the fabrication temperature.

Composite adherends are relatively sensitive to moisture, which is not a problem for metal adherends. As a result, response of the adhesive to moisture maybe a significant issue for composite joints.

The effects of moisture and temperature on adhesive joints are a relatively new field of study. Roy and Reddy ^[24] studied the effect of temperature and stress level on the visco-elastic response by a nonlinear shift factor definition. This method studys the visco-elastic response under different temperatures by changing them into those under a standard reference temperature through multiplication by a non-linear factor. The reference temperature is usually the room temperature (25°C). They also considered penetration sorption effects using a nonlinear Fickean diffusion model in which the diffusion coefficient is dependent on the penetration concentration and the dilatational strain. Commercial FEA codes are limited in dealing with this complex situation. They developed a set of FEA code by themselves. Butkus ^[25] made a report on the aging experiments of three bonded aerospace material systems, two epoxies and one polyimide. The test data were analyzed using finite element programs and closed-form solutions.

Environmental exposure caused reductions in the failure strain, strength, and toughness of the adhesive specimens, and in the toughness and fatigue threshold of the bonded joint specimens. Specimens exposed under high temperature and humidity prior to testing and those tested at low temperatures indicative of high altitude operations experienced the most significant toughness losses. The fatigue crack growth rate sensitivity appeared to be unaffected by environmental exposure. Ashcroft et al. [26] tested the effects of environment on the fatigue behavior of carbon fiber reinforced plastics/epoxy (CFRP/epoxy) lap-strap joints. It was shown that the fatigue resistance of the lap-strap joints did not vary significantly until the glass transition temperature, T_g , was approached, at which point a considerable reduction in the fatigue threshold load was observed. It was noted that the absorbed moisture resulted in a significant reduction of the adhesive's T_g . Ashcroft et al. [27] analyzed the fatigue strength of adhesive joints using stress analysis and fracture mechanics. Non-linear stress and fracture analysis are performed in order to predict the strength of the joints in different hostile environmental conditions. The use of several threshold criteria was investigated. The plastic zone size does not show correlation at the fatigue threshold load in the different joint types, furthermore, elastic and elasto-plastic fracture parameters were calculated for two different inherent cracks. The results were satisfying. Criteria based on the principal stress can provide good threshold prediction for small plastic deformation. The maximum principal strain, von Mises strain, shear stress and von Mises stress predict with good accuracy the fatigue thresholds of the joints that undergo large plasticity.

Although there are some progresses in multiple parameter FEA analysis, it is still a difficult research area. Commercial FEA codes are limited in studying the co-effects of multiple

parameters. User-developed FEA codes or subroutines are usually necessary for research in this field.

3.3 FRACTURE MECHANICS

There are no perfect structures in reality, and to detect small cracks is not always easy. Once a crack comes into being, it would introduce significant stress concentration. The stress distribution would be greatly changed. In this case, the static analysis becomes unreliable, and fracture mechanics analysis is necessary. Another reason that makes fracture mechanics important in adhesive design is the phenomenon of free edge singularity in some types of adhesive joints. For example, using static, linear analysis, the theoretical results of peeling stress would go to infinity at the edge and the center for single-strap adhesive joint. FEA would not predict such infinite results, but the maximum stresses would be very sensitive to the mesh density.

Fracture mechanics analysis is an important method for the design of adhesive joints. There are many articles in this area. Nishioka and Atluri [28] presented a three-dimensional analysis of cracks in adhesively bonded laminates (single lap), with debonding around the crack. Effects of the several key parametric variations were studied: relative thicknesses of adhesives, relative material properties of adhesives and adherends, ratio of flaw length to laminate characteristic dimensions, and shape of debonded region. Their work provided a guideline in adhesive joints design. Kyogoku et al. [29] studied single lap joints, scarf joints and shaft joints. They found that the smaller the difference in the Young's moduli between the adherends, the greater was the joint strength. Sancaktar et al. [30] assume that crack propagation is constrained within the adhesive layer regardless of the loading orientation when they studied single lap joints. They considered

only the effects of peel and in-plane-shear stresses. Hufferd [31] pointed that thickness of bondline can not be ignored. He wrote a set of finite element analysis codes to consider the effects of (linear) visco-elastic adhesive behavior and geometric nonlinearities on the computed fracture behavior of a cracked lap shear (CLS) test specimen. Johnson and Mall [32] used both finite element analysis and experimental analysis to study cracked lap shear (CLS) specimens. They found that total strain energy release rate appeared to be the driving parameter for cyclic debonding and debond initiation in structural adhesives. Imanaka et al. [33] studied adhesive-bonded carbon fiber reinforced plastics (CFRP) pipe. They pointed out that the fatigue strength of the joint mainly depends on the maximum tensile stress normal to the adhesive/adherend interface at the lap end.

The research above indicates that in the failure and crack growth of adhesive joints, there are many important parameters to be consider, especially the bondline thickness and the difference in Young's moduli between adherends and adhesive.

3.4 NEW DESIGN OF ADHESIVE JOINTS

New design of adhesive joints is an effective method to improve the joints' performance. A common method is to introduce fillets at the ends of adherends. Madenci et al. [5] studied the effects of fillets with different angles. It was proved that a smaller angle fillet could reduce the stress concentration more effectively. Attachments were applied into single lap joints to the ends of the adherends by Sun et al. [34]. This was reported to be effective and it can turn the singular peel stress into compression. Sun also proposed a wavy single lap joint, in which the two adherends are aligned. It was reported that the stress concentrations at the ends of the adherends are reduced, the shear stress in the adhesive is more uniform, and the adhesive peel stress is

reduced [35-37]. Adams et al. inserted different films in the adhesive layer adhesive joints [38]. This method provided a good control of crack propagation direction inside of the adhesive layer.

Nano-scaled adhesive joints design is discussed in the present dissertation. This approach gives us an enlarged design freedom in adhesive joints design. Two new designs for adhesive joints, low/high/low layered and loading direction adhesive modulus distribution, will be given out in the following chapters.

3.5 INTERFACIAL FORCE MICROSCOPY (IFM)

Interfacial Force Microscopy (IFM) is applied in our research for nano-mechanics characterization. IFM is a scanning probe microscope developed at Sandia National Laboratories by Dr. Jack E. Houston [39]. The applied force in IFM is measured using a self-balancing differential capacitance sensor. An electrochemically sharpened tungsten tip is displaced relative to the sample at a given displacement rate by piezoelectric probe positioners, and the measured force is recorded as a function of displacement. The inchworm sample positioner can move 3-dimensionally. It allows IFM to detect the local mechanical properties for the region of interest. The structure of IFM is shown in Figure 3.

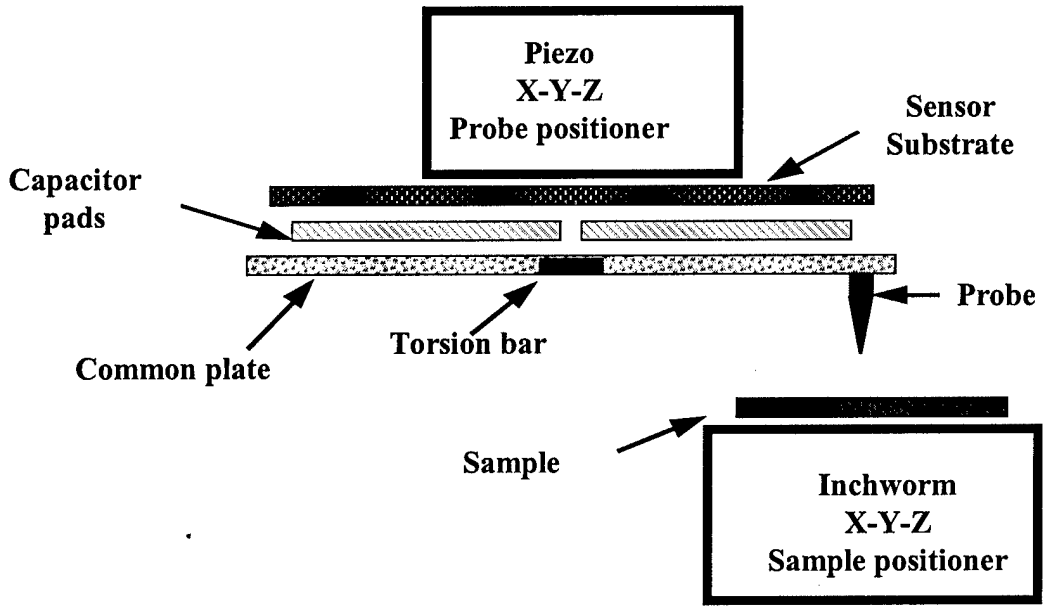


Figure 3. Structure of IFM.

In the process of detection, a force curve is produced, which is a plot of tip deflection as a function of the vertical motion of the scanner. This curve can be analyzed to provide information on the local mechanical response. The spring constant of the cantilever probe can be chosen such that small differences in response can be detected for polymers having a certain range of stiffness corresponding to the chosen spring constant. The advantage is that IFM makes it possible to achieve purely elastic deformation by applying penetration depths of only a few nanometers to tens of nanometers, which is small compared to the tip radius (ranges from 70 nm to 500 nm) of the tungsten probe. In this case, Hertzian contact mechanics can be applied to the loading curve or unloading curve, as has generally been done for indentation testing with the IFM^[40, 41]. Some characteristics data of IFM are listed in Table 1.

Table1 IFM sensor : Characteristics

Parameter	Value
Normal force sensitivity	1 nN to 400 mN
Feedback response time	500 sec
Image resolution	~ 100 Å
Lateral force sensitivity	2 nN to 50 mN

The analysis of indentation load-penetration curves produced by depth-sensing indentation systems is often based on work by Oliver and Pharr [42]. Their analysis was in turn based upon relationships developed by Sneddon [43] for the penetration of a flat elastic half space by different probes with particular axisymmetric shapes (e.g., a flat-ended cylindrical punch, a paraboloid of revolution, and a cone). In general, the relationships between penetration depth, h , and load, P , for such indenter geometries can be represented in the form

$$P = \alpha(h - h_f)^m \quad (2)$$

where α contains geometric constants, the sample elastic modulus, the sample Poisson's ratio, the indenter elastic modulus, and the indenter Poisson's ratio, h_f is the final unloading depth, and m is a power law exponent that is related to the geometry of the indenter; for a flat-ended cylindrical punch, $m = 1$, for a paraboloid of revolution, $m = 1.5$, and for a cone, $m = 2$. In applying Equation (1) to the calculation of modulus, Oliver and Pharr made two significant realizations. First, the slope of the loading and unloading curve change constantly due to a constantly changing contact area. In prior research, the high load portion of the unloading curve was

approximated as linear, which incorrectly assumes that the contact area remains constant for the initial unloading of the material. This practice created a dependence of calculated modulus values on the number of data points. Second, if the unloading curve can be fit by a power law expression (i.e., Equation (2)), then a derivative, dP/dh , applied at the maximum loading point (h_{max} , P_{max}) should yield information about the state of contact at that point. This derivative was termed the contact stiffness, S , and is given by

$$S = 2aE_r = \frac{2\beta}{\sqrt{\pi}} E_r \sqrt{A} \quad (3)$$

where a is the contact radius and A is the projected area of tip-sample contact. The reduced modulus, E_r , accounts for deformation of both the indenter and the sample and is given by

$$\frac{1}{E_r} = \frac{1 - \nu^2}{E} + \frac{1 - \nu_i^2}{E_i} \quad (4)$$

where E and ν are the sample elastic modulus and Poisson's ratio, respectively, and E_i and ν_i are the elastic modulus and Poisson's ratio, respectively, of the indenter material. β is used to account for the triangular and square cross sections of many indenters used in nanoindentation studies. For $\beta = 1$, the cross section of the indenter is assumed to be circular, as the contact radius, a , is replaced by $(A/\pi)^{1/2}$, and Equation (3) (with $\beta = 1$) is valid for any indenter that has a shape described by a solid body of revolution of a smooth function. However, the values of β , as determined by King [44] using numerical analysis, are only small corrections (e.g., $\beta = 1.034$ for a triangular punch) and are not often used in practice. Another correction factor has recently been

suggested due to unrealistic boundary conditions used by Sneddon [45]. This correction factor, γ , which depends upon the sample Poisson's ratio, ν , and tip geometry ranges from approximately 1.05 to 1.10 for ν between 0.1 and 0.4 and a conical indenter with an opening angle of 70.32° [41, 45].

3.6 Fourier Transform Infrared Spectroscopy (FT-IR)

A. Fundamental Working Principle of FT-IR

Fourier Transform Infrared spectroscopy is an important analysis technique for organic chemistry. It is an easy way to identify the presence of certain functional groups in a molecule. Also, one can use the unique collection of absorption bands to confirm the identity of a pure compound or to detect the presence of specific impurities.

The heart of most FT-IRs is a Michelson Interferometer. Its structure was shown in Figure 4. The function of an interferometer is to split a beam of light into two beams, and make one light beam travels a different distance from the other. The difference in distance traveled by these two light beams is called the optical path difference (or optical retardation), δ . The Michelson Interferometer consists four arms. The first arm is the source of infrared light, the second arm is a stationary (fixed) mirror, the third arm contains a moving mirror, and the fourth arm is open. The intersection of the four arms is a beam splitter. It can transmit half the radiation and reflect the other half part. After reflecting off their respective mirrors, the two light beams recombined at the beam splitter, then leave the interferometer to interact with the sample and strike the detector.

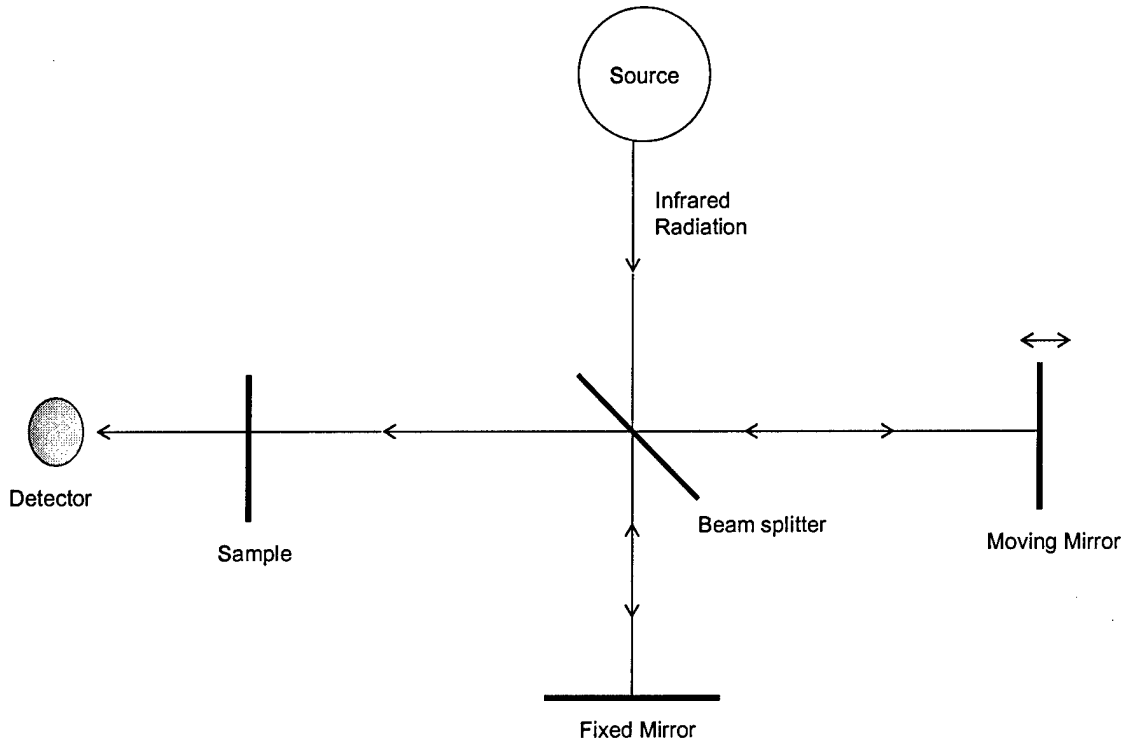


Figure 4. An optical diagram of a Michelson Interferometer. [46]

If the moving mirror and the fixed mirror have the same distance from the beam splitter, the optical path difference is zero, which is called zero path difference (ZPD). In a Michelson Interferometer, an optical path different is introduced between the two light beam by change the position of the moving mirror. The distance mirror move from ZPD is called the mirror displacement, Δ . The relationship between the mirror displacement and the optical path difference is

$$\delta = 2\Delta \quad (5)$$

When the two light beams come together, interference occurs. For monochromatic light beams with the light wave length of λ , if the optical path difference equal to multiples of λ , the amplitude of the combined lights is the sum of two separate light beams. That is called constructive interference. The condition for constructive interference is:

$$\delta = n\lambda \quad (6)$$

where n is any integer with the values $n = 0, 1, 2, 3\dots$. Correspondingly, for some other path distance, the amplitude of the combined lights is the difference between two separate light beams. That is called destructive interference. The condition for destructive interference is:

$$\delta = (n+1/2)\lambda \quad (7)$$

where n is any integer with the values $n = 0, 1, 2, 3\dots$. If the moving mirror is moved at constant velocity, the intensity of the radiation increases and decreases smoothly. The variation of light intensity with optical path difference is measured by the detector as a cosine wave. A plot of light intensity versus optical path difference is called an interferogram. To generate a complete interferogram, the moving mirror is translated back and forth once. This is known as a scan.

In practice, FT-IR uses not a laser, but a continuous infrared light source. So the interferogram obtained by an FT-IR is a combination of many cosine waves with different wave lengths. A Fourier transform is applied to transform the interferogram into a spectrum. When an interferogram is Fourier transformed, a single beam spectrum is obtained. It is a plot of raw detector response versus wavenumber ($1/\lambda$). A single beam spectrum obtained without a sample in the infrared beam is called a background spectrum. The background spectrum contains the instrument's and the environment's contribution to the infrared spectrum. It is called the instrumental response function. The overall shape of the background spectrum is determined by the sensitivity of the detector, transmission and reflection properties of the beam splitter, emissive properties of the source, and reflectivity of the mirrors. Common features around 3500 and 1630 cm^{-1} are due to atmospheric water vapor, and the bands at 2350 and 667 cm^{-1} are due to carbon dioxide. A background spectrum must always be taken when analyzing samples by FT-IR.

When an interferogram is measured with a sample, and Fourier transferred to a sample single beam spectrum, the instrumental and atmosphere contributions to the spectrum must be eliminated. So the sample single beam spectrum needs to be ratioed against the background spectrum. This produces a transmittance spectrum. The calculation is:

$$T = I/I_0 \quad (8)$$

where T is transmittance, I is intensity measured with a sample in the beam, and I_0 is intensity measured with no sample in the beam.

Then we get a spectrum of Transmittance versus Wavenumber. It is called transmittance spectrum. The absorbance spectrum can be calculated from the transmittance as following:

$$A = -\log T \quad (9)$$

where T is transmittance, and A is absorbance.

All materials consist of atoms. These atoms vibrate at specific natural frequencies. The vibrating frequencies are determined by the characters of the chemical bonds and their chemical environments. They can absorb energy from light if the light frequency equals the natural frequency of one of those vibrations. So the peaks in the absorbance spectrum (or the transmittance spectrum) correspond to specified vibrations of atomic bonds. By studying the peak position in a FT-IR spectrum, we can determine the chemical group existing in a material, and thus its structure.

Quantitative analysis can be carried according to the Beer's law:

$$A = \varepsilon lc \quad (10)$$

where A is absorbance, ε is absorptivity, l is pathlength, and c is concentration.

The molecule of interest is called the analyte. The height or area of a peak in an absorbance spectrum is directly proportional to the concentration of analyte in the infrared beam. In practice, the concentration of analyte is usually determined from the correlation between absorbance and concentration. To establish this correlation, the infrared spectra of samples that contain known analyte concentration are called standards. During the process called calibration,

a mathematical model is generated giving the correlation between absorbance and analyte concentration. Once an accurate model is established, the concentration in unknown samples can be predicted.

B. FT-IR Microsampling Techniques

With the rapid advances in manufacture technology, FT-IR combined with microscope sampling accessories came into being. During the later 1970s and early 1980s, a number of papers were published dealing with FT-IR microsampling technologies [47-50]. Unfortunately, micromanipulation techniques using a beam condenser were time-consuming and generally required skillful operators. These disadvantages were largely overcome by FT-IR microscope sampling technique, introduced in 1983. Since that time, the technique has found wide acceptance and has become the routine method for characterization and identification of samples available in pictogram quantities.

The first commercial FT-IR microsampling equipment was produced by BioRad Digilab Division (Cambridge, MA) since 1983. Now Analect, Bruker, Mattson, JEOL, and Jasco all have this kind of products. FT-IR microsampling techniques provide us a powerful tool for chemical structural analysis at specified locations in a material.

Figure 5 shows the schematic optical diagram of the BioRad Digilab Division microscope sampling for the reflection mode of operation. The microscope is at the top of the FT-IR sample compartment. The infrared beam from the FT-IR instrument is focused onto a sample placed on a standard microscope x-y stage. The infrared beam that was reflected from the sample was collected by a 36 \times Cassegrain objective. The objective produces an image of the sample within

the barrel of the microscope, and variable aperture (circular iris or circular diaphragm) is placed in this image plane. The radiation passing the aperture is focused on a small area ($250 \times 250 \mu\text{m}$) liquid nitrogen-cooled MCT (mercury cadmium telluride) detector by another $36 \times$ Cassegrain condenser. The microscope include a switchable $4 \times$ or $10 \times$ glass objective and a collinear visible illumination and observation system that can be used for the visual inspection of the sample. In experiment, the sample is first placed on the microscope stage, and the desired area of the sample is located using the low-power glass objective. The $36 \times$ Cassegrain objective is then switched into place and provides a total visual magnification of $360 \times$. The desired area on the sample image is optically equivalent to masking the sample with a pinhole. The result would be the spectrum of the desired part of the sample [51]. The sample stage can move 3 dimensionally. It allows FT-IR to detect the local chemical structures for the region of interest. The sampling area in our research is $20 \times 20 \mu\text{m}$.

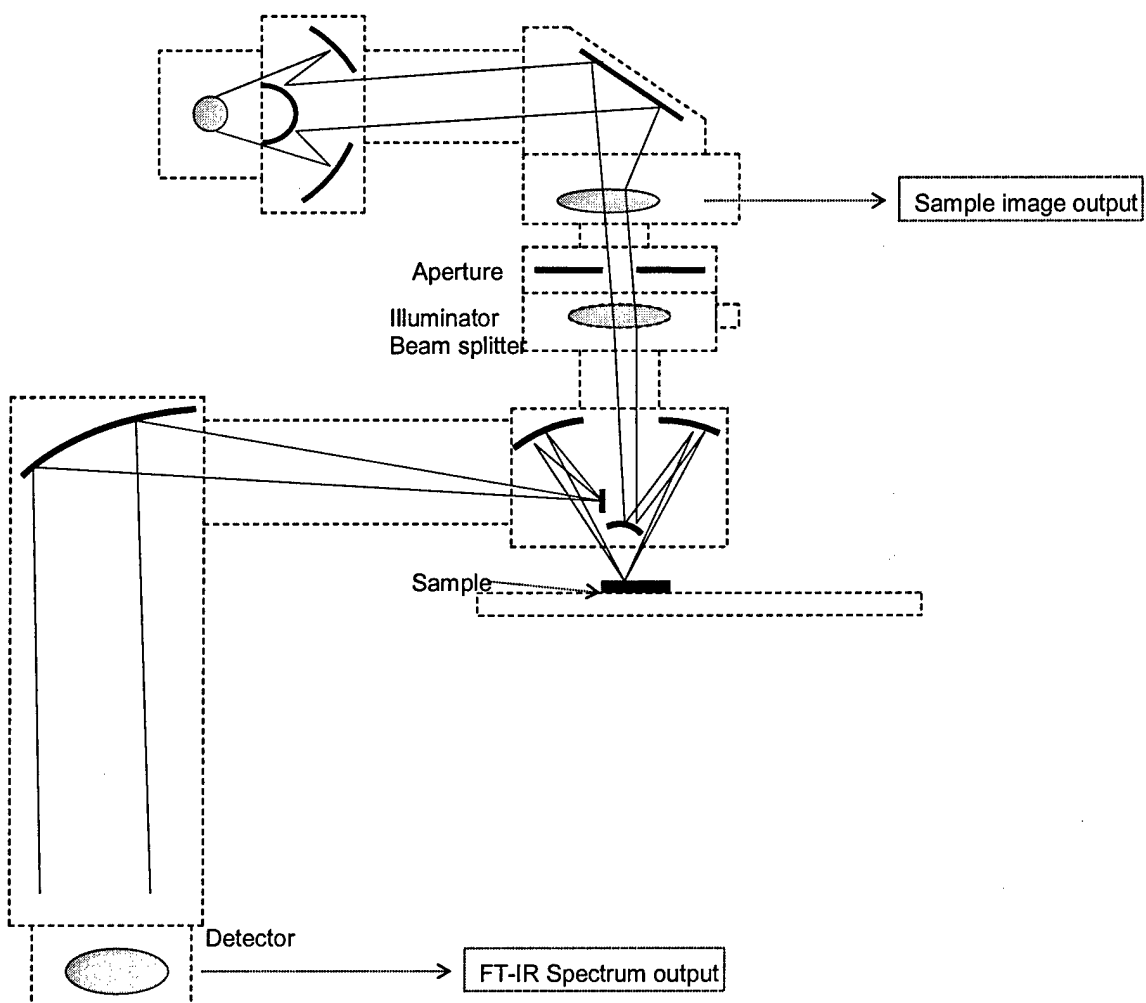


Figure 5. The optical system of the UMA-300A infrared microscope in the reflection mode of operation.

3.7 NANO-CLAY/EPOXY COMPOSITE ADHESIVE

Polymer/nano-clay composites are formed through the union of two very different materials with organic and mineral pedigree. Linus Pauling first elucidated the structure of clay minerals using X-ray crystallographic methods and thereby provide the basis for subsequent extensive study of these materials in the disciplines of colloid science, rheology, mineralogy , catalysis, tribology, civil engineering, ceramic engineering, and especially soil science. Clays, in particular, are

unique in the fact that they exist in nature and can be broken down into one nanometer thick platelets. They have many industry applications.

Polymer/nano-clay composites have their origin in the pioneering research conducted at Toyota Central Research Laboratories. The first practical application of a nanocomposite was in the use of a nylon-montmorillonite clay as a timing belt cover on a Toyota Camry automobile. This nanocomposite exhibited large increases in tensile strength, modulus and heat distortion temperature without a loss in impact resistance. The composite also had lower water sensitivity, permeability to gases and thermal coefficient of expansion. All of these property improvements could be realized without a loss of clarity in the polymer. It has been further found that nanocomposites impart a level of flame resistance and UV resistance. Nano-clay composites have also been successfully applied to thermosetting polymers, including epoxy^[52].

A. Structures of Clay [53]

Layered polysilicate, kaolinite, and layered double hydroxide are three typical kinds of clay used in polymer-clay nanocomposite materials. They all have good intercalation abilities, which means that polymer molecular can easily enter their interlayer spaces.

The framework of layered polysilicates consists of SiO_4 tetrahedra with some silanol groups in the interlayer region, and exchangeable cations are present in the interlayer region. The structure of polysilicate is shown in Figure 6.

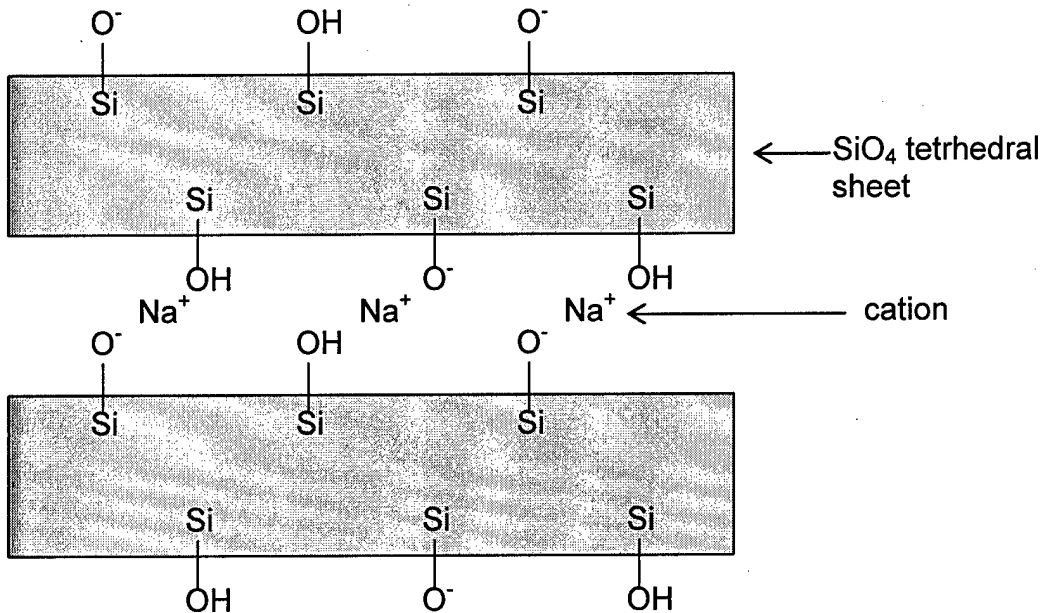


Figure 6. Structure of layered polysilicate.

Kaolinite consists of SiO_4 tetrahedral sheets and $\text{AlO}_2(\text{OH})_4$ octahedral sheets. Neither cations nor anions are present between the layers, and the layers are linked to each other by hydrogen bondings between hydroxyl groups on the octahedral sheets and the oxide arrangement of the tetrahedral sheets. The structure of Kaolinite is shown in Figure 7.

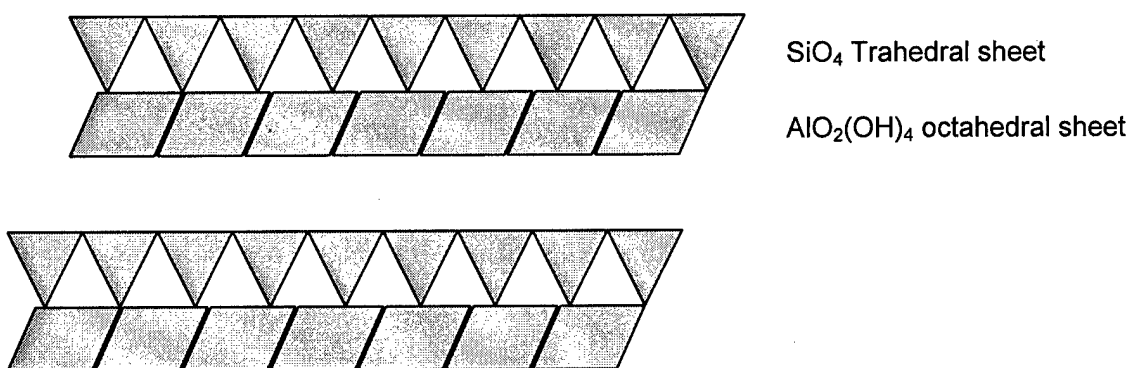


Figure 7. Structure of layered kaolinite

Layered double hydroxide consists of mainly brucite-like sheets. Anions are present between those layers. Figure 8 shows the structure of layered double hydroxide.

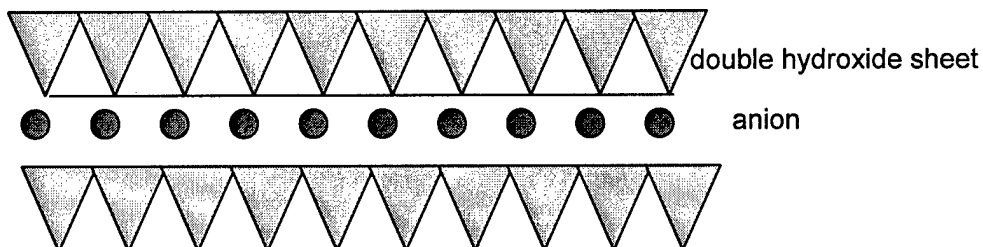


Figure 8. Structure of layered double hydroxide.

B. Reaction Routes in Layered Polysilicates

Layered polysilicates include kanemite, makatite, magadiite, octosilicates and kenyrite. Their structures consist mainly of layered SiO_4 tetrahedra. They are usually naturally occurring minerals, except octosilicates. Layered polysilicates can be treated using mild acid. Then we can get their acidic analogues, which have silanol groups in the interlayer region. Various organic function groups can be grafted onto polysilicates by reacting with those silanol groups. This process is called intercalation. Among those layered polysilicates, the intercalation ability of magadiite has been relatively well investigated^[51-53]. The procedure includes 3 steps:

- (i). ion exchange with organic cations,
- (ii). Adsorption of polar organic molecules to ions by dipolar interactions and/or to silanol groups by hydrogen bonds,
- (iii). Silylation and esterification of interlayer silanol groups.

In an early stage of investigation on magadiite intercalation, Lagaly et al. mentioned that caprolatam and acrylamide were intercalated into H-magadiite and polymerized in the interlayer space [54, 55]. Sugahara et al. reported intercalation of poly(acrylonitrile) into magadiite [56]. The procedure is:

- (i). Ion exchange. A $C_{12}H_{25}N(CH_3)_3^+$ -magadiite is prepared by ion exchange.
- (ii). Monomer intercalation. The system is soaked in acrylonitrile monomer containing 0.7 wt % benzoyl peroxide as an initiator for 24 hours.
- (iii). Polymerization. The mixture is heated at 50 °C for 24 hours.
- (iv). Heat treatment. The product is heat to 1300 °C, to get β-SiC ceramics.

Recently, Wang et al. have investigated the exfoliation of magadiite in an epoxy matrix [55-56]. Depending on the kind of interlayer ions, intercalated or exfoliated magadiite nanocomposites are obtained. The exfoliated nanocomposites are typically disordered, but a new type of exfoliated structure is also observed in which the nanolayers are regularly spaced over long distances (e.g. ~8 nm). The tensile properties of the polymer matrixes are greatly improved by the reinforcement effect of the silicate nanolayers.

C. Intercalation of Kaolinite

The layered structure of kaolinite, $Al_2Si_2O_5(OH)_4$, is shown in Figure 6. Kaolinite consists of 1:1 type sheets. It consists of SiO_4 tetrahedral sheets and AlO_6 octahedral hydroxyl sheets. There are no ions in the interlayer space. The interlayer regions are surrounded by hydroxyl groups on one side of the octahedral sheets, and the oxide arrangement of the silicate on the other side. The

layer thickness is around 0.72 nm. As kaolinite has its inherent hydrogen bondings between the layers, its intercalation reactivity is low. But several techniques have been developed to overcome this obstacle. The most effective technology is a guest displacement reaction. Dimethyl sulfoxide (DMSO) and n-methylformamide (NMF) are usually used as “guest”. They can pre-intercalate kaolinite, and then be displaced with various types of organic species^[59-61]. Figure 9 shows the process of guest displacement reaction. In the first step, the “guest” agent comes into the interlayer region inside of nano-clay (or kaolinite). It is called “pre-intercalation”. In the second step, “intercalation”, the “guest” agent is displaced by intercalating agent, so that we get the intercalated nano-clay as the product. Usually, “guest” agent has a smaller volume than intercalation agent, so it is easier for “guest” agent to get into the interlayer region of nano-clay. After the intercalation of “guest” agent, the interlayer region would be increased, which makes it easier for intercalating agent to get in. Recently, a kaolinite-methanol compound has shown to be an excellent intermediate for the intercalation. Other “guest” agents in recent reports include alkyamines, p-nitroaniline, ϵ -caprolactam and poly(vinylpyrrolidone)^[62-65].

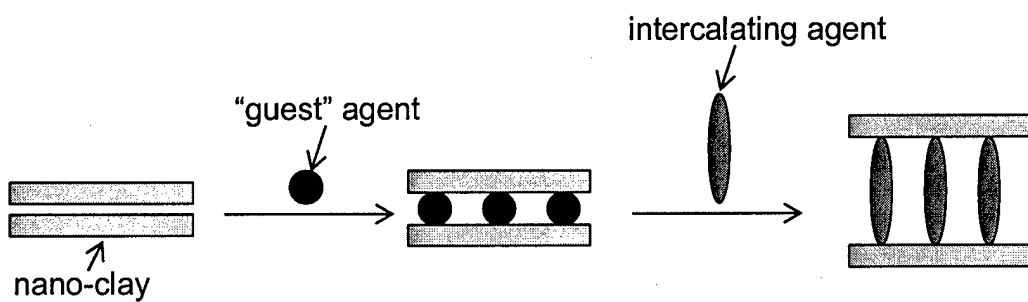


Figure 9. Process of guest displacement reaction.

D. Intercalation Property of Layered Double Hydroxide (LDH)

The structure of layered double hydroxides (LDH) was shown in Figure 8. They are minerals or synthetic materials with positively charged brucite-like layers of mixed hydroxides.

Exchangeable anions are located in the interlayer spaces. Conventional anion exchange is carried out in an aqueous solution. CO₂ should be excluded during the sample preparation, because it is very easy for CO₃²⁻ to enter LDH interlayer space, and once there, it would be difficult to be displaced.

E. Types of polymer-clay nanocomposites

From a structure point of view, polymer-clay composites can be generally classified into ‘conventional composites’ and ‘nanocomposites’. In a conventional composite, the registry of the clay nanolayer is retained when mixed with the polymer, but there is no intercalation of polymer into the clay structure. Consequently, the clay fraction in conventional clay composites plays little or no functional role and acts mainly as filling agent for economic considerations. An improvement in modulus is normally achieved in a conventional clay composite, but this reinforcement effects are limited.

Two types of polymer-clay nanocomposites are possible. Intercalated nanocomposites are formed when one or a few molecular layers of polymer are inserted into the clay galleries with fixed interlayer spaces. Exfoliated nanocomposites are formed when the silicate nanolayers are individually dispersed in the polymer matrix, the average distance between the segregated layers being dependent on the clay loading. Exfoliated nanocomposites show greater phase homogeneity than intercalated nanocomposites, and this structure can effectively improve the

performance of composite materials. Figure 10 shows the structure of these three types of clay-polymer composites.

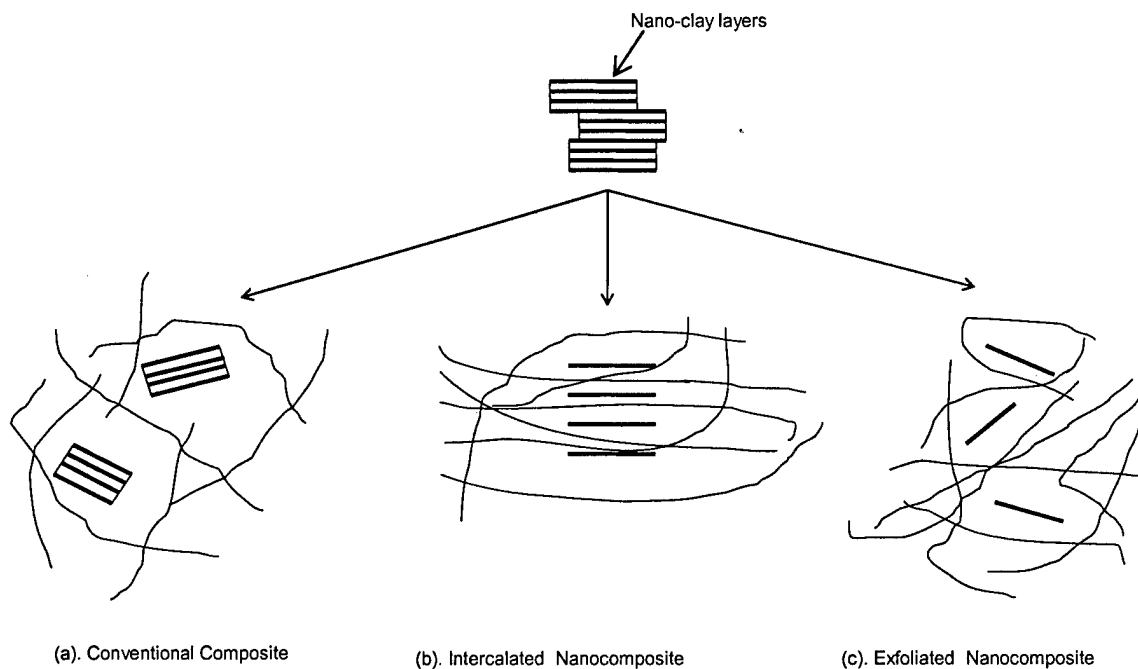


Figure 10. Schematic illustrations of clay-polymer composites.

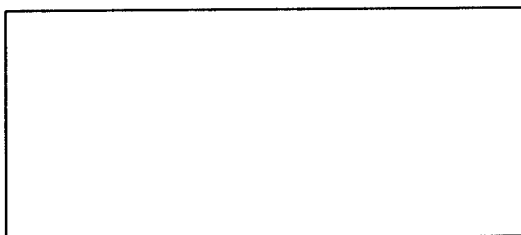
Pinnavaia et al. studied thermoset epoxy system with the ring opening polymerization of epoxides to form polyether nanocomposites [66-68]. This chemistry was studied for both rubbery and glassy thermoset epoxy-clay nanocomposite using different aminecuring agent. The mechanism leading to nanolayer exfoliation in thermoset epoxy systems have been greatly elucidated [69, 70]. In addition, the polymer-clay interfacial properties have been shown to play a dominant role in determining the performance benefits derived from nanolayer exfoliation [71].

4 THE LAYER MODEL FOR COMPOSITE MATERIALS

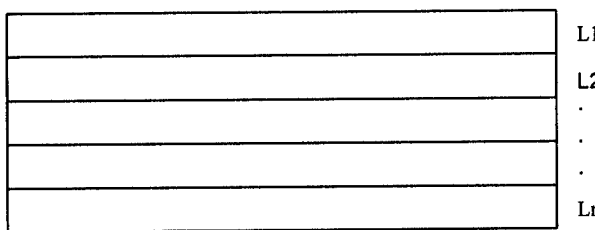
There are millions of fibers inside of composite material. It is practically impossible to model the real micro-structure of composite materials directly in finite element analysis.

The classic model to simulate composite materials is a homogenized orthotropic model. It assumes that a composite material is equivalent to a homogenous and orthotropic material.

Although the classic model is widely used and accepted in composite material design, it ignores the effects of adherend interfacial properties on the adhesive stress field. Thus we compared it with a more detailed model: the Layer Model. It assumes that a composite material is equivalent to the total effect of several different layers, each layer being distinctly homogenous and orthotropic (Figure 11).



Classic Model: homogenous and orthotropic.



Layer Model: composite is divided into several different homogenous and orthotropic layers.

Figure 11. Difference of the Classic Model and the Layer Model.

4.1 VALIDATION OF THE LAYER MODEL

In order to make sure the layer model is accurate and reliable, the results of a double lap adhesive bonded joint with a closed-form solution^[72] are compared with finite element analysis (ABAQUS) based on the classic model, and with finite element analysis (ABAQUS) based on the layer model.

Figure 12 and Figure 13 show that the results of these two methods have similar stress distributions. The maximum difference between FEA Layer Model results and the closed-form results is about 25%, because the absolute value of the stress in the middle of the adhesive joint overlap is close to zero, which makes the relative error significant. However, the trend shows that the Layer Model is reasonable.

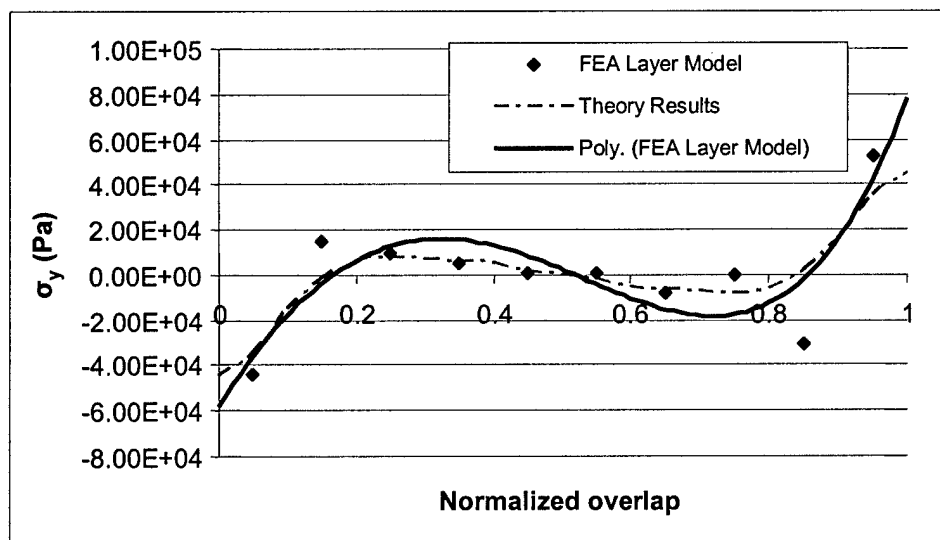


Figure 12. Comparison of Peeling Stress.

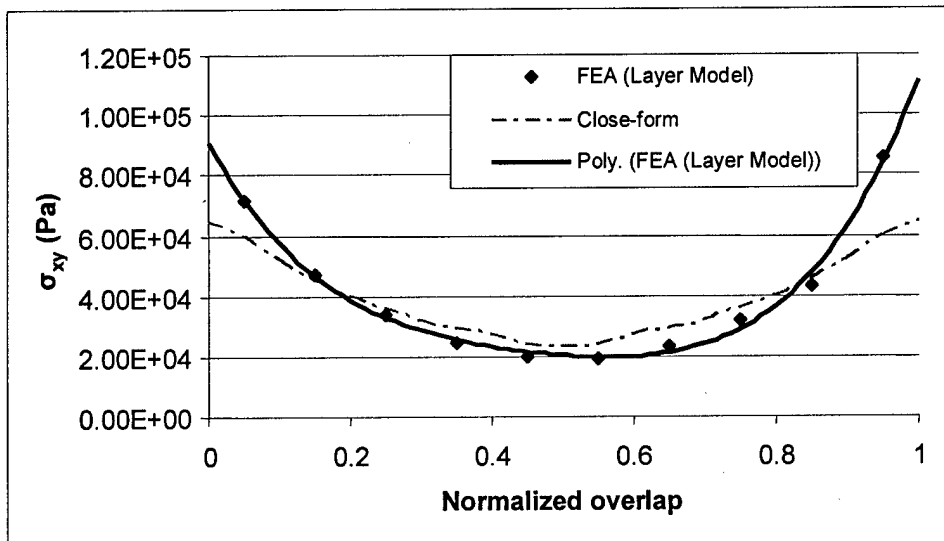


Figure 13. Comparison of Shear Stress.

4.2 NECESSITY OF LAYER MODEL

The detailed structure of the adherend, especially close to the adhesive layer, has a great affect on the maximum stress.

Both quarter-symmetry models (Figure 14 and 15) and half-symmetry models are studied for a double lap joint using ABAQUS FEA to compare the difference between the Layer Model and Homogenous Orthotropic Model.

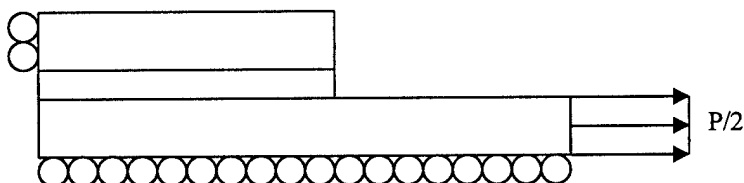


Figure 14. Quarter Model for Double Lap Adhesively Bonded Joints.

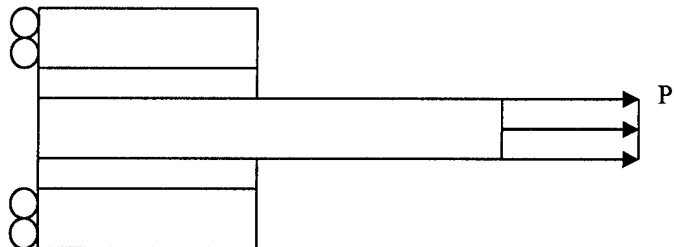


Figure 15. Quarter Model for Double Lap Adhesively Bonded Joints.

Firstly, the FEA stress results using the homogenous adherend (Figure 16) and layered adherend (Figure 17) are compared. The Young's modulus used in Figure 16 is 180 GPa, which is equal to the equivalent Young's modulus of the composite adherends in the reinforcing direction. In Figure 17, the adherend in the middle is divided into 60 layers, and the outer adherends are divided into 30 layers each. The layer thickness is 0.1 mm. Two different kind of layers are alternately distributed: High Modulus Layer, $E = 269.9$ GPa; Low Modulus Layer, $E = 4.6$ GPa. The modulus of the adhesive is 2.6 GPa. The maximum stresses (absolute value) in the two models are greatly different. The homogenous adherend gives a maximum adhesive stress twice that of the layered adherend.

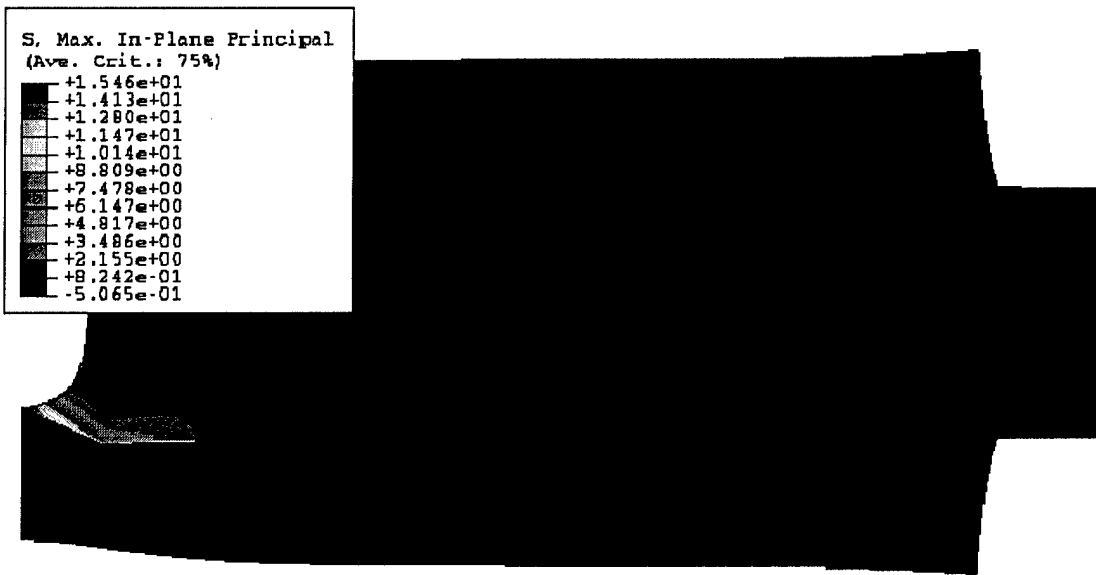


Figure 16. The Stress Distribution of Tensile Test in Uniform Adherend Model ($E=180$ Gpa).

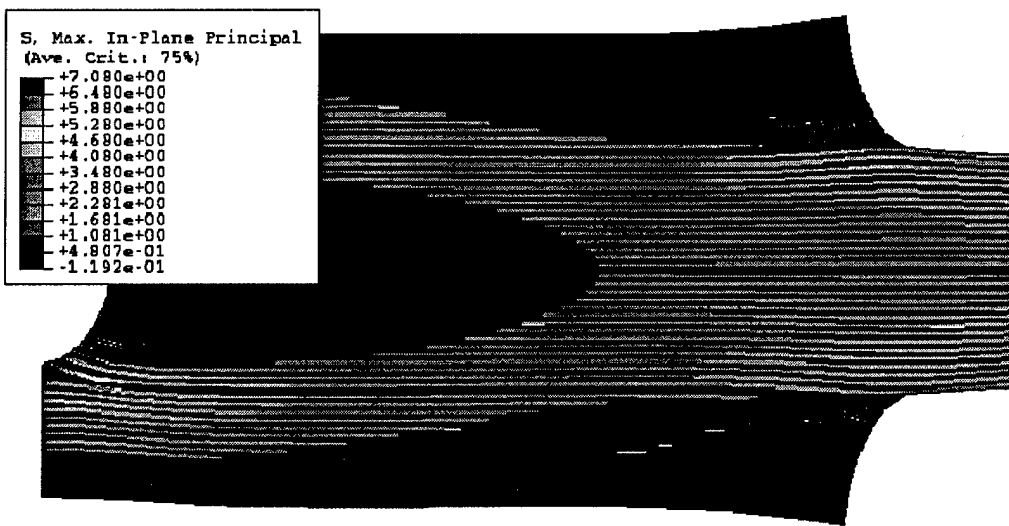


Figure 17. The Stress Distribution of Tensile Test in Layered Adherend Model
(layer thickness=0.1 mm).

The stress distribution of different layer orders, as shown in Figure 18, are also studied.

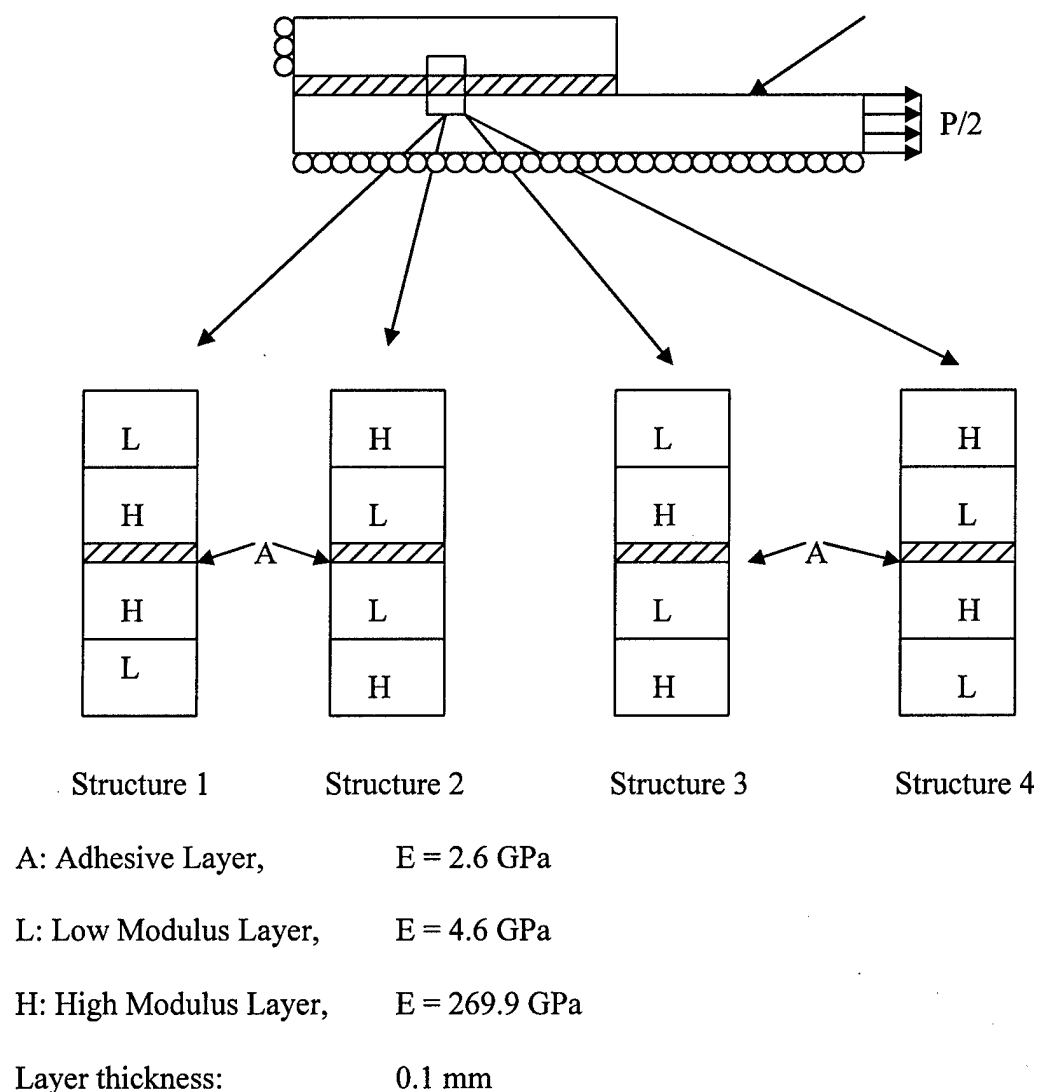


Figure 18. Different Layer Orders.

A comparison of the results is shown in Figure 19. It is found that the stress distributions in these four figures are very similar. The maximum stress occurs on the left end of the adhesive layer in Figure 18. The value of maximum stress (absolute value) shows a big difference.

Comparing the maximum stress (absolute value) in the four structures, we get:

Structure 4 > Structure 1 > Structure 3 > Structure 2

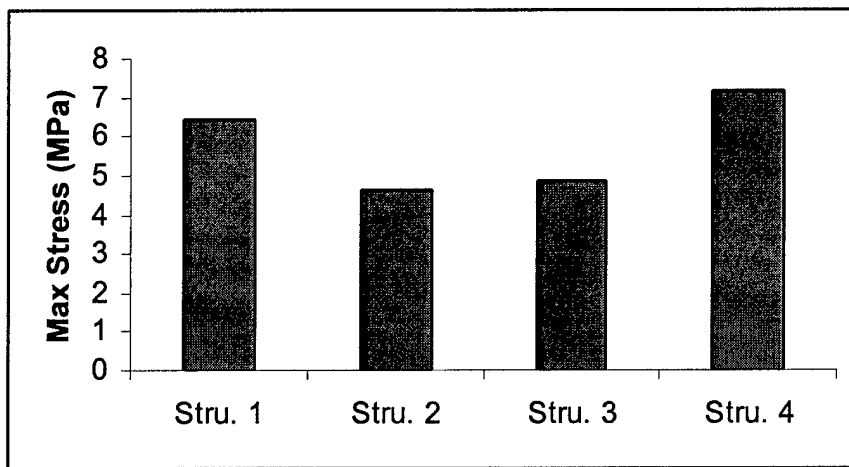


Figure 19. Comparison of Maximum Stress for Layer Adherends in Different Layer Orders.

The stress distributions are shown in Figure 20 ~23.

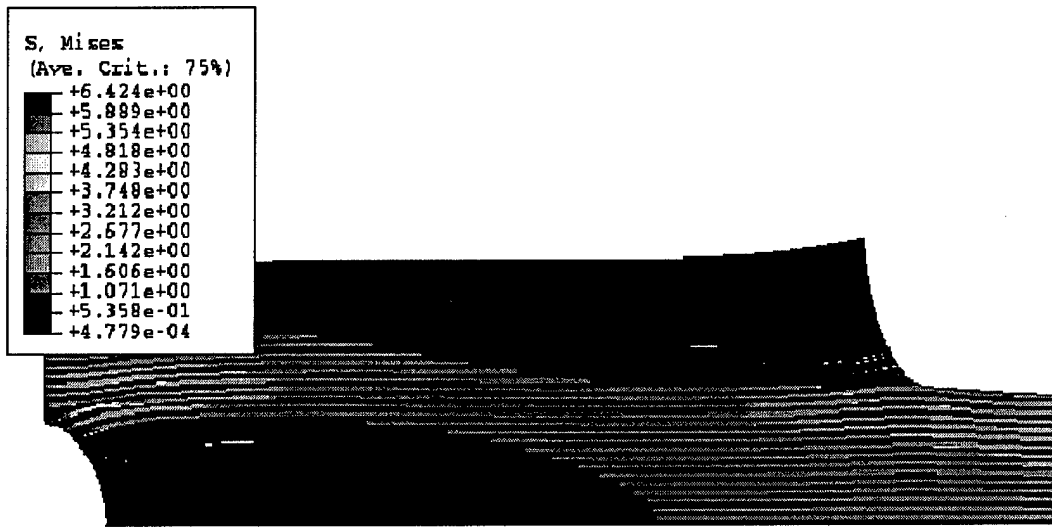


Figure 20. Layer Adherends, Structure 1.

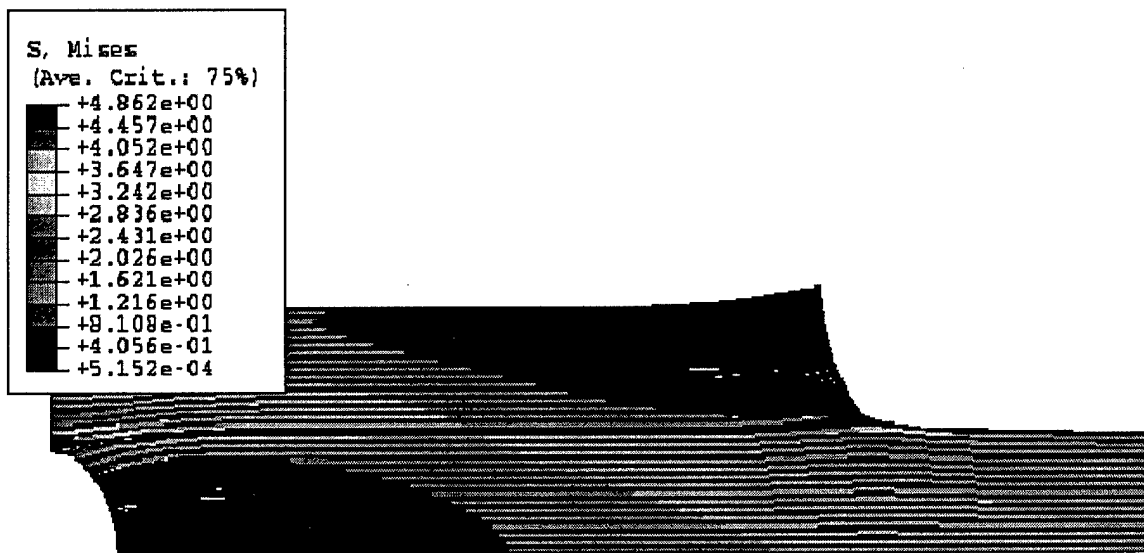


Figure 21. Layer Adherends, Structure 2.

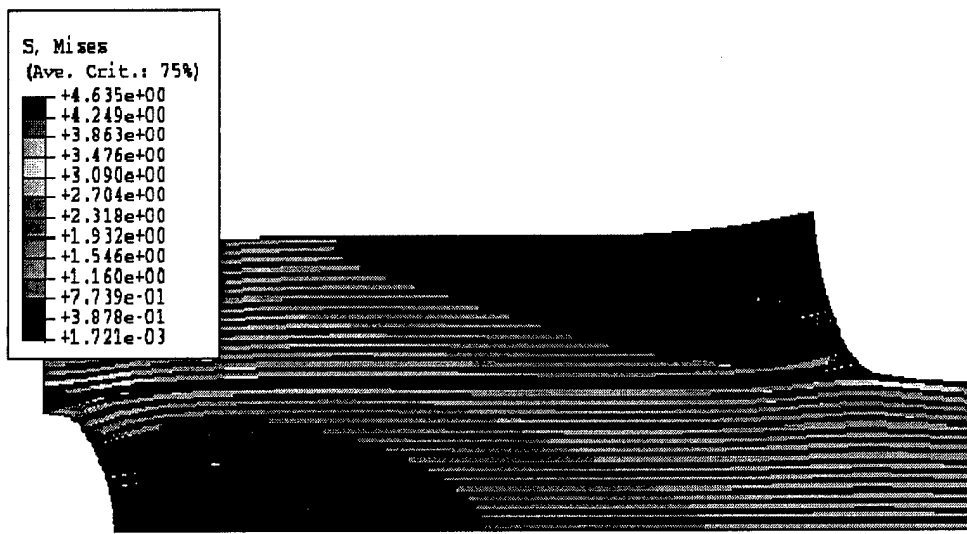


Figure 22. Layer Adherends, Structure 3.

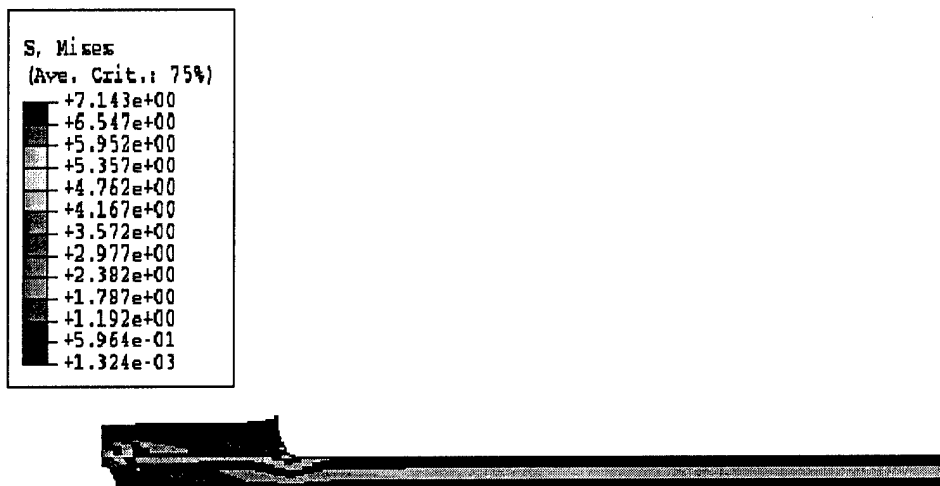


Figure 23. Layer Adherends, Structure 4.

4.3 THEORY OF THE ITERATIVE METHOD TO SOLVE FOR LOCAL MATERIAL PROPERTIES IN COMPOSITE

Given that the Layer Model is more accurate for composite adhesive bonded joints, the material properties for each layer of the composite material is now given.

The usual method to calculate the Young's modulus is to apply a load in x-direction, y-direction, and z-direction, respectively, and then using $E_i = \frac{\sigma_{ii}}{\varepsilon_{ii}}$ to calculate E_1 for load in x -direction, E_2 for load in y -direction, and E_3 for load in z -direction, where σ_{ii} and ε_{ii} mean the stress and strain in the i direction, respectively, $i = x, y, z$. This method assumes that stress is solely in the direction in which the load is applied. This assumption is reasonable for homogenous materials. But composite materials can transfer some load to other directions. For example, if a load in the x -direction is applied (Figure 24), the stress in the y -direction is about 10% as much as the stress in the x -direction. In this case to assume the stresses in another direction as zero is no longer reasonable. For this reason, we suggest using the Iterative Method in determining the equivalent material properties for composite material, including the equivalent material properties for the whole composite, and those for the local layers of the composite.

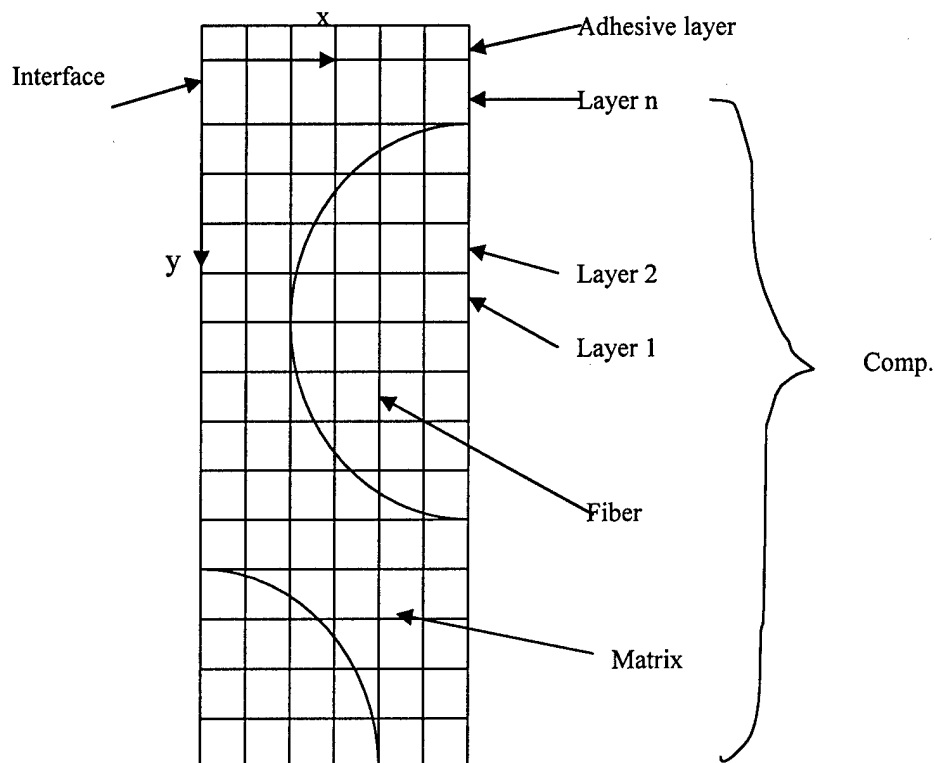


Figure 24. X-Y View of FEA Model for Calculating the Local Material Properties.

The formula used is the stress-strain relationship for orthotropic materials:

$$\begin{Bmatrix} \varepsilon_{11} \\ \varepsilon_{22} \\ \varepsilon_{33} \\ 2\gamma_{23} \\ 2\gamma_{13} \\ 2\gamma_{12} \end{Bmatrix} = \begin{bmatrix} \frac{1}{E_1} & -\frac{\nu_{21}}{E_2} & -\frac{\nu_{31}}{E_3} & 0 & 0 & 0 \\ -\frac{\nu_{12}}{E_1} & \frac{1}{E_2} & -\frac{\nu_{32}}{E_3} & 0 & 0 & 0 \\ -\frac{\nu_{13}}{E_1} & -\frac{\nu_{23}}{E_2} & \frac{1}{E_3} & 0 & 0 & 0 \\ 0 & 0 & 0 & \frac{1}{G_{23}} & 0 & 0 \\ 0 & 0 & 0 & 0 & \frac{1}{G_{13}} & 0 \\ 0 & 0 & 0 & 0 & 0 & \frac{1}{G_{12}} \end{bmatrix} \begin{Bmatrix} \sigma_{11} \\ \sigma_{22} \\ \sigma_{33} \\ \tau_{23} \\ \tau_{13} \\ \tau_{12} \end{Bmatrix} \quad (11)$$

In Equation (11), $\frac{\nu_{12}}{E_1} = \frac{\nu_{21}}{E_2}$, $\frac{\nu_{13}}{E_1} = \frac{\nu_{31}}{E_3}$, and $\frac{\nu_{23}}{E_2} = \frac{\nu_{32}}{E_3}$. Then Equation (11) can be rewritten as

$$\begin{Bmatrix} \varepsilon_{11} \\ \varepsilon_{22} \\ \varepsilon_{33} \\ 2\gamma_{23} \\ 2\gamma_{13} \\ 2\gamma_{12} \end{Bmatrix} = \begin{bmatrix} \frac{1}{E_1} & -\frac{\nu_{12}}{E_1} & -\frac{\nu_{13}}{E_1} & 0 & 0 & 0 \\ -\frac{\nu_{12}}{E_1} & \frac{1}{E_2} & -\frac{\nu_{23}}{E_2} & 0 & 0 & 0 \\ -\frac{\nu_{13}}{E_1} & -\frac{\nu_{23}}{E_2} & \frac{1}{E_3} & 0 & 0 & 0 \\ 0 & 0 & 0 & \frac{1}{G_{23}} & 0 & 0 \\ 0 & 0 & 0 & 0 & \frac{1}{G_{13}} & 0 \\ 0 & 0 & 0 & 0 & 0 & \frac{1}{G_{12}} \end{bmatrix} \begin{Bmatrix} \sigma_{11} \\ \sigma_{22} \\ \sigma_{33} \\ \tau_{23} \\ \tau_{13} \\ \tau_{12} \end{Bmatrix} \quad (12)$$

Load Cases for the Iterative Method

Three load cases are examined:

Load Case A: Tensile load in x-direction (11-direction)

Data: Average σ_{A11} , σ_{A22} , σ_{A33} , ε_{A11} , ε_{A22} , ε_{A33} for Layer n.

Load Case B: Tensile load in y-direction (22-direction)

Data: Average σ_{B11} , σ_{B22} , σ_{B33} , ε_{B11} , ε_{B22} , ε_{B33} for Layer n.

Load Case C: Tensile load in z-direction (33-direction)

Data: Average σ_{C11} , σ_{C22} , σ_{C33} , ε_{C11} , ε_{C22} , ε_{C33} for Layer n.

4.4 STEPS OF THE ITERATIVE METHOD

C. Initial Values of Material Properties

In this step, we used simplified formulas to calculate the approximate solution of these material properties. These values are taken as the initial values of material properties, which will be used in the next step.

$$E1_0 = \frac{\sigma_{A11}}{\varepsilon_{A11}} \quad (13)$$

Equation (13) is based on $\varepsilon_{A11} = \frac{\sigma_{A11}}{E1} - \frac{\nu12}{E1}\sigma_{A22} - \frac{\nu13}{E1}\sigma_{A33}$, which is the first line of Equation (12). It is in Load Case A and assumes $\sigma_{A22} = \sigma_{A33} = 0$.

$$E2_0 = \frac{\sigma_{B22}}{\varepsilon_{B22}} \quad (14)$$

Equation (14) is based on $\varepsilon_{B22} = -\frac{\nu12}{E1}\sigma_{B11} + \frac{\sigma_{B22}}{E2} - \frac{\nu23}{E2}\sigma_{B33}$, which is the second line of Equation 12. It is in Load Case B and assumes $\sigma_{B11} = \sigma_{B33} = 0$.

$$E3_0 = \frac{\sigma_{C33}}{\varepsilon_{C33}} \quad (15)$$

Equation (15) is based on $\varepsilon_{C33} = -\frac{\nu13}{E1}\sigma_{C11} - \frac{\nu23}{E2}\sigma_{C22} + \frac{\sigma_{C33}}{E3}$, which is the third line of Equation (12). It is in Load Case C and assumes $\sigma_{C11} = \sigma_{C22} = 0$.

$$\nu13_0 = \frac{\sigma_{C11} - E1_0 \cdot \varepsilon_{C11}}{\sigma_{C22} + \sigma_{C33}} \quad (16)$$

Equation (16) is based on $\varepsilon_{C11} = \frac{\sigma_{C11}}{E1} - \frac{\nu12}{E1}\sigma_{C22} - \frac{\nu13}{E1}\sigma_{C33}$, which is the first line of Equation (12). It is in Load Case C and assumes $\nu12 = \nu13$.

$$\nu23_0 = \frac{\varepsilon_{C22} - \frac{\sigma_{C22}}{E2_0}}{-\frac{\sigma_{C11}}{E1_0} - \frac{\sigma_{C33}}{E2_0}} \quad (17)$$

Equation (17) is based on $\varepsilon_{C22} = -\frac{\nu12}{E1}\sigma_{C11} + \frac{\sigma_{C22}}{E2} - \frac{\nu23}{E2}\sigma_{C33}$, which is the second line of Equation (12). It is in Load Case C and assumes $\nu12 = \nu23$.

$$\nu12_0 = \frac{\sigma_{B11} - \nu_{13} \cdot \sigma_{B33} - E1_0 \cdot \varepsilon_{B11}}{\sigma_{B22}} \quad (18)$$

Equation (18) is based on $\varepsilon_{B11} = \frac{\sigma_{B11}}{E1} - \frac{\nu12}{E1}\sigma_{B22} - \frac{\nu13}{E1}\sigma_{B33}$, which is the first line of Equation (12). It is in Load Case B.

D. Iterative Loop to Get Accurate Material Properties

The following steps use no simplification, all the work is based on the stress-strain relationship for orthotropic materials. Every iterative loop gives more accurate results, converging rapidly.

$$E1_i = \frac{\sigma_{A11} - \nu12_{i-1} \cdot \sigma_{A22} - \nu13_{i-1} \cdot \sigma_{A33}}{\varepsilon_{A11}} \quad (19)$$

Equation (19) is based on $\varepsilon_{A11} = \frac{\sigma_{A11}}{E1} - \frac{\nu12}{E1}\sigma_{A22} - \frac{\nu13}{E1}\sigma_{A33}$, which is the first line of Equation (12). It is in Load Case A.

$$E2_i = \frac{\sigma_{B22} - \nu23_{i-1}\sigma_{B33}}{\varepsilon_{B22} + \frac{\nu12_{i-1}}{E1_i}\sigma_{B11}} \quad (20)$$

Equation (20) is based on $\varepsilon_{B22} = -\frac{\nu12}{E1}\sigma_{B11} + \frac{\sigma_{B22}}{E2} - \frac{\nu23}{E2}\sigma_{B33}$, which is the second line of

Equation (12). It is in Load Case B.

$$E3_i = \frac{\sigma_{C33}}{\varepsilon_{C33} + \frac{\nu13_{i-1}}{E1_i}\sigma_{C11} + \frac{\nu23_{i-1}}{E2_i}\sigma_{C22}} \quad (21)$$

Equation (21) is based on $\varepsilon_{C33} = -\frac{\nu13}{E1}\sigma_{C11} - \frac{\nu23}{E2}\sigma_{C22} + \frac{\sigma_{C33}}{E3}$, which is the third line of Equation

(12). It is in Load Case C.

$$\nu13_i = \frac{\sigma_{C11} - \nu12_{i-1} \cdot \sigma_{C22} - E_i \cdot \varepsilon_{C11}}{\sigma_{C33}} \quad (22)$$

Equation (22) is based on $\varepsilon_{C11} = \frac{\sigma_{C11}}{E1} - \frac{\nu12}{E1}\sigma_{C22} - \frac{\nu13}{E1}\sigma_{C33}$, which is the first line of Equation

(12). It is in Load Case C.

$$\nu23_i = \frac{\varepsilon_{C22} - \frac{\sigma_{C22}}{E2_i} + \frac{\nu12_{i-1} \cdot \sigma_{C11}}{E1_i}}{-\frac{\sigma_{C33}}{E2_i}} \quad (23)$$

Equation (23) is based on $\varepsilon_{C22} = -\frac{\nu12}{E1}\sigma_{C11} + \frac{\sigma_{C22}}{E2} - \frac{\nu23}{E2}\sigma_{C33}$, which is the second line of Equation

(12). It is in Load Case C.

$$\nu12_i = \frac{\sigma_{B11} - \nu13_i \cdot \sigma_{B33} - E1_i \cdot \varepsilon_{B11}}{\sigma_{B22}} \quad (24)$$

Equation (24) is based on $\varepsilon_{B11} = \frac{\sigma_{B11}}{E1} - \frac{\nu12}{E1}\sigma_{B22} - \frac{\nu13}{E1}\sigma_{B33}$, which is the first line of

Equation (12). It is in Load Case B.

At last we would get 6 engineering material constants for Layer n . Repeat this process, but using the stress and strain data averaged for Layer $n+1$, we can get the material properties for Layer $n+1$. The whole process in determining the material constants in each layer of composite material is shown in Figure 25.

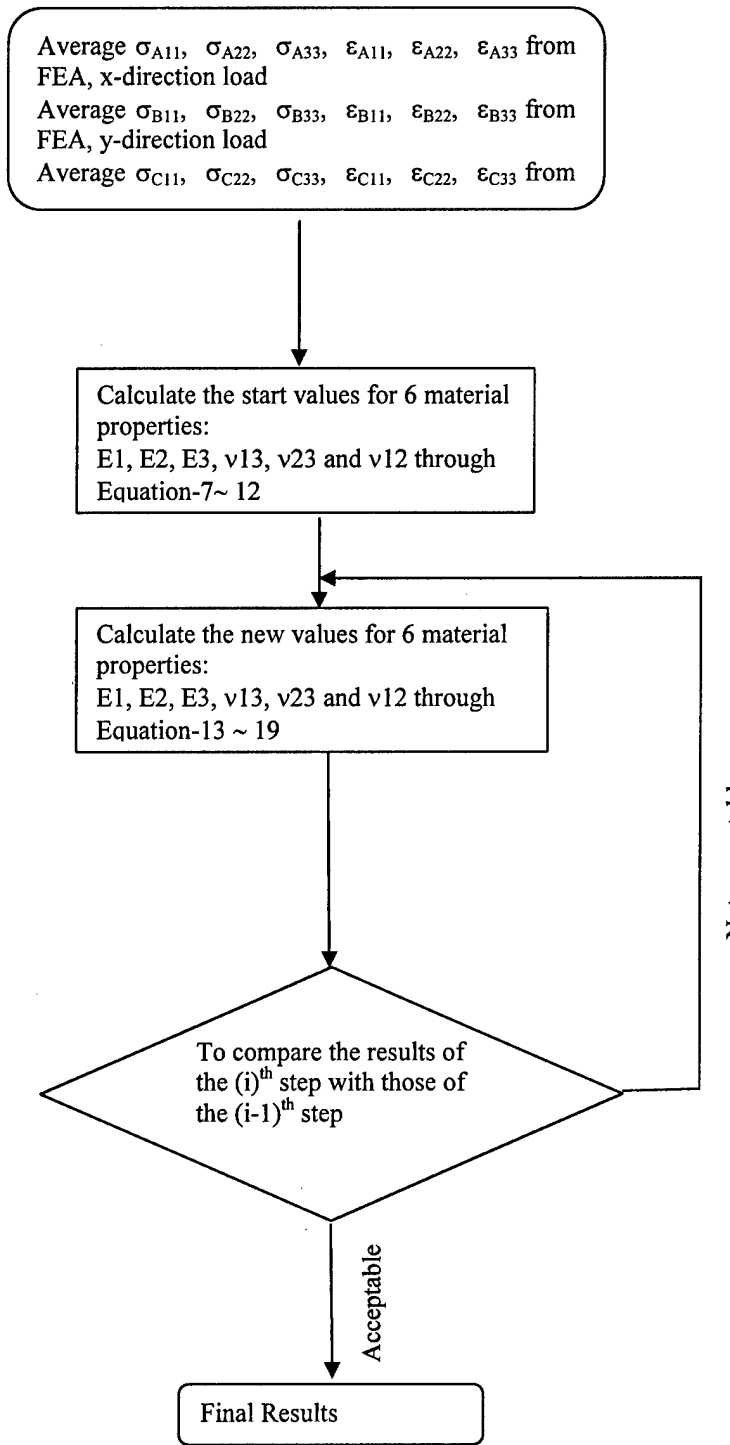


Figure 25. The Process of the Iterative Method to Calculate the Local Material Properties for a Composite.

4.5 RESULTS OF THE ITERATIVE METHOD TO SOLVE THE LOCAL MATERIAL PROPERTIES IN A COMPOSITE

The effects of the iterative method to solve the local material properties in a composite are shown in Figure 26 (the reinforcing direction is the 3-direction).

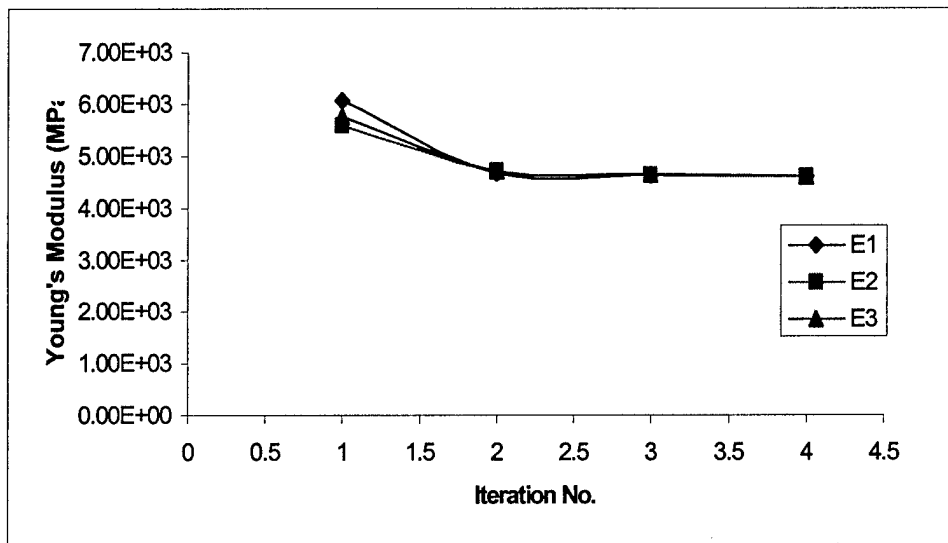


Figure 26. Effect of Iteration (Young's Modulus vs. Iteration No. for Layer 6).

Figure 26 shows:

- (1) This method converges rapidly. The results of the 3rd loop are close to those of the 4th loop. The maximum difference is less than 1%.
- (2) The final results for Layer 6, which is pure resin, are very close to the bulk material properties of resin. The error is less than 0.25%.
- (3) The results of the 1st loop are the results of the classic method. The classic method has about 10% error compared with the iterative method.

The final results of the local material properties of the composite material are shown in Figure 27 and Figure 28.

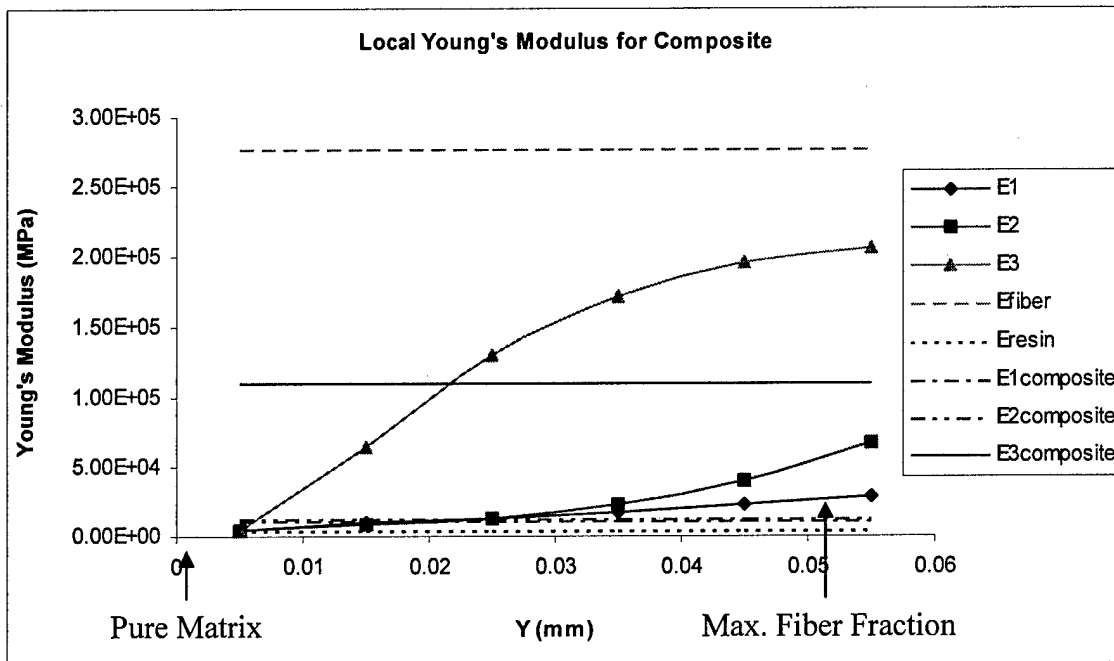


Figure 27. The Local Young's Modulus of Composite Material.

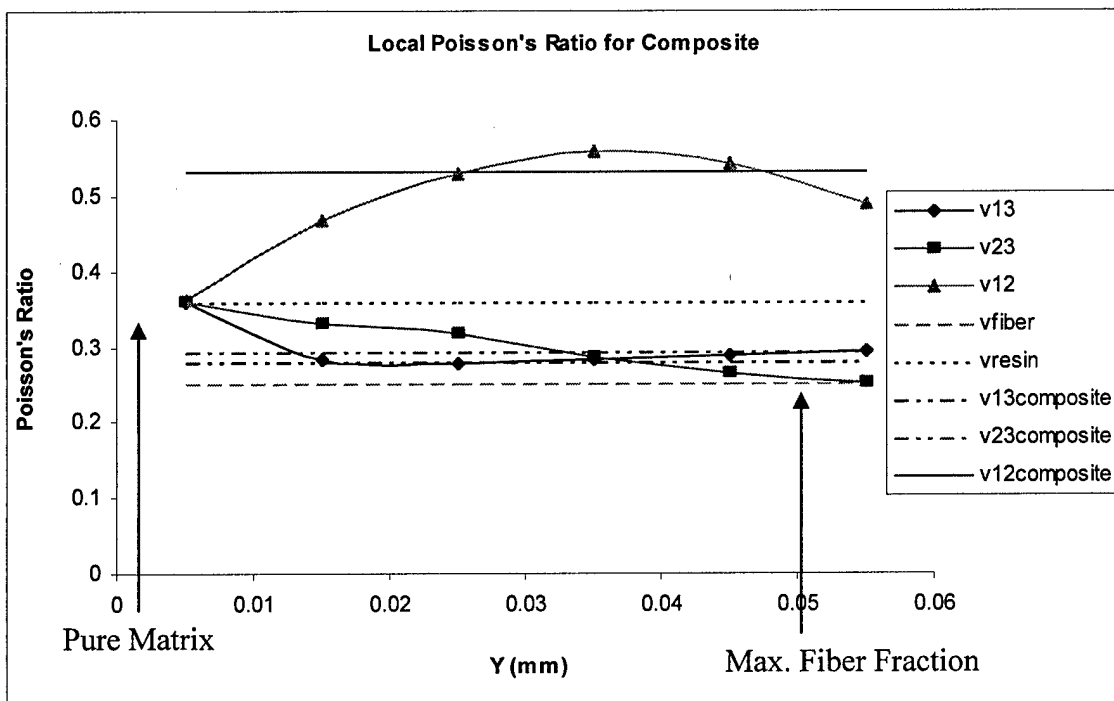


Figure 28. The Local Poisson's Ratio of Composite Material.

All three Young's moduli keep increasing with the increase of fiber fraction, which is reasonable. The Young's moduli of the first layer, which is made up of pure matrix, is exactly equal to the Young's moduli of matrix resin.

4.6 LOCAL SHEAR MODULUS OF COMPOSITE MATERIALS

We already know the relationship among the shear stress, shear strain and shear modulus from the 4th ~ 6th lines of Equation (12), which are:

$$\gamma_{12} = \frac{\tau_{12}}{2G_{12}} \quad (25)$$

$$\gamma_{13} = \frac{\tau_{13}}{2G_{13}} \quad (26)$$

$$\gamma_{23} = \frac{\tau_{23}}{2G_{23}} \quad (27)$$

Calculation of G_{12} presents a problem. For a small piece of composite material, as the fiber shear modulus is much bigger than that of matrix, its boundary would become obviously distorted subjected to the shear load (Figure 29). This situation makes the average shear deformation physically meaningless.

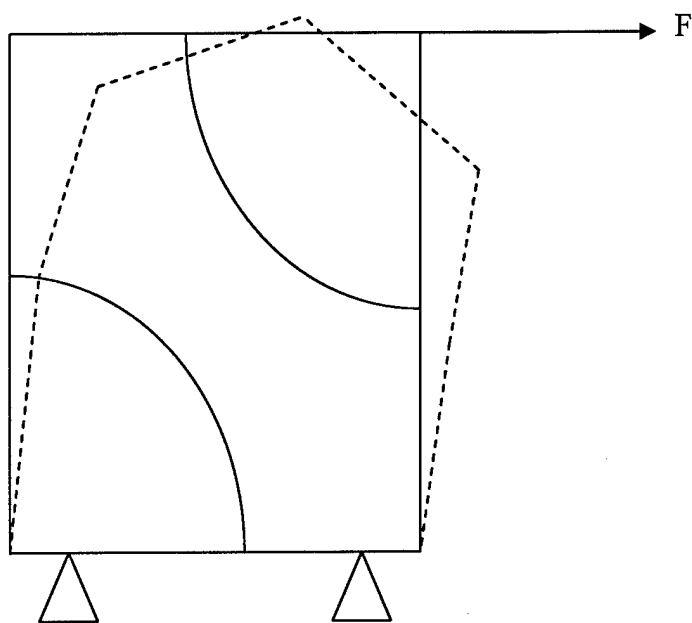


Figure 29. Deformation of Small Composite Piece Subjected to Shear Load.

To solve this problem, in the FE model , we added rigid bodies on the four sides of the composite cell with good results (Figure 30).

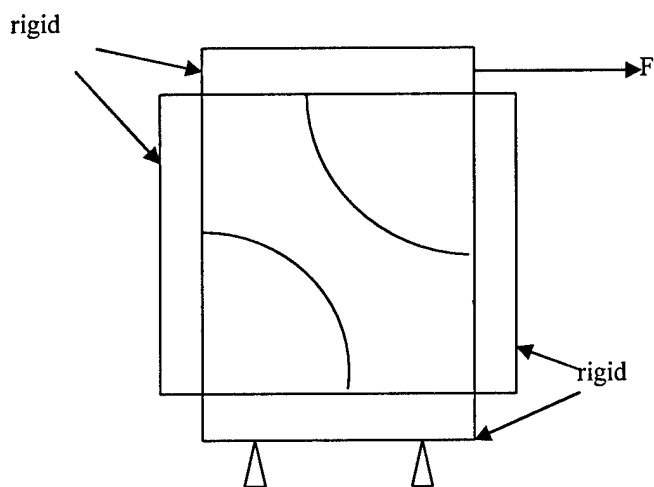
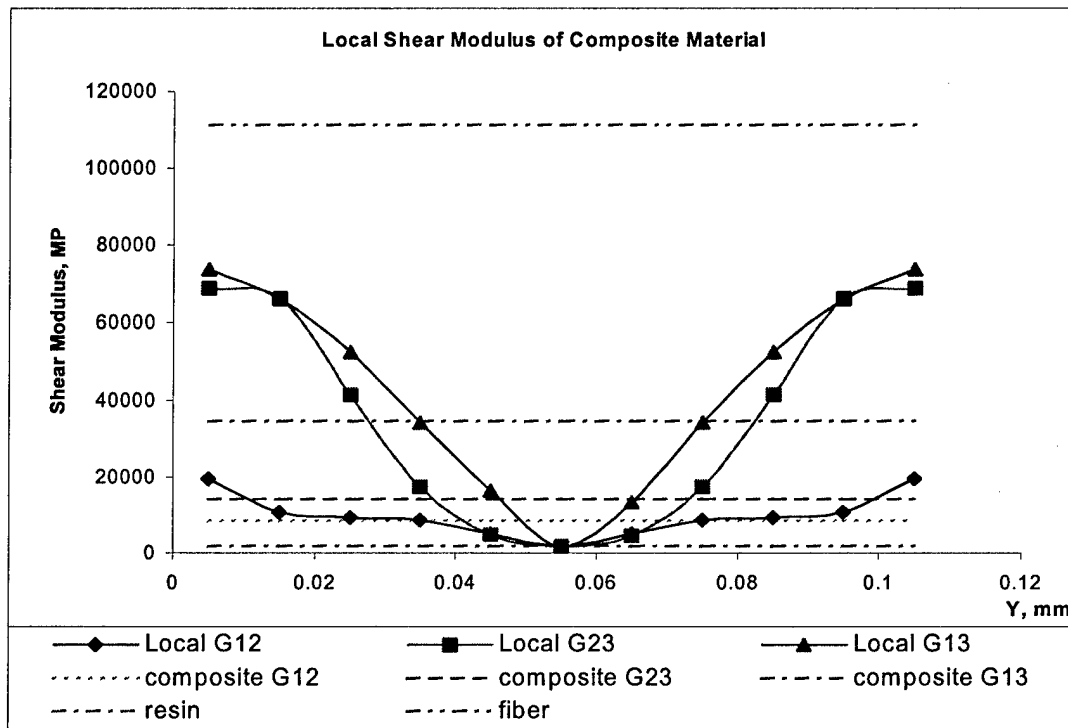


Figure 30. FEA Shear Model to Calculate G_{12} .

The results of shear modulus are given in Figure 31. All three shear moduli keep increasing with the increase of fiber fraction, which is reasonable. The shear moduli of the middle layer, which is made up of pure matrix, is exactly equal to the shear moduli of matrix resin.

Figure 31. Local Shear Modulus of Composite Material.



4.7 CONCLUSION

- The detailed structure of an adhesively bonded composite joints, especially at the range close to the interface between composite and adhesive, is very important. For example, as the interface layer modulus changes, the maximum stress changes greatly.
- We suggest a new model (Layer Model) for composite materials, which is closer to the real structure of composite materials than the classic model.
- We established an iterative method in micro-mechanical analysis to simulate the layer properties of composite materials. We found the difference from the classic method to be about 10%.

5 FRACTURE MECHANICS ANALYSIS FOR ADHESIVE JOINTS

No material in practical use is perfect. Defects always exist, and the cracks growing from them can adversely change the stress distribution because of the stress concentration effects. In our research, we show that there are both free edge and central singularities for the single-strap adhesive joints, which is a common joint in airplane repair. So it is important to take the effects of cracks into consideration in mechanical design. Adhesive joints also have defects, thus it is essential to verify the reliability of an adhesive joint with cracks.

The FEA software ABAQUS provides the avenue to make fracture mechanics analysis in complex structures. Before FEA fracture mechanics was applied on the adhesive joint, the necessity and reliability for a single strap adhesive joint was verified.

5.1 STRESS DISTRIBUTION IN ADHESIVE LAYER OF SINGLE STRAP JOINTS

Because of stress concentration, the maximum stress got from theoretical linear static analysis goes to infinity. In this case, the material in the high stress concentration region would have plastic deformation. Plasticity and non-linearity would become necessary to get accurate stress results. This is difficult, time-consuming and high cost. Fracture mechanics analysis can solve this problem, because it allows using linear analysis for brittle material failure, even if there exists small region plasticity. This section focuses on aluminum single strap joints, which are common in airplane wing repair. Figures 32 and 33 give the schematic and the model of the single strap joint used in our research.

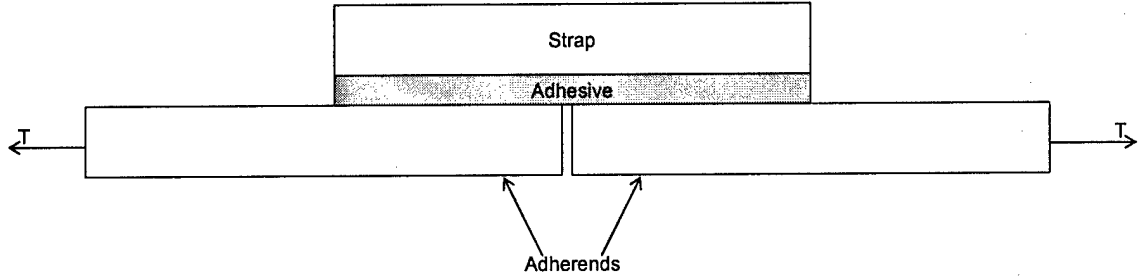


Figure 32 Schematic of single-strap adhesive sample.

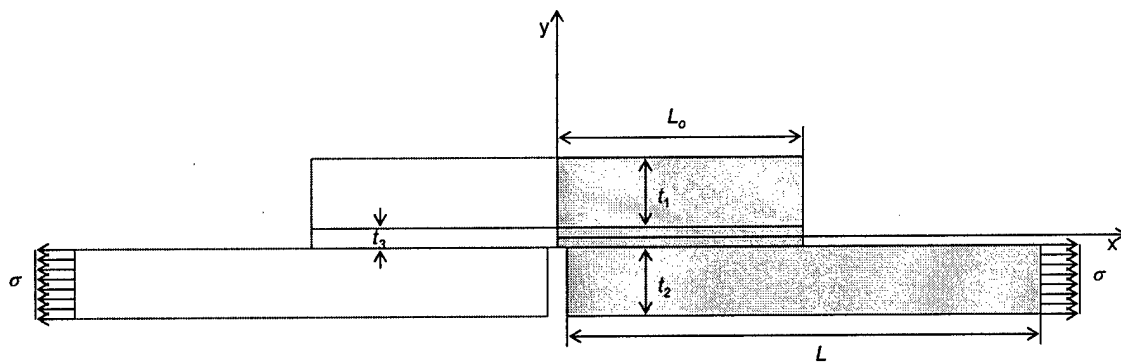


Figure 33. Single strap joint model.

The material properties of adherends are $E = 70$ GPa, $\nu = 0.3$ (material properties for typical aluminum). Those of the adhesive layer are $E = 2.2$ GPa, $\nu = 0.4$ (material properties for typical epoxy). The applied stress $\sigma = 1.0$ MPa. The dimensions used in Figure 33 are as following: $L = 120$ mm, $L_o = 20$ mm, $t_1 = t_2 = 3$ mm, and $t_3 = 0.2$ mm. We chose these dimensions because there are such aluminum bars commercially available. Let b be the side length of the smallest finite elements for the model, (elements not shown in Figure 33). Both coarse mesh and fine mesh are used. For the coarse meshed model, the total element number is 2150 and the total node number is 2464, and $b/L_o = 0.02$. For the fine meshed model, the total element number is

18900 and the total node number is 19389, with $b/L_o = 0.00096$. Figures 34-36 show the results of these two models.

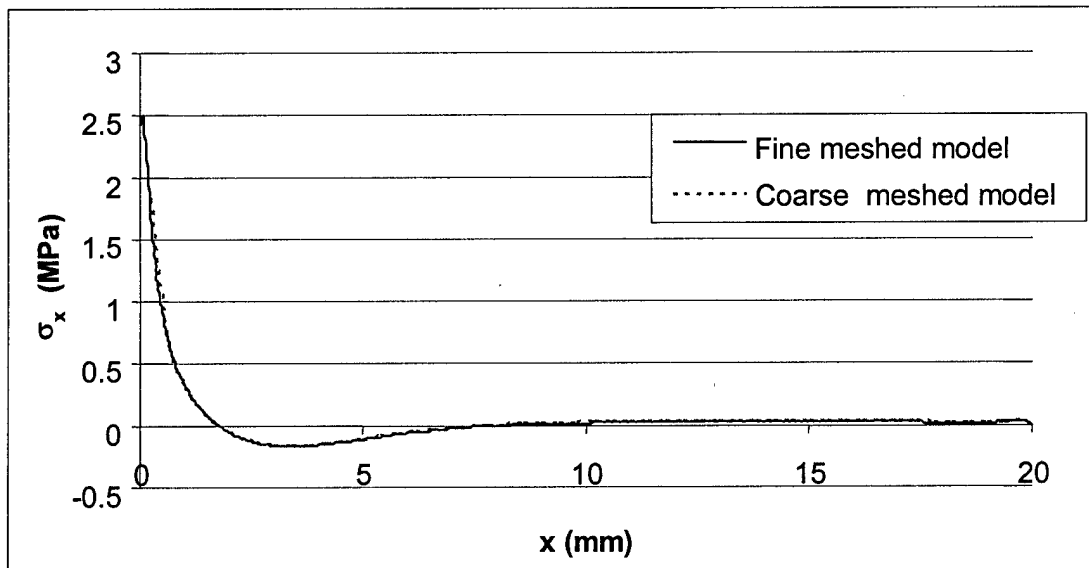


Figure 34. Tensile stress in the adhesive layer of single strap joints.

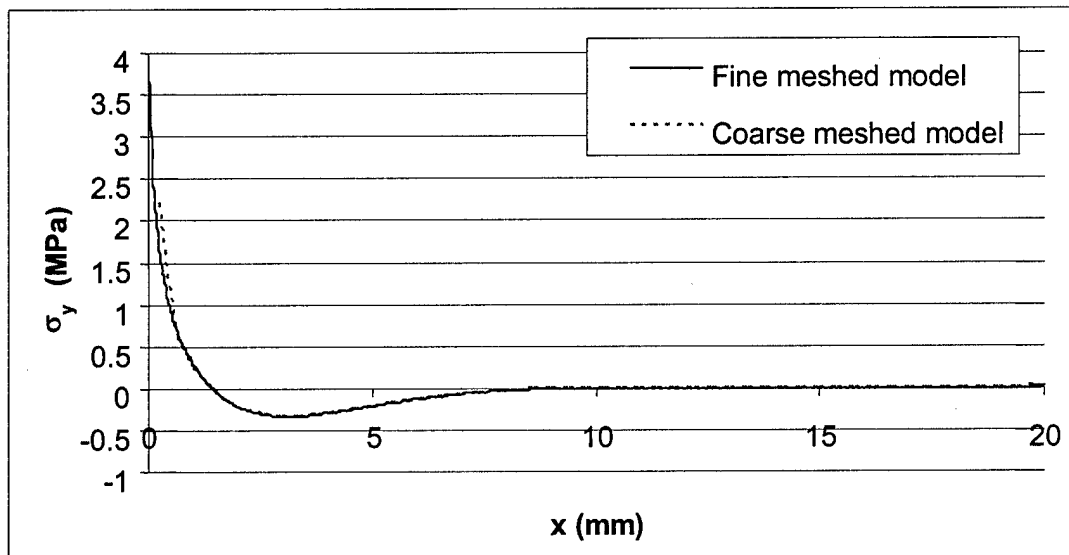


Figure 35. Peeling stress in the adhesive layer of single strap joints.

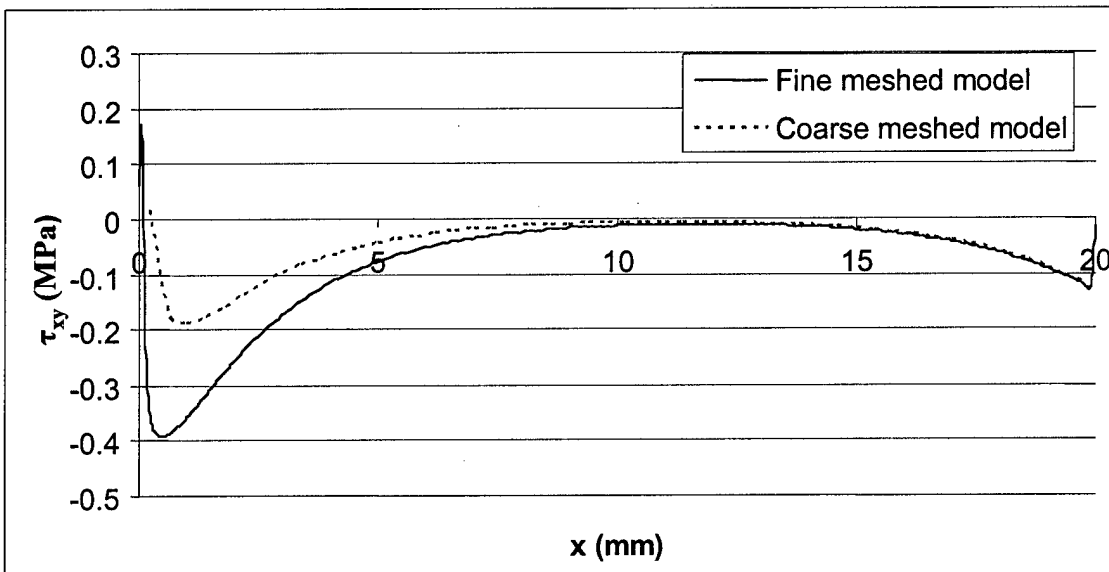


Figure 36. Shear stress in the adhesive layer of single strap joints.

In Figures 35-36, we are interested in comparing the maximum stress. Coarse meshed model is accurate for tensile stress σ_x and peeling stress σ_y in low stress concentration region, but the shear stress τ_{xy} seems not accurate even in low stress concentration region. The reason is the location of maximum shear stress is closer to the low stress concentration region. The tensile stress and the peeling stress tend to go to infinity at the center of the joint ($x = 0$); the shear stress has a maximum value at $x = 0.5$ mm. For all of these three different stress, fine meshed model gives a much higher maximum stress. If we further increase the mesh density, the reported value of the maximum stress in a single strap adhesive joint can be even higher. Theoretically, σ_x and σ_y can approach infinity. This is called as singularity. Because of this singularity problem, fracture mechanics analysis is needed for the design of single strap adhesive joint.

5.2 MESH DENSITY SENSITIVITY STUDY OF FEA FRACTURE MECHANICS

A. Model of Rectangular Bar

In order to determine the suitable mesh density used for our research, the mesh density sensitivity of FEA fracture mechanics was studied by comparing the FEA results and theoretical results for the energy release rate of a crack in a rectangular bar (shown in Figure 37). The crack length is $2a$ and the dimension of the rectangular bar is $2L \times 2W$, with $W = 100$ mm, $L = 200$ mm, and $a = 10$ mm. (For a plane strain problem, the thickness of the rectangular bar is large.) The material properties used in this model are: elastic modulus, $E = 200$ GPa and Poisson's ratio, $\nu = 0.3$. b is the side length of the smallest finite elements for the model, (elements not shown in Figure 37). It is a parameter to show the mesh density of the FEA model. We define b as the representative side length of the elements around the crack tip.

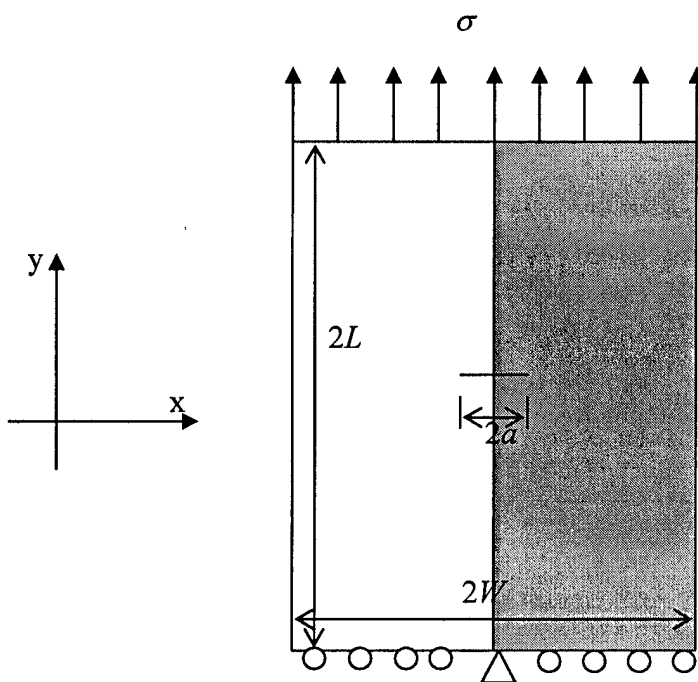


Figure 37. Model for evaluation of the reliability of FEA fracture mechanics.

A theoretical calculation was carried according to Equations (28-30) [5]:

$$K_I = \sigma \sqrt{\pi a} \left(\sec \frac{a}{W} \right)^{1/2} \quad (28)$$

$$G_I = \frac{K_I^2 (1 - \nu^2)}{E} \quad (29)$$

$$Error(\%) = \frac{G_{Theory} - G_{FE}}{G_{Theory}} \times 100 \quad (30)$$

where G_I is the energy release rate, K_I is the stress intensity factor, and σ is the far field stress.

The Virtual Crack Closure method was also used to calculate the energy release rate [73]. It assumes that the energy needed to make a crack propagate a distance δ is U :

$$U = 2 \int_{-\delta}^{\delta} \bar{v} dF \quad (31)$$

where \bar{v} is the average y-direction displacement (Figure 38), and dF is the increase of crack opening force. The factor of 2 is included because there are two surfaces produced when the crack propagates. The methods to calculate \bar{v} and F are given in Equations (32) and (33):

$$\bar{v} = \frac{v}{2} \quad (32)$$

$$dF = \sigma_y t dx \quad (33)$$

where v is the maximum y-direction displacement, σ_y is the normal stress in the y-direction, and t is the thickness of the plate. The energy release rate is given by

$G_I = U/bt$, and the calculation of G_I is given in Equation (34). Figure 38 gives the definition of the variables.

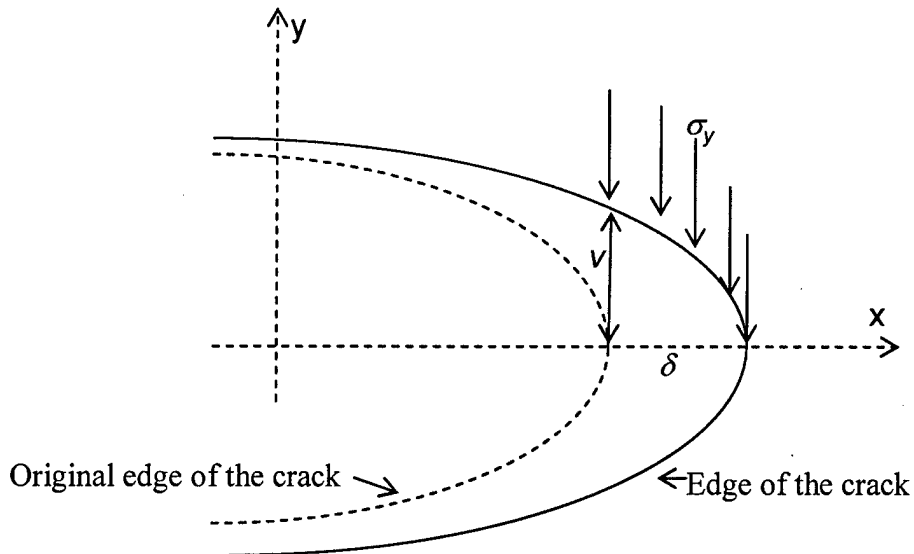


Figure 38. Variable definition for Virtual Crack Closure method.

$$G_I = \lim_{\delta \rightarrow 0} \frac{2}{\delta} \int_0^{\delta} \frac{1}{2} \sigma_y v dx \quad (34)$$

Equation (35) gives the Virtual Crack Closure method FEA calculation of energy release rate. Figure 39 shows the variables in Equation (35), where v is the maximum y-direction displacement, σ_y is the normal stress in the y-direction, and t is the thickness of the plate.

$$G_I = -Fv / \delta \quad (35)$$

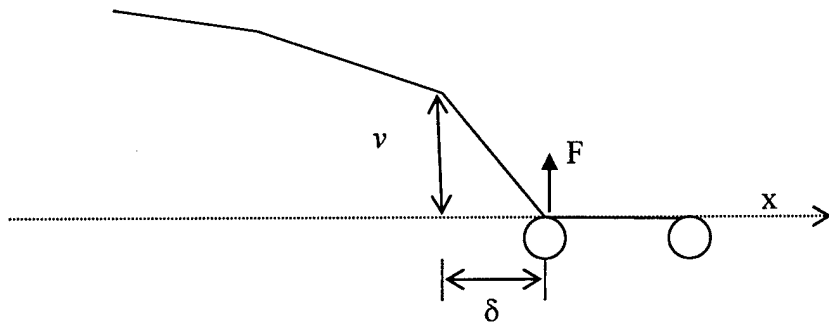


Figure 39. Variable definition for Virtual Crack Closure method in FEA model.

J-integral method is a method of path independent contour integral based on the theorem of energy conservation [74]. Its two-dimensional form can be written as:

$$G = J = \int_{\Gamma} (W dy - T \frac{\partial u}{\partial x} ds) \quad (36)$$

with

$$W = \int \sigma_{ij} d\varepsilon_{ij} \quad (37)$$

Γ is a closed contour followed counter clockwise (Figure 40) in a stressed solid, T is the tension vector perpendicular to Γ in the outside direction, $T_i = \sigma_{ij} n_j$, u is the displacement in the x-direction and ds is an element of Γ .

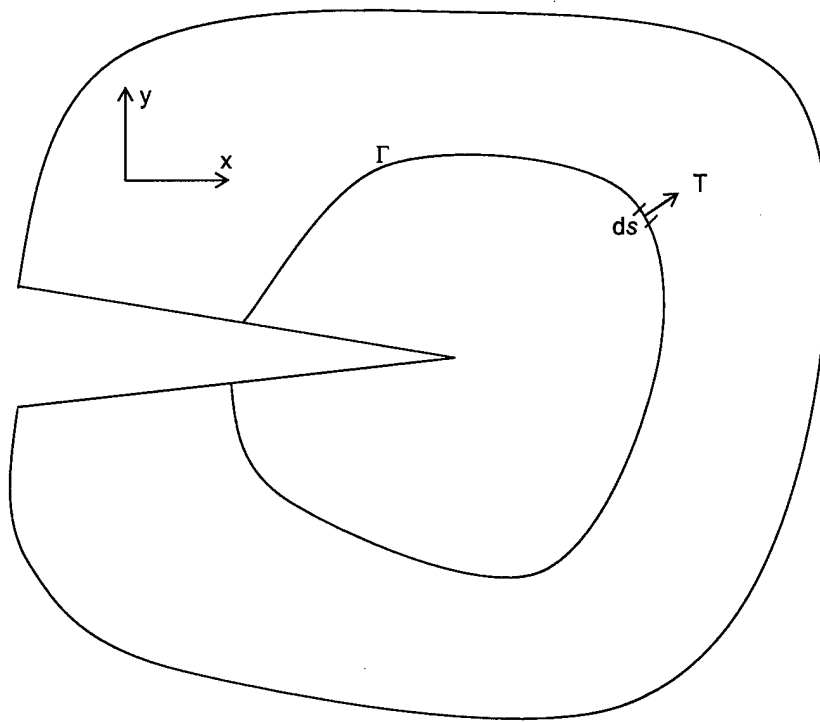


Figure 40. Definition of J-integral.

In order to evaluate the reliability of FEA fracture mechanics, the problem described in Figure 37 was calculated using the theoretical calculation method (Equations (29-30)), FEA Virtual Crack Closure method (Equation (35))^[73], and FEA J-Integral method (Equations (36-37))^[73]. To compare the effects of mesh density, different mesh densities are employed in the FEA models. The results are shown in Figures 41-42.

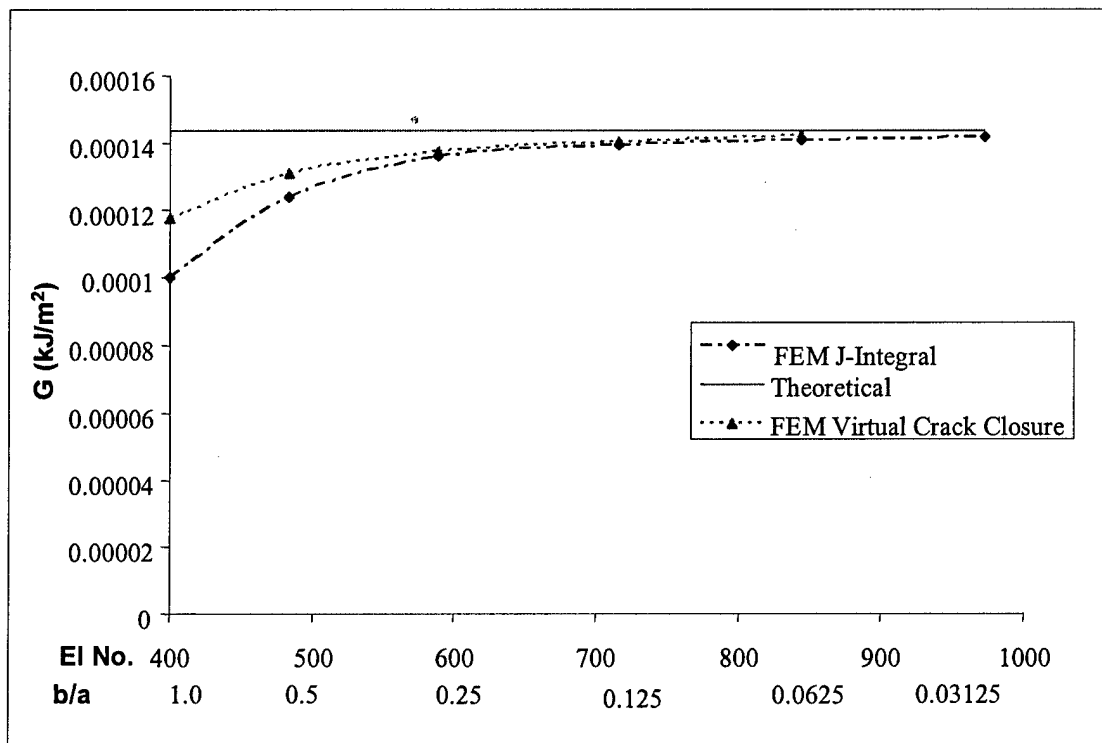


Figure 41. Results of energy release rate for different mesh densities. El. No. = number of elements in the whole model.

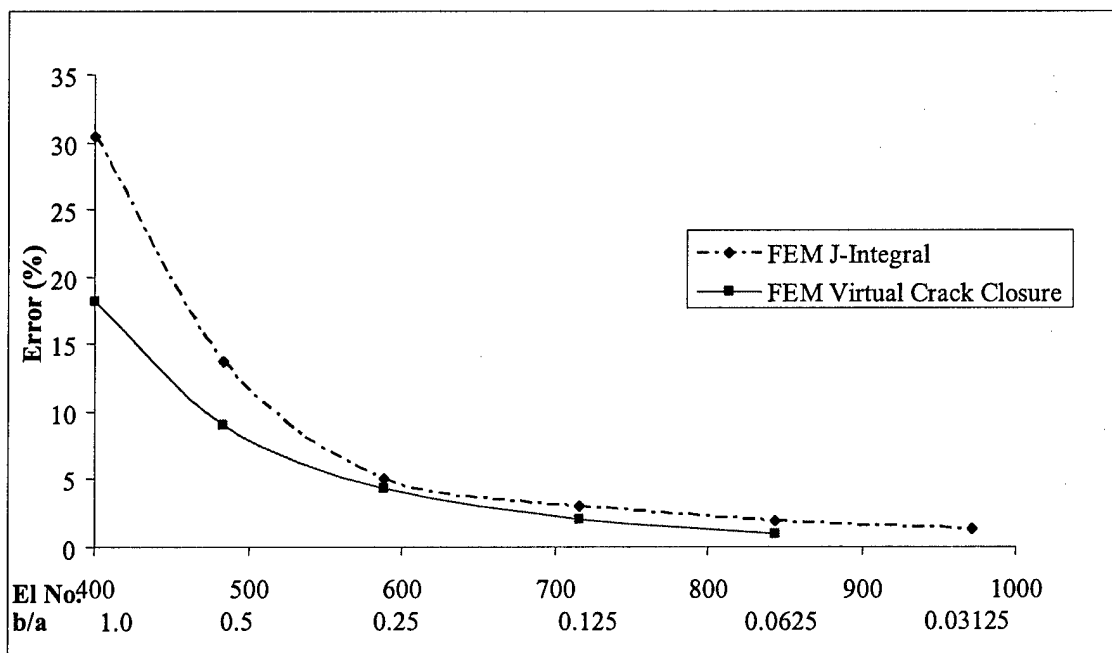


Figure 42. Accuracy of energy release rate for different mesh density. El. No. = number of elements in the whole model.

Error in Figure 42 was defined as:

$$Error = \frac{G_{FEA} - G_{Theory}}{G_{Theory}} \times 100\% \quad (38)$$

where G_{FEA} is the energy release rate result from FEA analysis (including two cases: FEA J-integral and FEA virtual crack closure), and G_{Theory} is the theory calculation results. The results in Figures 41-42 show that the error of FEA results decreases quickly with the decreasing of b/a . When b/a is less than 0.0312, the errors of both FEA methods (J integral and Virtual Crack Closure) are less than 1.5%. Coarse meshed FEA usually gives a negative error in prediction the energy release rate. The reason is that energy release rate is the function of stress and strain, and coarse meshed FEA usually gives lower stress and strain.

The results in Figures 43-44 show the accuracy of stress intensity factor K_I for different mesh densities. Error in Figure 44 was defined as:

$$Error = \frac{K_{I,FEA} - K_{I,Theory}}{K_{I,Theory}} \times 100\% \quad (39)$$

where $K_{I,FEA}$ is the energy release rate result from FEA analysis and $K_{I,Theory}$ is the theory calculation results. When b/a is less than 0.0312, the error of FEA J-integral method is less than 3%. For a fine meshed model, FEA results of stress intensity factor K_I have a poorer accuracy than those of energy release rate, but they are still acceptable. For coarse meshed model, K_I is even more accurate than energy release rate, because G is proportional to K_I^2 (Equation (29)).

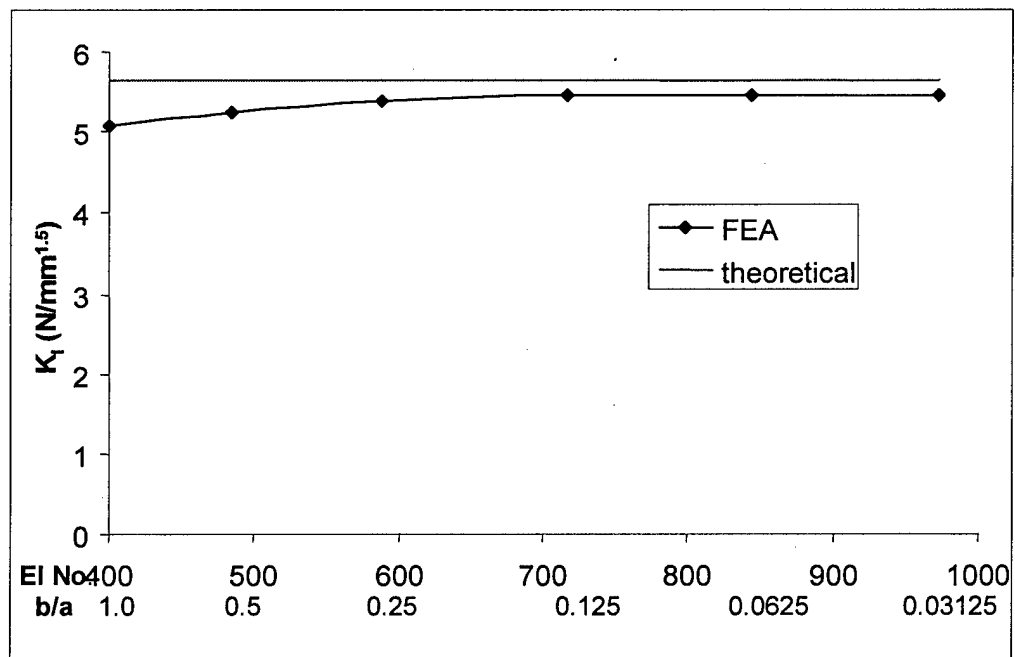


Figure 43. Results of stress intensity factor K_I for different mesh density. El. No. = number of elements in the whole model.

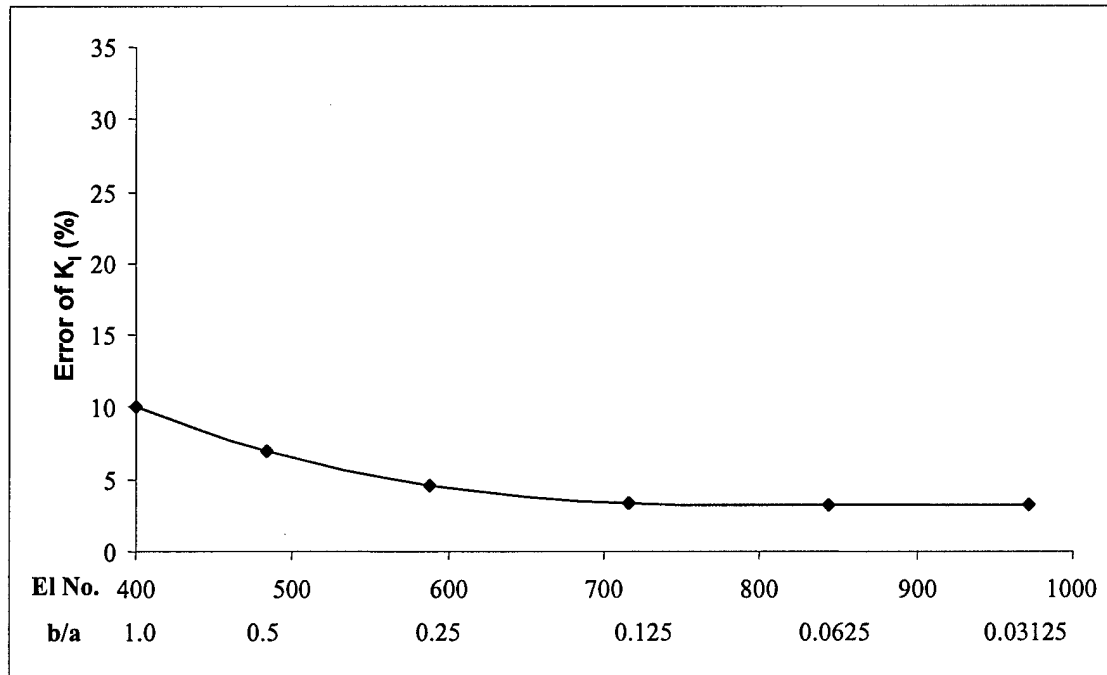


Figure 44. Results of stress intensity factor K_I for different mesh density. El. No. = number of elements in the whole model.

Figures 45-52 show the stress distribution near the crack (in a 20 mm × 60 mm rectangular region of Figure 37). We are interested in comparing the difference between the coarse meshed and fine meshed models. The white lines in the figures are the elements' edges. From these figures, we can conclude as following:

- (1) In most figures, the stress distributions are symmetric, except Figures 49 and 50, which show the distribution of shear stress. It is anti-symmetric respect to the x axis, because its direction changes.
- (2) The predicted maximum stress value is significantly affected by the mesh density around the crack tip. The fine meshed model gives a higher maximum value. Theoretically, the maximum stress goes to infinity at the crack tip.
- (3) The coarse meshed model shows high stress around the nodes with boundary conditions. This is a numerical error, which can be solved by increasing the mesh density.
- (4) The coarse meshed model predicted the location of the maximum shear stress is in the center of the crack. In the fine meshed model, the maximum shear stress is near the crack tip. Obviously, the latter is more reasonable.
- (5) Comparing with the fine meshed model, the coarse meshed model usually gives a bigger high stress region with the lower maximum stress.

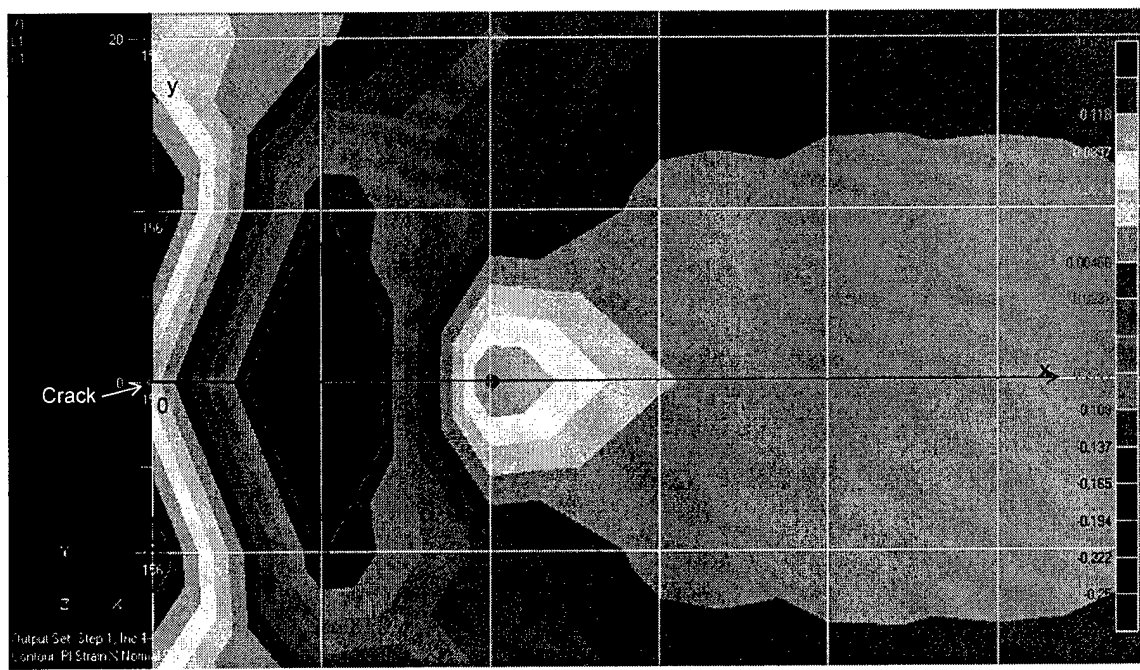


Figure 45. σ_x distribution around the crack tip in the rectangular bar model ($b/a = 1$)
 Maximum stress: 0.175 MPa, location: nodes with boundary condition;
 Minimum stress: - 0.279 MPa, location: the crack tip.

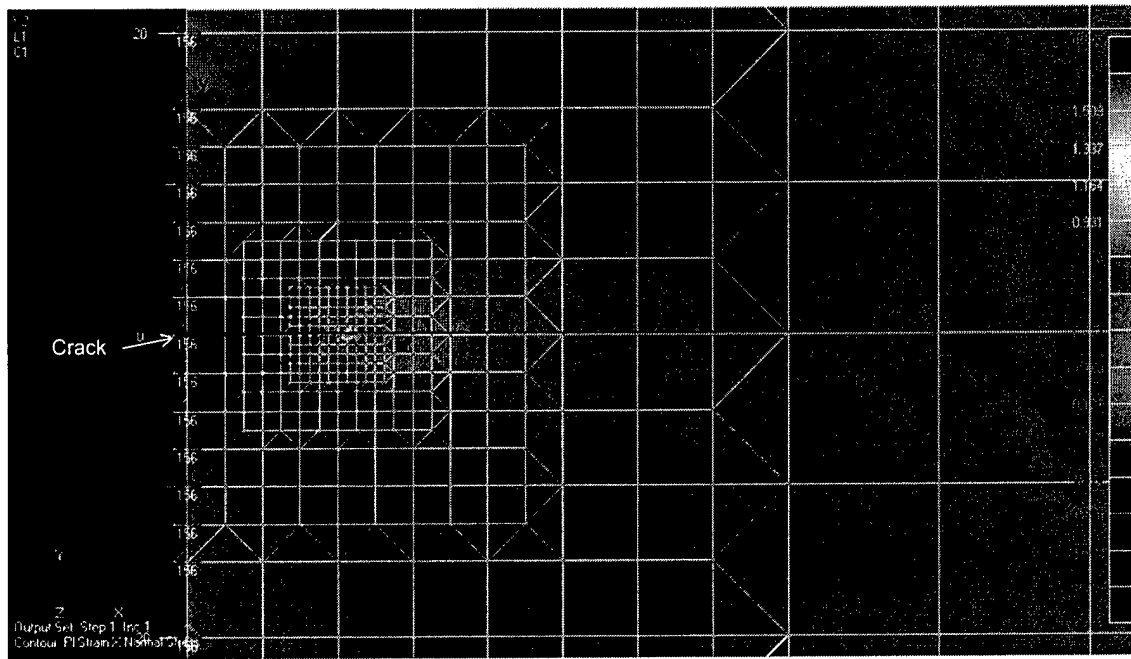


Figure 46. σ_x distribution around the crack tip in the rectangular bar model ($b/a = 0.0625$)
 Maximum stress: 1.855 MPa, location: in front of the crack tip;
 Minimum stress: - 0.909 MPa, location: after the crack tip.

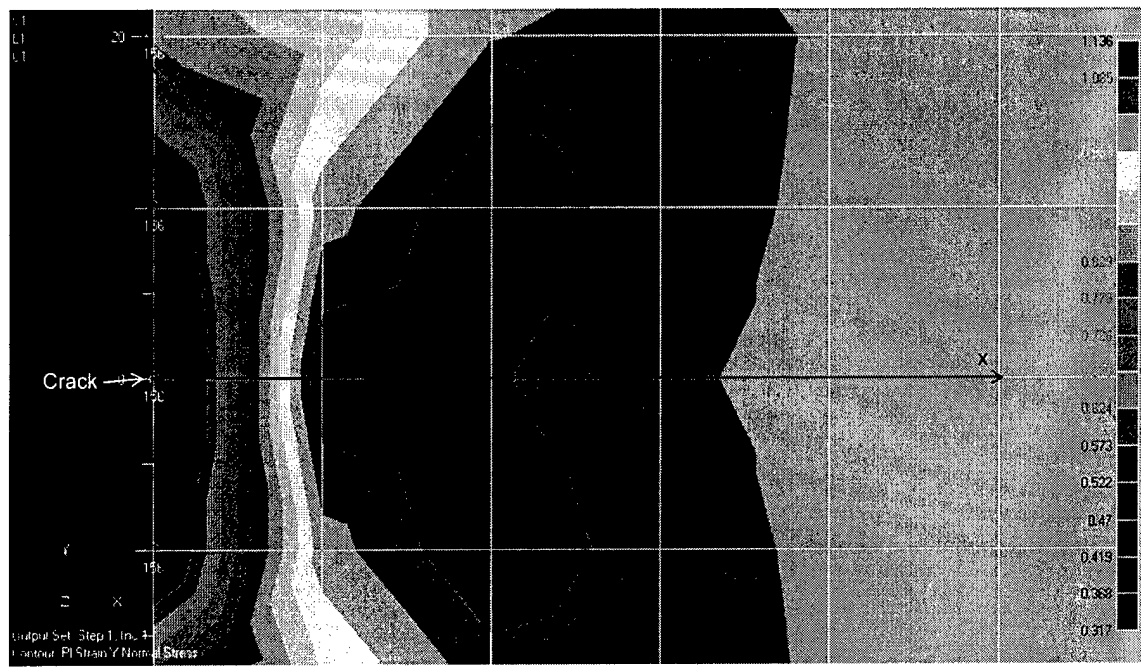


Figure 47. σ_y distribution around the crack tip in the rectangular bar model ($b/a = 1$)
 Maximum stress: 1.136 MPa, location: in front of the crack tip;
 Minimum stress: 0.317 MPa, location: center of the crack.

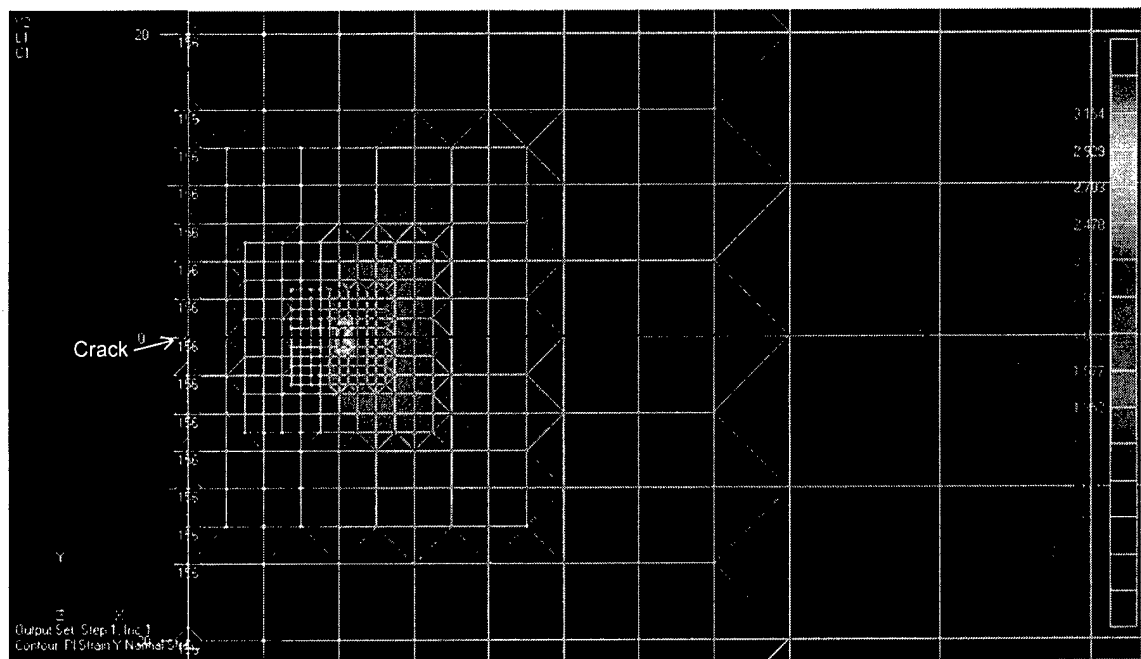


Figure 48. σ_y distribution around the crack tip in the rectangular bar model ($b/a = 0.0625$)
 Maximum stress: 3,604 MPa, location: in front of the crack tip;
 Minimum stress: 0 MPa, location: center of the crack.



Figure 49. τ_{xy} distribution around the crack tip in the rectangular bar model ($b/a = 1$).
 Maximum stress: 0.734 MPa, location: below the center of the crack;
 Minimum stress: -0.734 MPa, location: above the center of the crack.

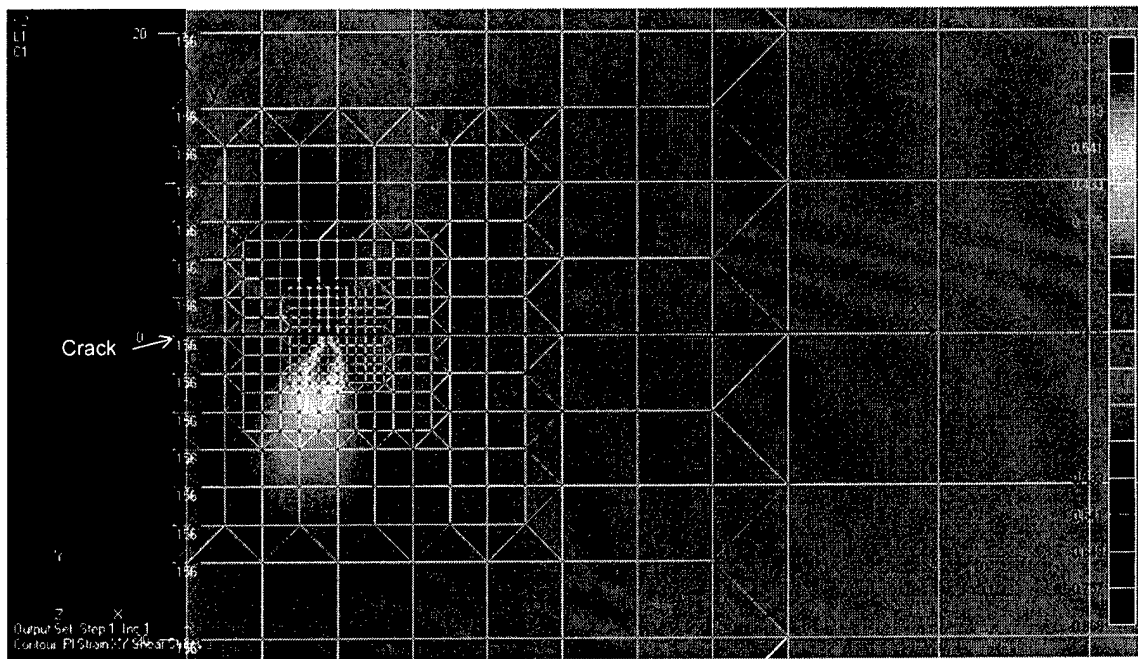


Figure 50. τ_{xy} distribution around the crack tip in the rectangular bar model ($b/a = 0.0625$). Maximum stress: 0.866 MPa, location: below the tip of the crack; Minimum stress: -0.866 MPa, location: above the tip of the crack.

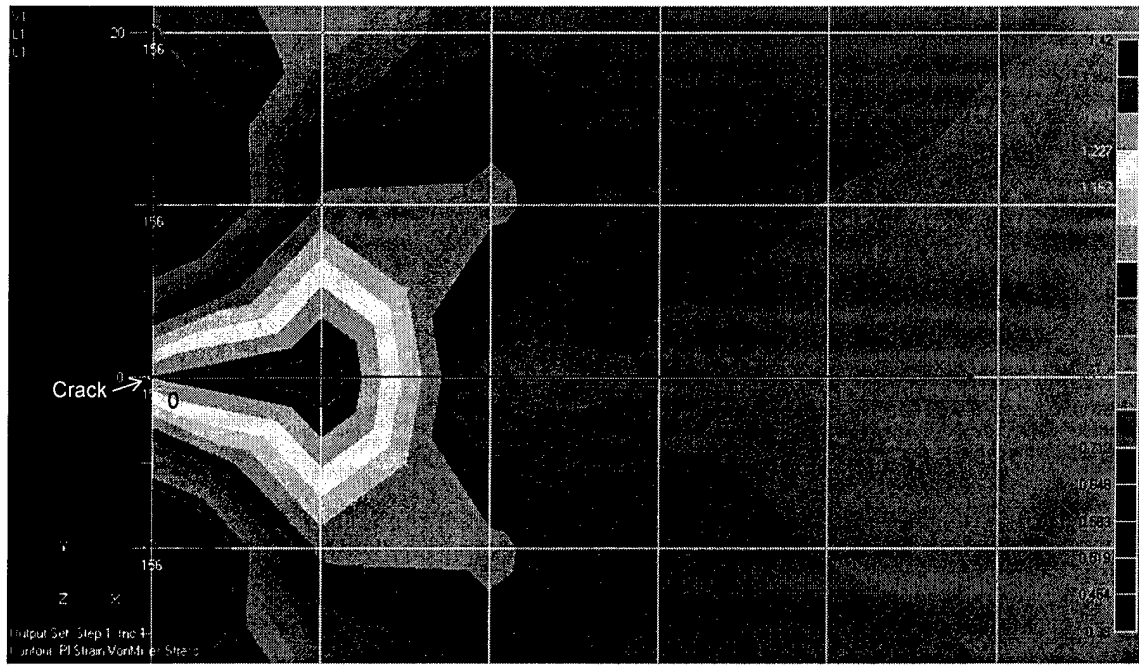


Figure 51. VonMises stress distribution around the crack tip in the rectangular bar model ($b/a = 1$) Maximum stress: 1.42 MPa, location: around the crack tip; Minimum stress: 0.39 MPa, location: nodes with boundary conditions.

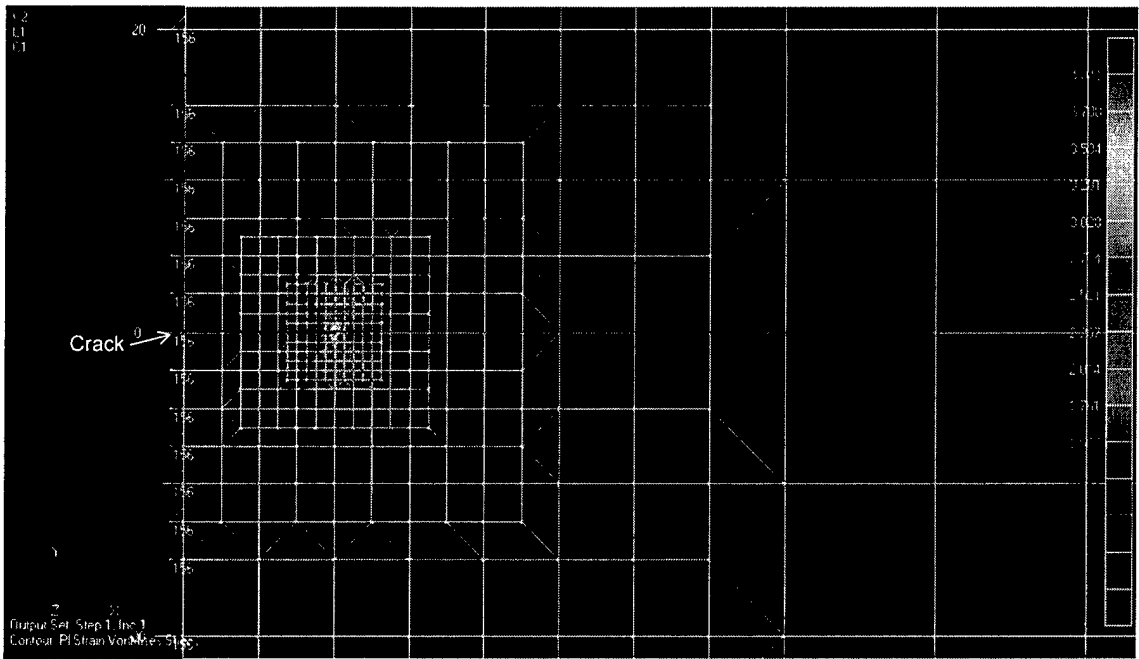


Figure 52. VonMises stress distribution around the crack tip in the rectangular bar model ($b/a = 0.0625$). Maximum stress: 4.294 MPa, location: in front of the crack tip; Minimum stress: 0.241 MPa, location: nodes with boundary conditions.

B. Model of Single Strap Adhesive Joint (with external parallel crack)

The initial crack in this model is parallel to the adhesive/adherend interfaces, (later we allow its position relative to the joint centerline to change, see Figure 53). In Figure 53, a is the crack length, h is the crack position relative to the adhesive layer centerline, and σ is the displacement load. In this section, the initial crack is always parallel to the adhesive/adherend interface, $a = 2$ mm, and we enforce here that $h = 0$. b is again the side length of the smallest finite elements in the model (which are not shown in Figure 51). The mesh density varies, i.e., b varies. The other dimensions are as follows: $L = 120$ mm, $L_o = 20$ mm, $t_1 = t_2 = 3$ mm, and $t_3 = 0.13$ mm. The material properties of adherends are $E = 70$ GPa, $\nu = 0.3$. The material properties of the adhesive layer are given as $E = 2.2$ GPa, $\nu = 0.4$.

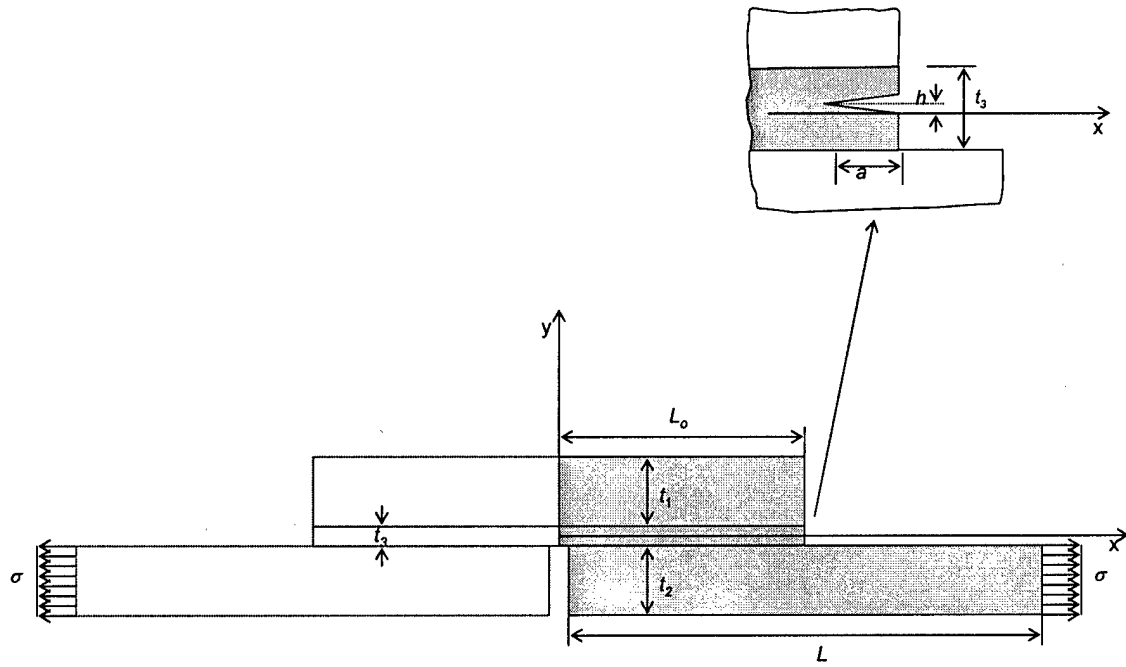


Figure 53. FEA model for outer parallel crack (crack position: $x = 20$ mm).

The results of the model in Figure 53 (with different mesh densities) are shown in Figures 54-57. As the geometry of single strap adhesive joints is relatively complex, it is difficult to provide a theoretical result. Figures 54-57 show only the FEA results.

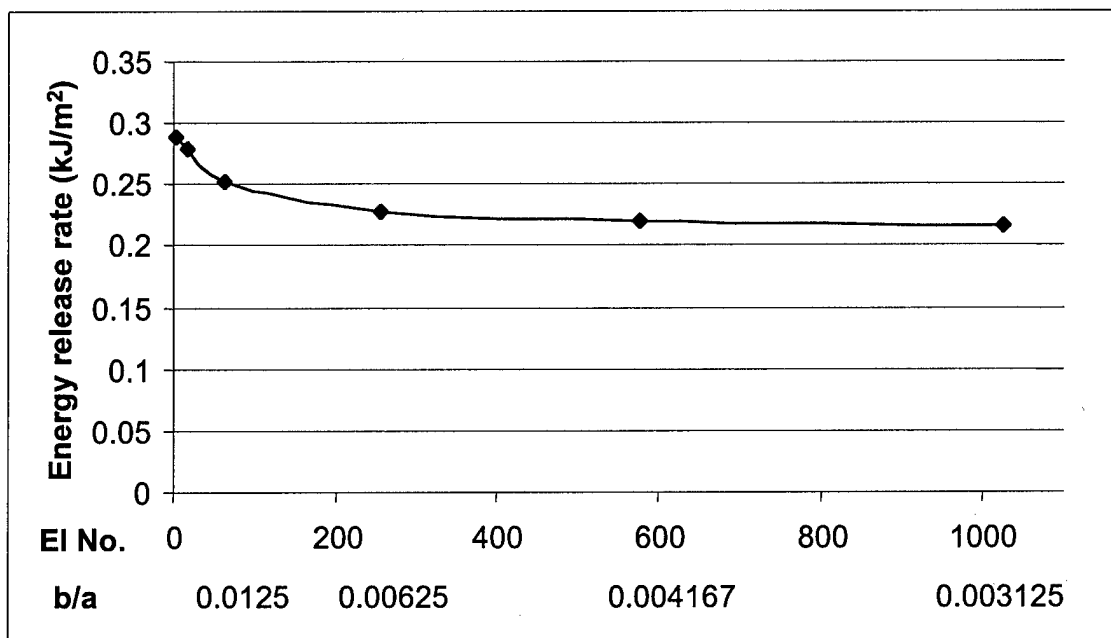


Figure 54. Results of energy release rate for different mesh densities, and $h = 0$. El. No. = number of elements in a $0.2 \times 0.2 \text{ mm}^2$ area around the crack tip. For the 1st data point, $b/a = 0.05$.

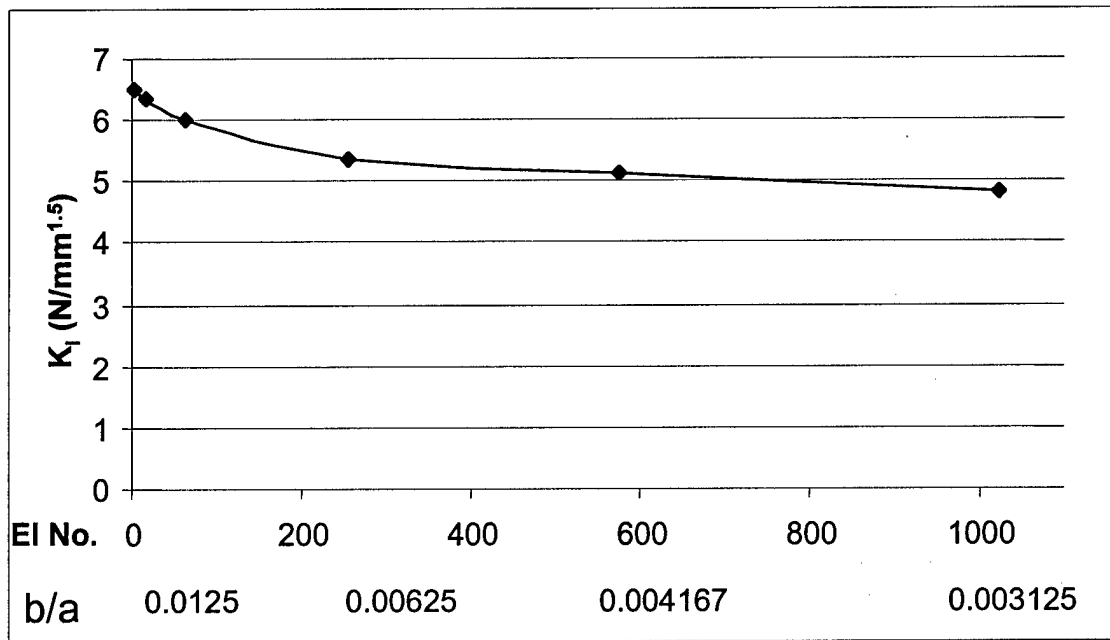


Figure 55. Results of K_I for different mesh densities, and $h = 0$. El. No. = number of elements in a 0.2×0.2 mm² area around the crack tip. For the 1st data point, $b/a = 0.05$.

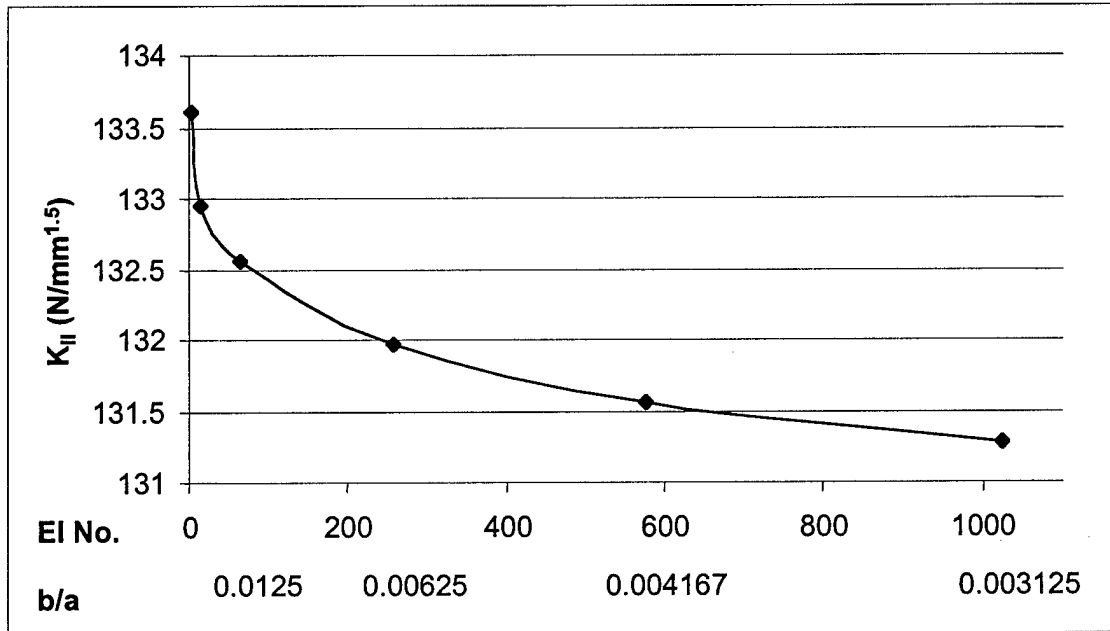


Figure 56. Results of K_{II} for different mesh densities, and $h = 0$. El. No. = number of elements in a 0.2×0.2 mm² area around the crack tip. For the 1st data point, $b/a = 0.05$.

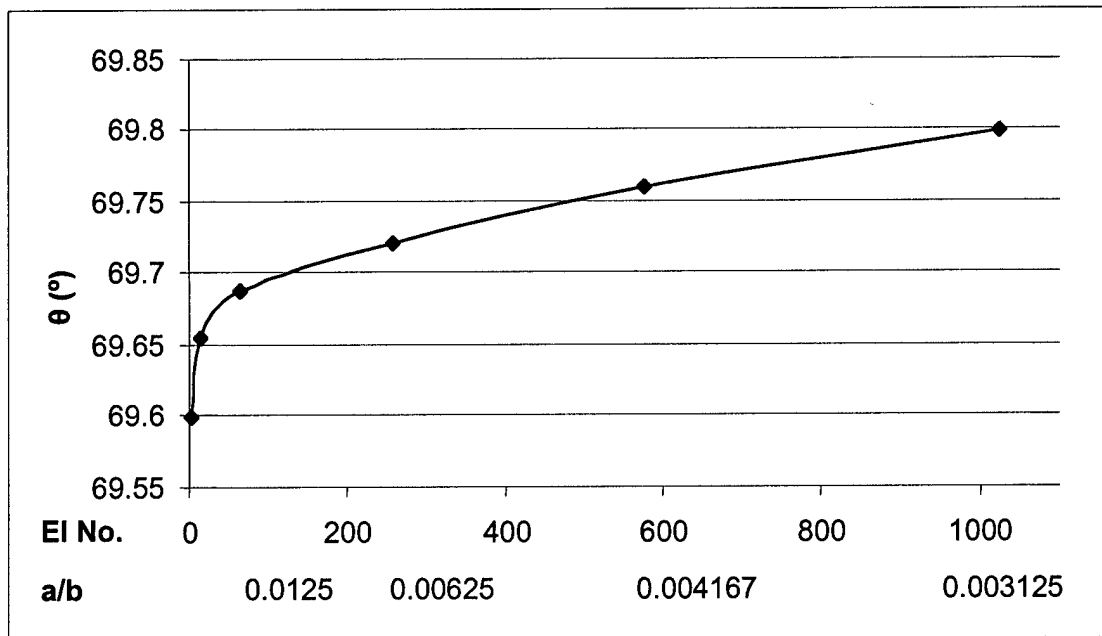


Figure 57. Results of K_{II} for different mesh densities, and $h = 0$. EI No. = number of elements in a $0.2 \times 0.2 \text{ mm}^2$ area around the crack tip. For the 1st data point, $b/a = 0.05$.

From Figures 54 -57, we concluded as follows:

- (1) When b/a changed from 0.5 to 0.00625, Energy release rate (G) and stress intensity factors (K_I and K_{II}) all significantly reduced. But they all tend toward a constant value as b/a is made less than 0.004.
- (2) Energy release rate (G) is the most sensitive to the mesh density. When $b/a = 0.05$, the value of G is 33% bigger than $b/a = 0.003125$. The crack propagation direction (θ) is not as sensitive to mesh density, changing only -0.2% when b/a changed from 0.05 to 0.003125. The reason may be that energy release rate (G) is a function for stress and strain, both of which are mesh sensitive; and crack propagation direction (θ) is determined by the direction of maximum principle stress, which is not mesh sensitive.

(3) It is reasonable to assume $b/a = 0.004$ is a suitable mesh density for FEA fracture mechanics analysis of single strap adhesive joints. Because the theoretical results for energy release rate (G), stress intensity factors (K_I and K_{II}) and crack propagation direction (θ) are not available for a single strap joint, we can't calculate the error of FEA fracture mechanics method in this section. But from (1) we know when $b/a = 0.004$, further increase of the mesh density doesn't change the results significantly.

5.3 EFFECTS OF EXTERNAL CRACKS ON THE SINGLE STRAP JOINT

The external initial cracks with different directions, lengths, and positions are studied in this section. The effects on the energy release rate and the crack propagation direction are discussed for different locations and directions of initial external parallel cracks. There were two models used in this section:

1. The center of the initial crack is on the centerline of the initial crack, but the direction of the initial crack is changing (see Figure 58). This model is used to compare the effects of the initial crack direction, and is called the "external aparallel crack".

2. The initial crack is parallel to the adhesive/adherend interfaces, but its position is changing (see Figure 53). This is model, called the "external parallel crack", was developed to compare the effects of the initial crack position.

A. Effects of the Initial External Crack Directions

Figure 58 shows a crack located in the free edge of the adhesive layer ($x = 20$ mm). The dimensions used in Figure 58 are as follows: $L = 120$ mm, $L_o = 20$ mm, $t_1 = t_2 = 3$ mm, and $t_3 = 0.2$ mm. a is the crack length, which is equal to 0.11 mm in this section. The material properties for the adherends are Young's modulus is 70 GPa; Poisson's ratio is 0.33. For the adhesive, the Young's modulus is 2.6 GPa, and the Poisson's ratio is 0.4. A displacement load of 0.5 mm was applied in this model. Figure 59 provides other variable definitions used in this section.

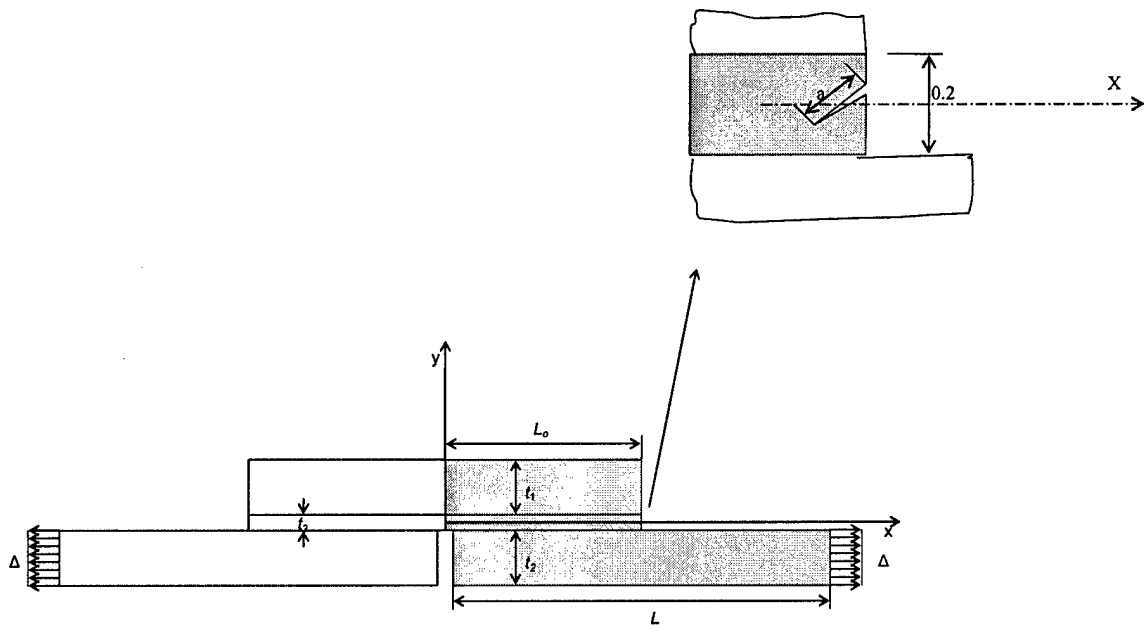


Figure 58. Model for the direction effects of external crack in adhesive joints study.

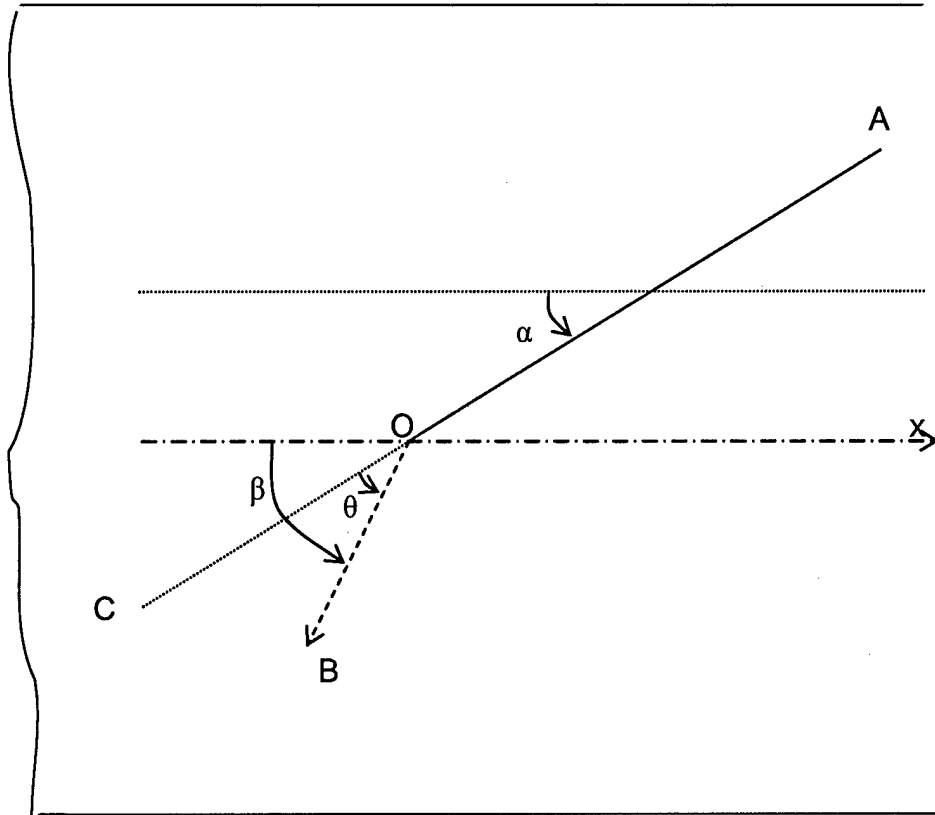


Figure 59. Variable definition for initial crack directions effects study.

In Figure 59, the line OA is the initial crack; the point O is the crack tip; OB is the propagation direction for the crack OA; α is the angle between the crack direction and the x-axis; θ is the crack propagation direction; and β is the angle between the crack propagation direction and the x-axis. Angle β is the direction of the crack propagation relative to the adhesive primary coordinate x, and is the sum of the angles α and θ :

$$\beta = \alpha + \theta \quad (40)$$

A numerical experiment was carried to study the effects of initiate crack direction (α) on the energy release rate (G), stress intensity factors (K_I and K_{II}) crack propagation direction (β and θ).

The model shown in Figure 59 was run several times using ABAQUS. Every time, the initial crack direction was changed. All other conditions, such as the crack length, the mesh density, the loading, the dimension and the material properties, kept the same. Results are shown in Figures 60-62.

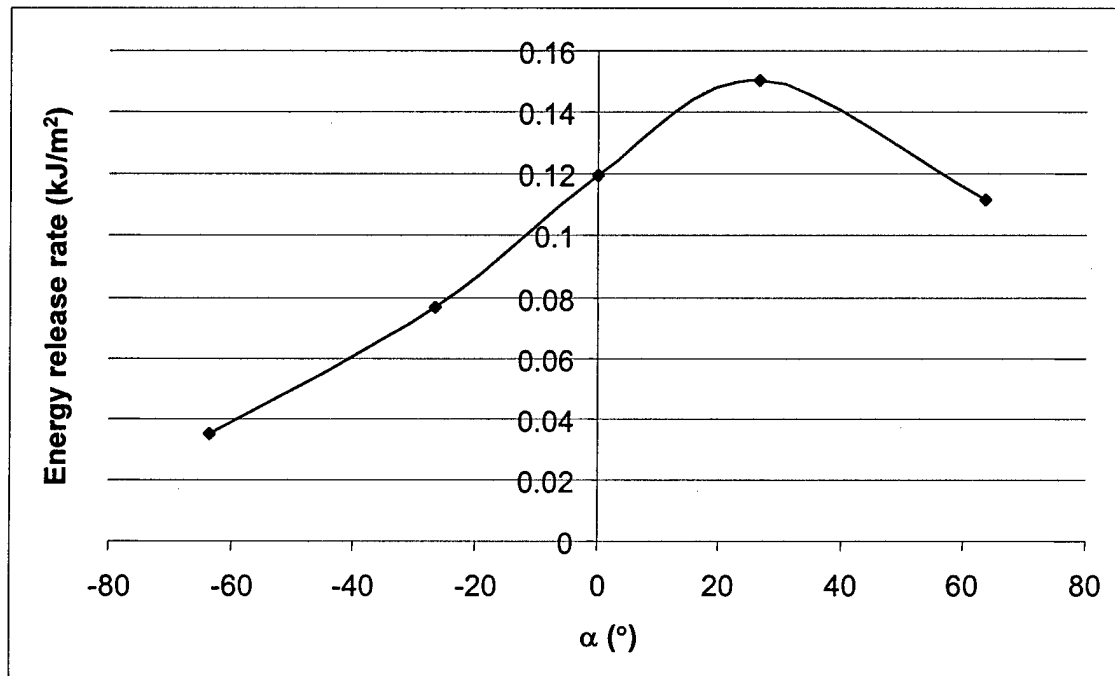


Figure 60. Energy release rate sensitivity of the initial external crack directions.

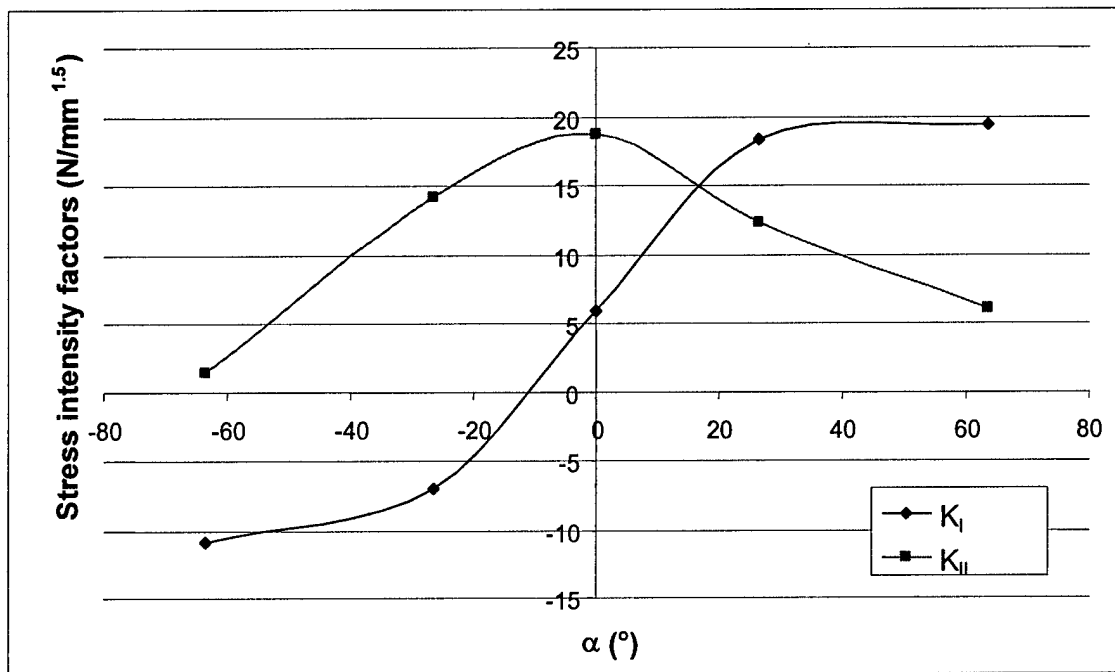


Figure 61. Stress intensity factors sensitivity of the initial external crack directions.

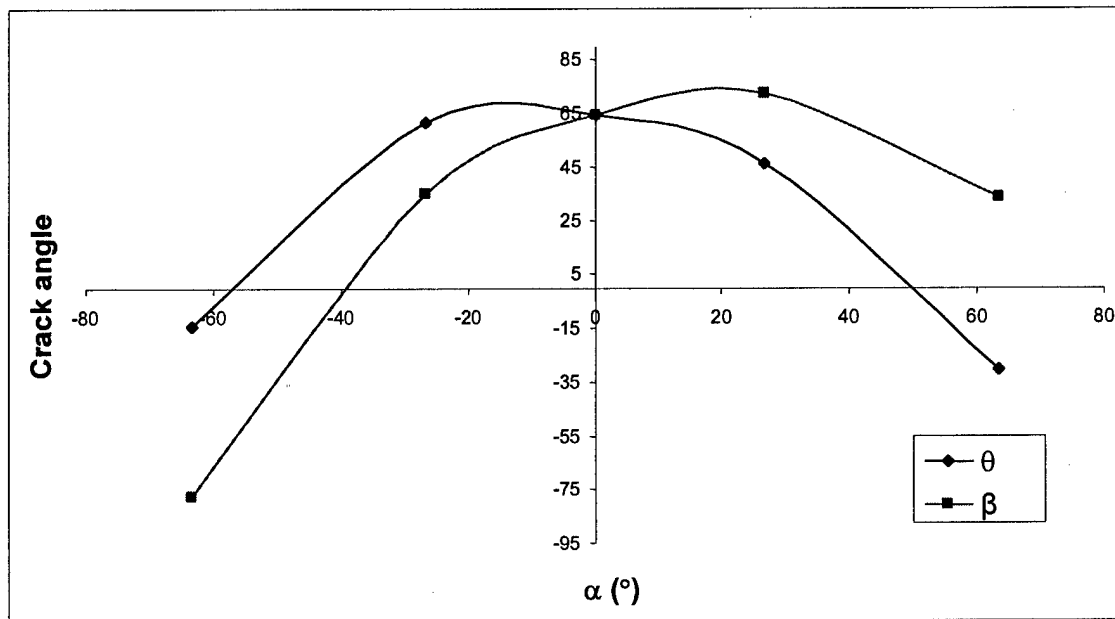


Figure 92. Crack propagation direction sensitivity of the initial external crack directions.

Figures 61-62 show that initial crack direction α can significantly affect the energy release rate, stress intensity factors, and propagation direction. These figures revealed that:

- (1) The energy release rate reaches a maximum value when $\alpha = 35^\circ$.
- (2) The effect of Mode I loading (shown by the curve of K_I) monotonically increases with increased angle of initial crack; but the effects of Mode II loading has a maximum value at $\alpha = 0$ (horizontal crack). These results are reasonable. When $\alpha < 0$, the crack tip subjects to a compression force, so K_I is small. When $\alpha > 0$, there is a tensile force applied on the crack tip. It results a larger K_I . K_{II} reaches its maximum at $\alpha = 0$ because the shear force is biggest in this moment. These results are also consistent with the results of the energy release rate. At the position of the maximum value of energy release rate, both K_I and K_{II} have relatively high values.
- (3) Once the angle of the initial crack (α) is less than -10° , K_I is negative, which means compression, and it has no effect on crack propagate. In this case, the crack propagates only under the effect of the Mode II leading.
- (4) If the initial crack direction α is -57° , the crack propagation angle θ is 0° . The crack would propagate in an angle of -57° to the x axis (β), which means $\alpha = \beta$. The crack would then propagate to the top interface of the adhesive. Once α is larger than -57° , θ is larger than 0° and β would be bigger than α , which would make the crack go to a larger angle of β in the next step. Thus if the adhesive is thick enough, the crack would eventually proceed to the bottom adhesive interface. If α is less than -57° , $\beta < \alpha$, and the crack would reach the top adhesive interface. $\alpha = -57^\circ$ is the critical value, i.e., when $\alpha = \beta$ ($\theta = 0^\circ$). It is also the critical value to determine the

eventual crack position. Figure 63 shows the crack propagating paths for different initiate directions.

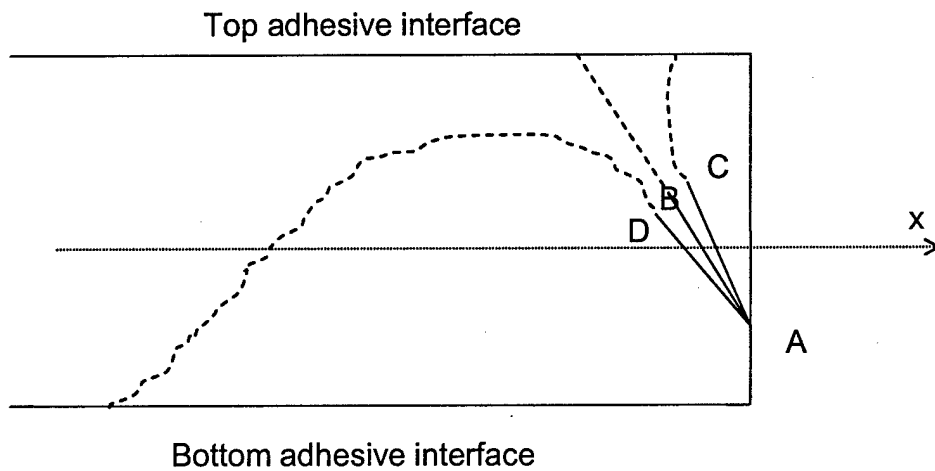


Figure 63. Crack propagating paths. AB is the crack with the direction of -57° , AC shows a crack with the initial direction less than -57° , and AD shows a crack with the initial direction larger than -57° .

In Figure 63, AB is the crack with the direction of -57° . As $\alpha = \beta$ in this case, the crack propagates in a straight line, and goes to the top adhesive interface. AC shows a crack with the initial direction less than -57° ; it would also reach the top interface of the bond line. AD shows a crack with the initial direction bigger than -57° . It may reach the bottom interface or the top interface of the bond line, depending on the bond line thickness.

The direction of initial crack (α) has significant effects on the energy release rate (G) and stress intensity factors (K_I and K_{II}), but the most important is the effect on the crack propagate direction (β). From the discussion above, we found that the crack is not common to keep

INVESTIGATION OF ADHESIVE JOINTS FOR NANO-ENGINEERING AND MODELING

propagating in the middle of the adhesive layer. More likely, the crack would reach the interface, and propagate along the interface. It is important the initial crack direction can determine the crack approach the top interface or the bottom interface.

B. Effects of initial crack lengths and positions

The model to simulate the external parallel crack is given in Figure 53. In Figure 53, a is the crack length, h is the crack position to the adhesive layer centerline, and σ is the displacement load. In this model, the initial crack is always parallel to the adhesive/adherend interface, but we now let its length (a) and position (h) vary. The dimensions are as follows: $L = 120$ mm, $L_o = 20$ mm, $t_1 = t_2 = 3$ mm, and $t_3 = 0.2$ mm. The material properties of adherends are $E = 70$ GPa, $\nu = 0.3$. The material properties of the adhesive layer are given as $E = 2.2$ GPa, $\nu = 0.4$. Figures 64 - 67 show the effects of initial crack lengths and positions for the external parallel cracks on energy release rate (G), stress intensity factors (K_I and K_{II}), and crack propagation direction (θ).

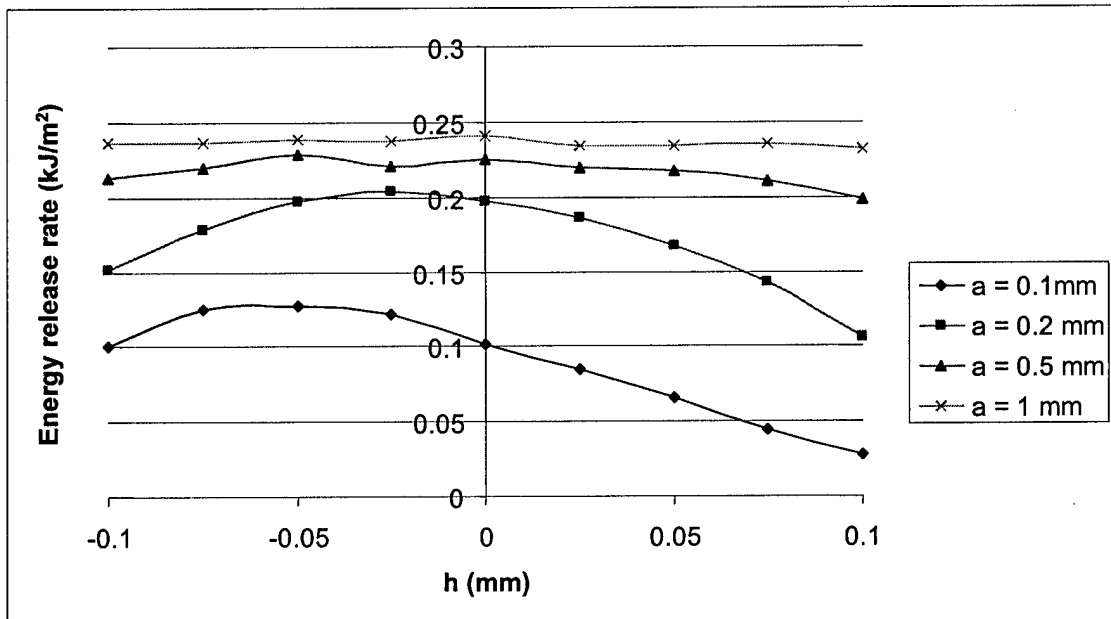


Figure 64. Energy release rate sensitivity of external parallel crack length and position.

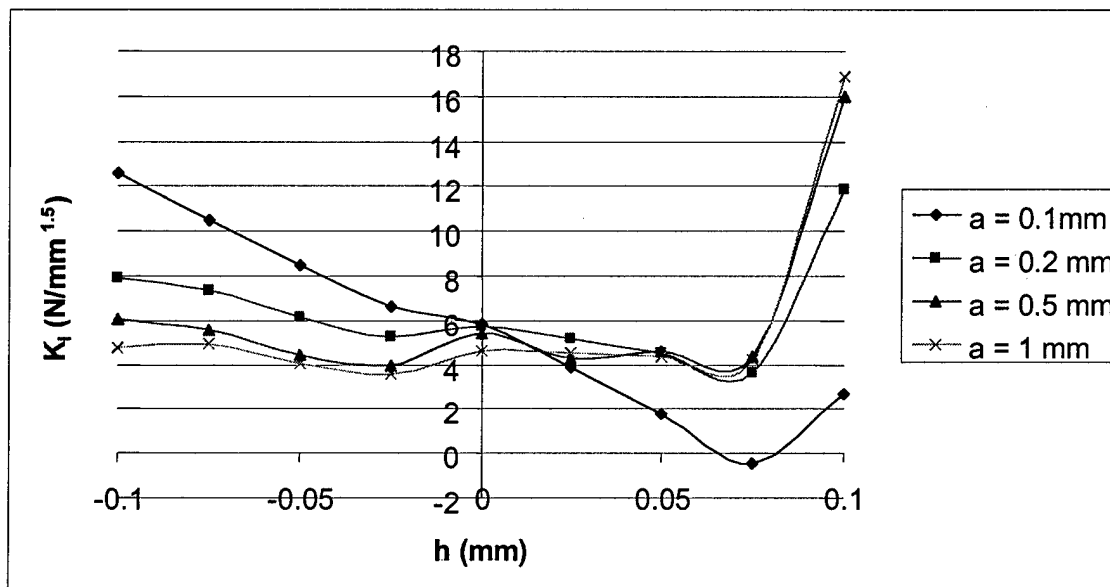


Figure 65. K_I Sensitivity of external parallel crack length and position

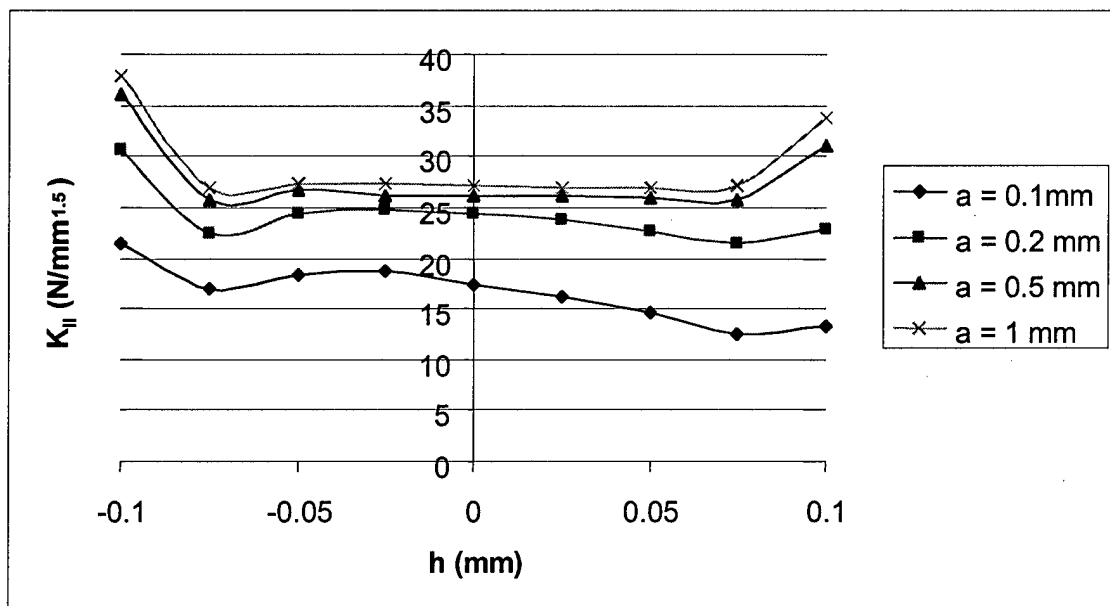


Figure 66. K_{II} sensitivity of external parallel crack length and position.

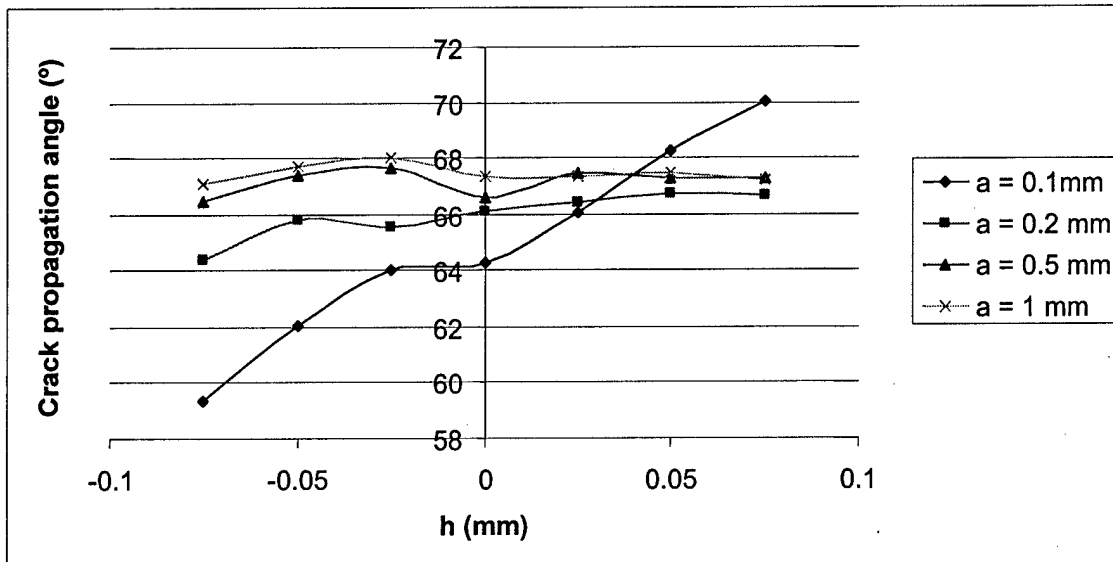


Figure 67. Crack propagation direction θ sensitivity of external parallel crack length and position.

Figure 64 - 67 tell us that for the external parallel crack, the energy release rate would increase with increasing crack length. For short initial crack length, the crack position can change the energy release rate significantly. Crack position doesn't have a big affect on long cracks ($a > 1$ mm). Crack position has only a small effect on the crack propagation direction. Both of the stress intensity factors (K_I and K_{II}) are significantly increased with the crack at the adherend/adhesive interface ($h = \pm 0.1$ mm). This means the stress concentration is significant on the interface. However energy release rate can not show this phenomenon (Figure 64). This highlights why the stress intensity factors are also important design parameters for adhesive joint design. Comparing the value of K_I and K_{II} (Figure 65 and 66), we found the value of K_{II} is much larger than K_I . So Case II loading (shear) has a more significant effect on the failure of single-strap adhesive joints. The crack propagation direction is generally around 66° , and slightly sensitive to crack position h for short cracks. The curves of energy release rate usually have a

maximum value close to $h = 0$ (Figure 64). This is because that the energy release rate is a function of both stress and strain, and the high modulus aluminum adherends restrict the deformation of adhesive, especially for the adhesive very close to the adherends. K_I and K_{II} generally decrease with increase of h , except the interface positions (Figures 64 and 65). It is reasonable. The larger is h , the farther away the crack is from the bottom adherend, where the loading come from. When the crack length a increases, in most location, K_I tends to decrease but K_{II} tends to increase (Figures 64 and 65). It means peeling effects are significant for short cracks, and shear effects are significant for long cracks. Some irregular data distributions are found when their values are close. This is believed to be numerical errors.

5.4 EFFECTS OF INTERNAL CRACKS ON SINGLE STRAP JOINTS

The static stress analysis (Figures 34-36) shows that the stress concentration in the center of a single strap adhesive joint is much more serious than that on its edge, so a crack is more likely to propagate from the center. The effects of internal cracks on a single strap joint are studied in this section.

Initial internal cracks with different directions, lengths, and positions are studied. The effects on the energy release rate and the crack propagation direction are discussed for different locations and directions of initial internal parallel cracks. Two models were used in this section:

1. The center of the initial crack is on the centerline of the adhesive layer, but the direction of the initial crack is changing (see Figure 68). This model is used to compare the effects of the initial crack direction, and is called the "internal aparallel crack"

2. The initial crack is parallel to the adhesive/adherend interfaces, but its position is changing (see Figure 73). It is called the “internal parallel crack”. This model compares the effects of the initial crack position.

A. Effects of the Initial Internal Crack Directions

Figure 68 shows a crack located in the center of the adhesive layer ($x = 0$). The dimensions used in Figure 68 are as follows: $L = 120$ mm, $L_o = 20$ mm, $t_1 = t_2 = 3$ mm, and $t_3 = 0.2$ mm. a is the crack length, which equals 0.1 mm in this section. The material properties for the adherends are Young’s modulus is 70 GPa; Poisson’s ratio is 0.33. For the adhesive, the Young’s modulus is 2.6 GPa, and the Poisson’s ratio is 0.4. A displacement load Δ of 0.5 mm was applied in this model. Figure 69 provides the variable definition used in this section.

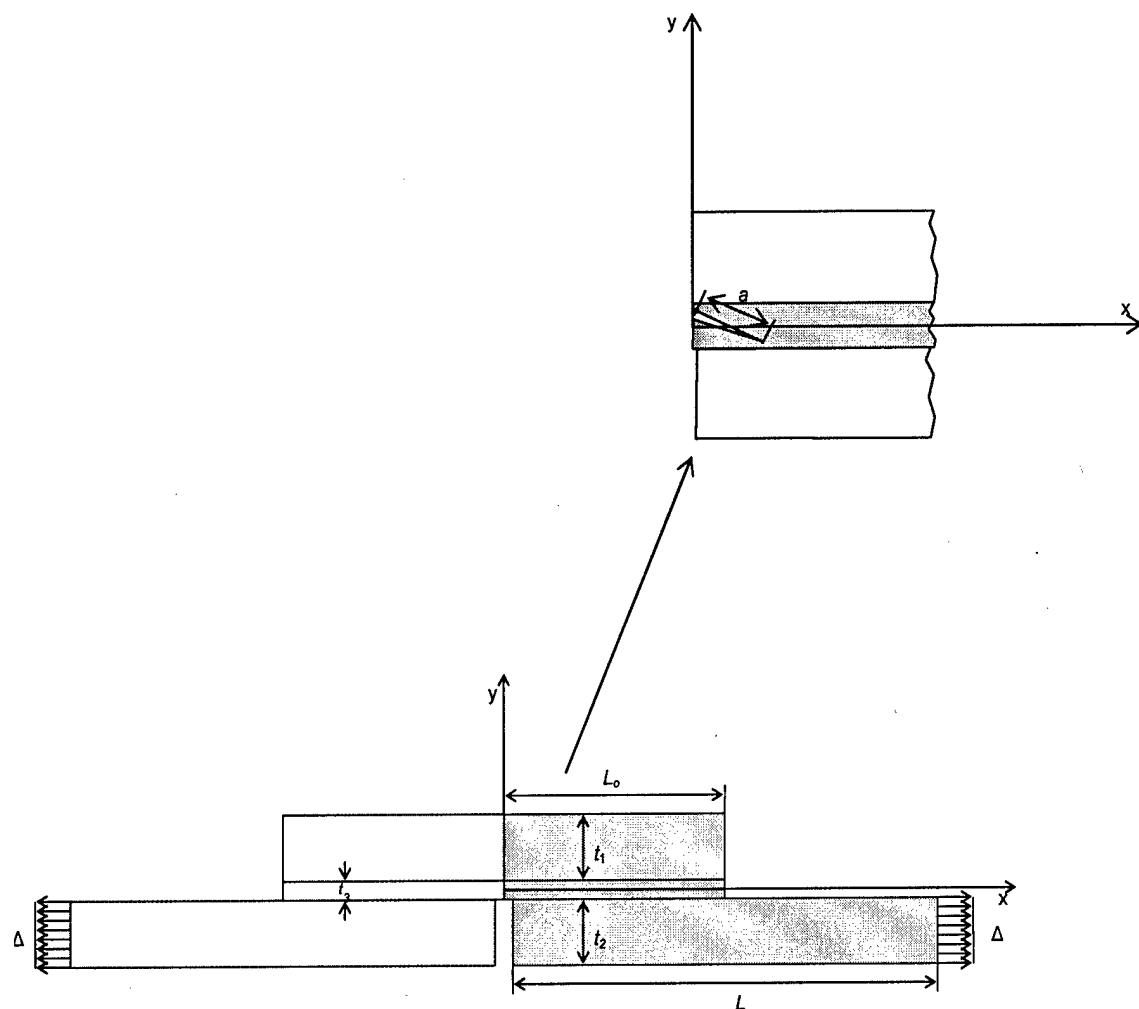


Figure 68. Model for the direction effects of internal initial crack study.

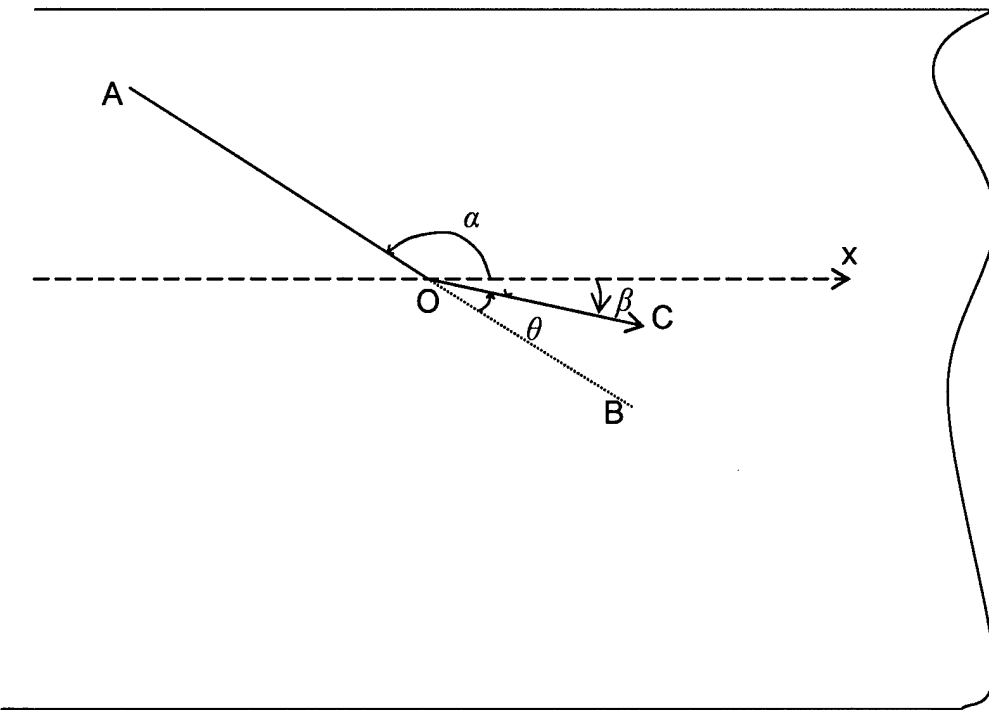


Figure 69. Variable definition for the internal crack propagation cases.

In Figure 69, O is the crack tip, AO is the initial crack, OC is the propagation direction of the crack, and the point B is in the line of AO. The x-axis is parallel to the adherend/adhesive interface. α is the angle between the x-axis and the initial crack AO, θ is the crack propagation angle (the angle between BO and CO), and β is the angle between the x-axis and CO. The counter-clock direction is positive for all of these three angles. So for this problem, the range of α is $90^\circ - 270^\circ$, and the calculation for β is:

$$\beta = \alpha + \theta - 180^\circ \quad (41)$$

Figures 70-72 show the energy release rate (G), the stress intensity factors (K_I and K_{II}), and the crack propagation direction (θ) are functions of initial crack direction (α).

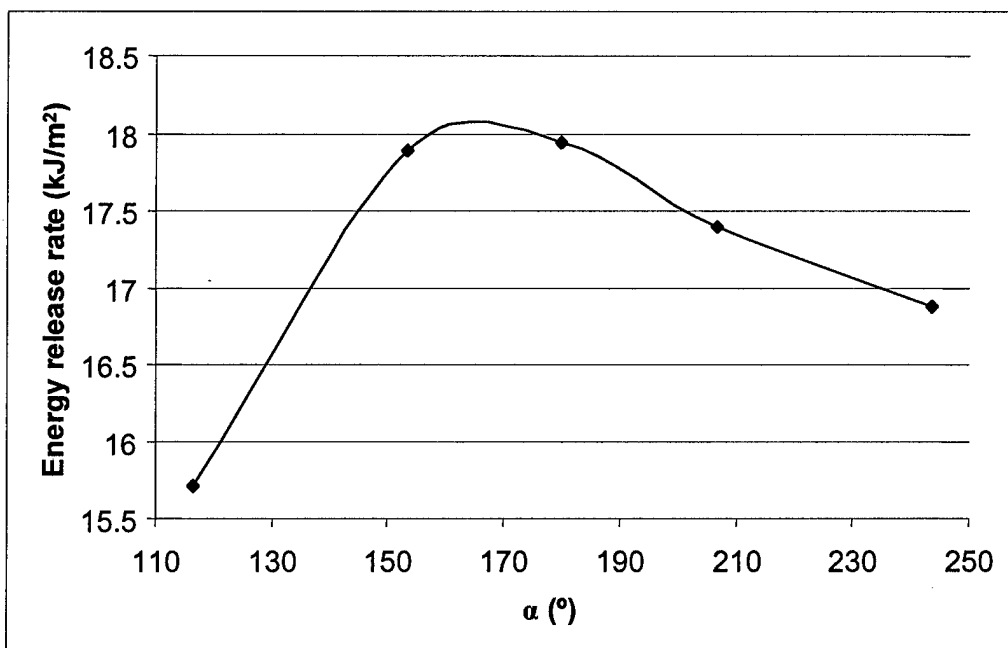


Figure 70. Energy release rate sensitivity to the initial internal crack direction.

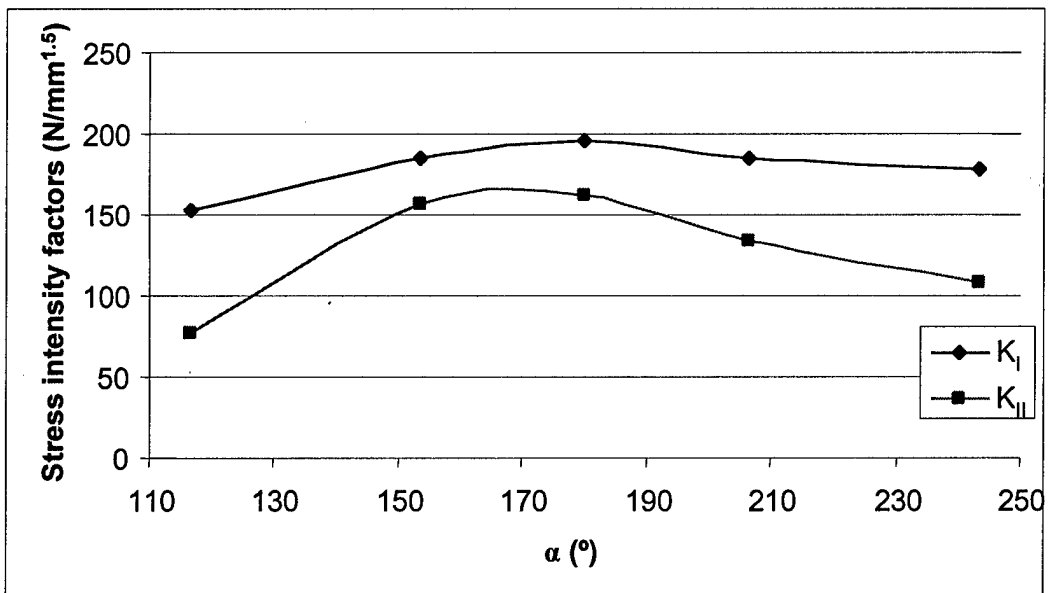


Figure 71. Stress intensity factors sensitivity to the initial internal crack direction.

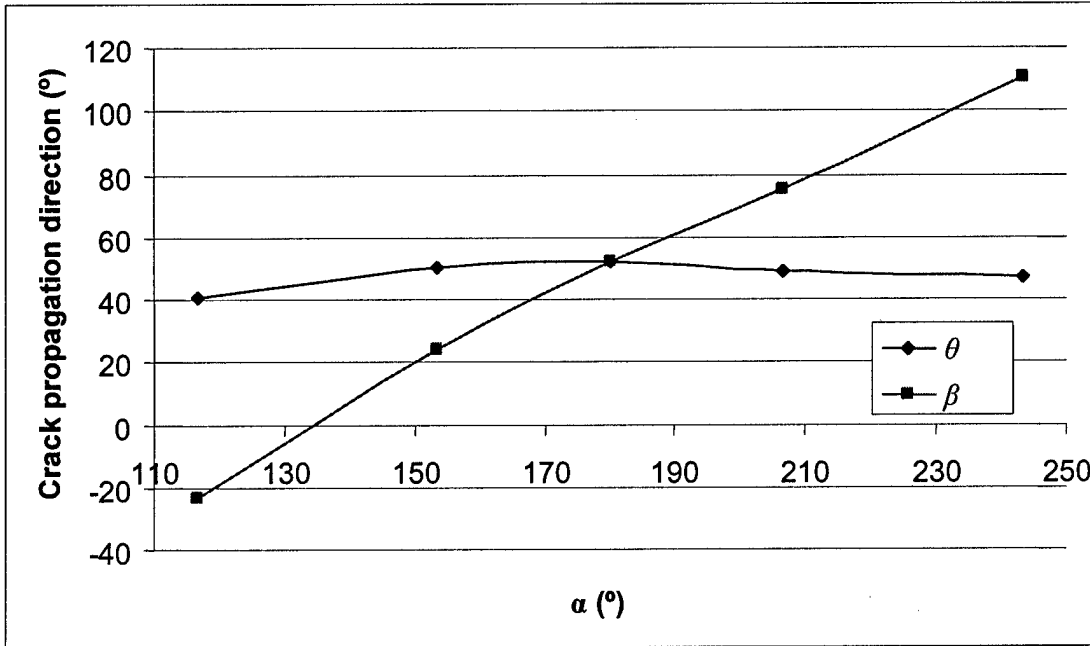


Figure 72. Crack propagation direction sensitivity to the initial internal crack direction.

From Figures 70 – 72 we can conclude that:

- (1) The energy release rate is highly sensitive to the direction of the initial crack for internal cracks in single-strap joints. It reaches its maximum value when α is around 180° (horizontal crack). Under the same loading, the energy release rate is much higher for the internal crack than for the external crack (up to $10^2 - 10^3$ times higher, see Figure 60).
- (2) The stress intensity factors (K_I and K_{II}) are about the same magnitude, and approximately 10 to 100 times greater than for the external crack (Figure 61). So the effects of both Mode I and Mode II are important in this case. They also both reach the maximums when α is around 180° . It seems the horizontal crack can result a higher stress concentration than other cracks, but we don't know the reason yet.
- (3) The crack propagation direction θ is in the region of 40° to 50° . In most cases, β is bigger than 0° , so most internal cracks tend to propagate to the top adhesive/adherend interface.

B. Effects of initial crack lengths and positions

The model to simulate internal parallel crack is given in Figure 73. In Figure 73, a is the crack length, h is the crack position to the adhesive layer centerline, and σ is the displacement load. In this model, the initial crack is always parallel to the adhesive/adherend interface, but its length a and position h vary. The dimensions are as follows: $L = 120$ mm, $L_o = 20$ mm, $t_1 = t_2 = 3$ mm, and $t_3 = 0.2$ mm. The material properties of the adherends are $E = 70$ GPa, $\nu = 0.3$. The material properties of the adhesive layer are $E = 2.2$ GPa, $\nu = 0.4$.

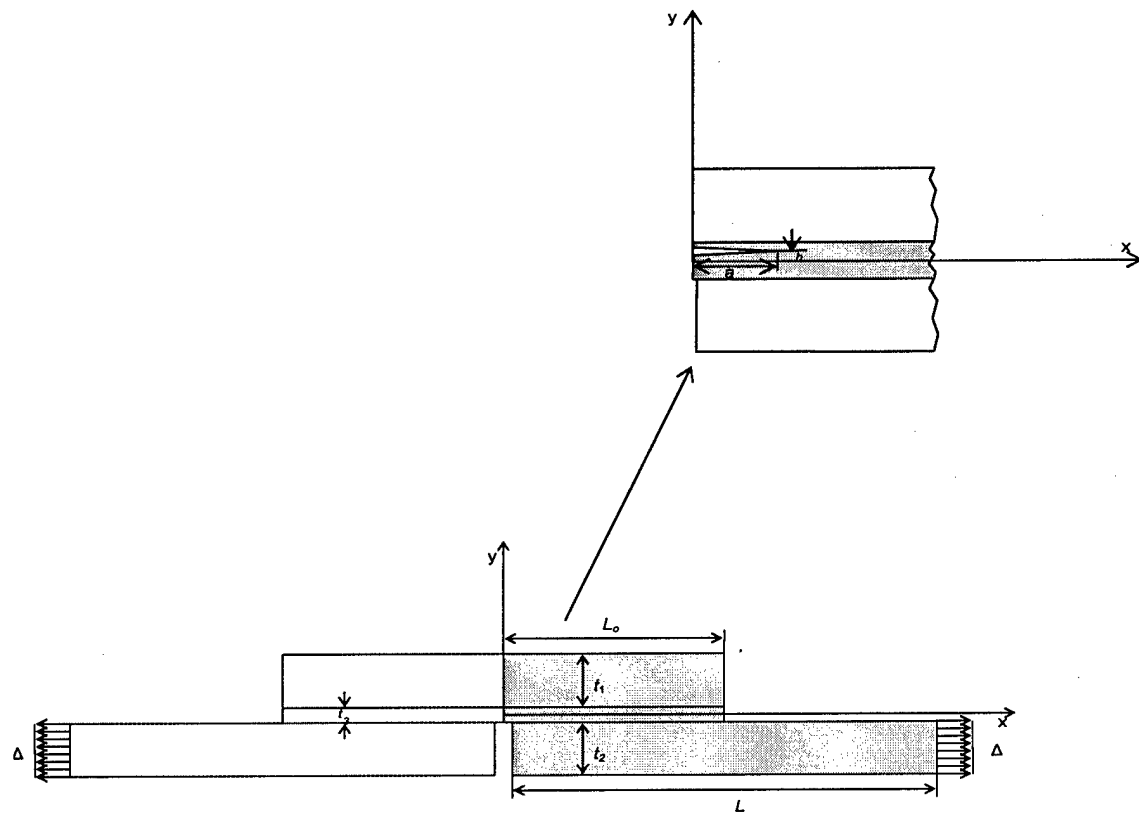


Figure 73. FEA model for study of internal initial crack length and position effects.

Figures 74-77 show the energy release rate (G), the stress intensity factors (K_I and K_{II}), and the crack propagation direction (θ) are functions of initial crack direction (α).

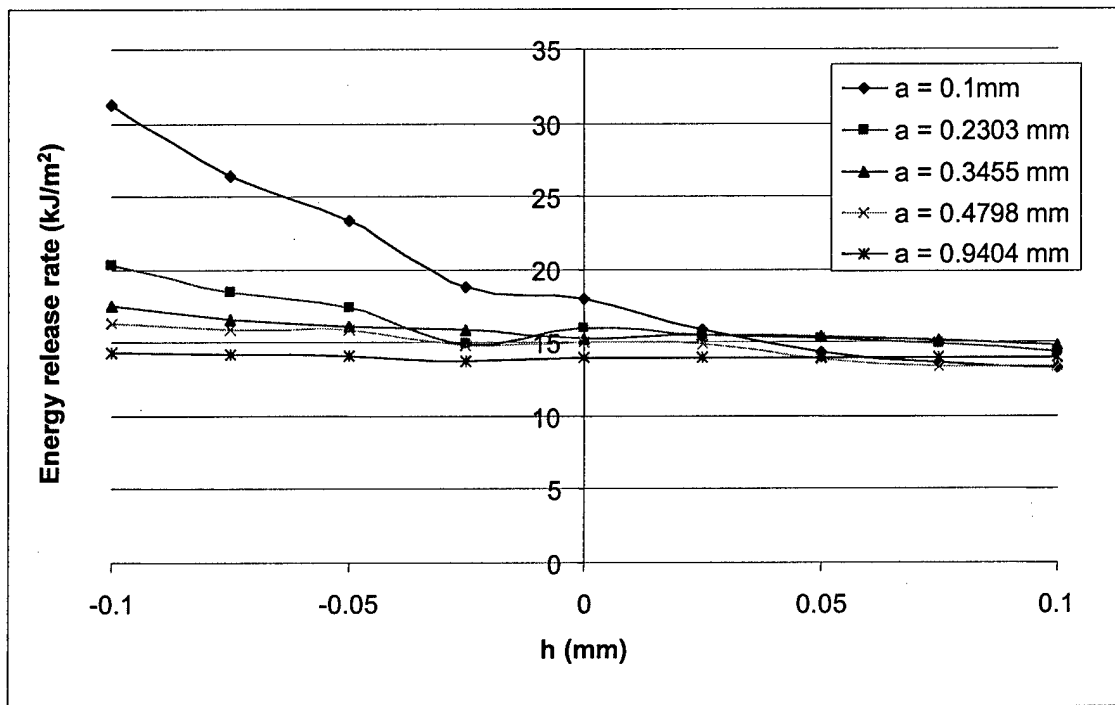


Figure 74. Energy release rate sensitivity of internal crack length and position.

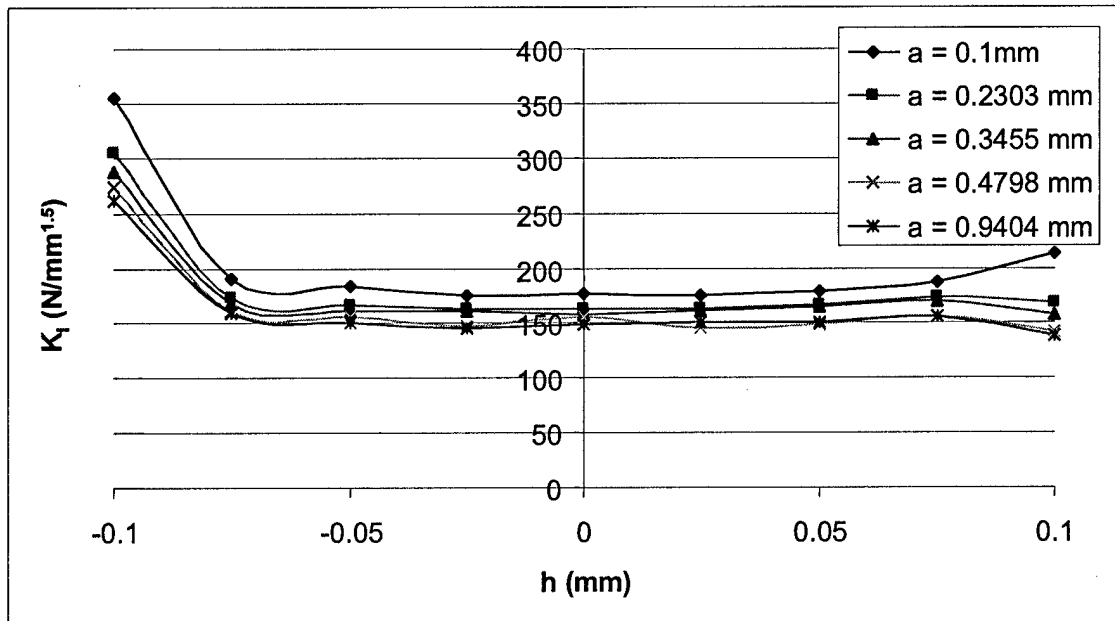
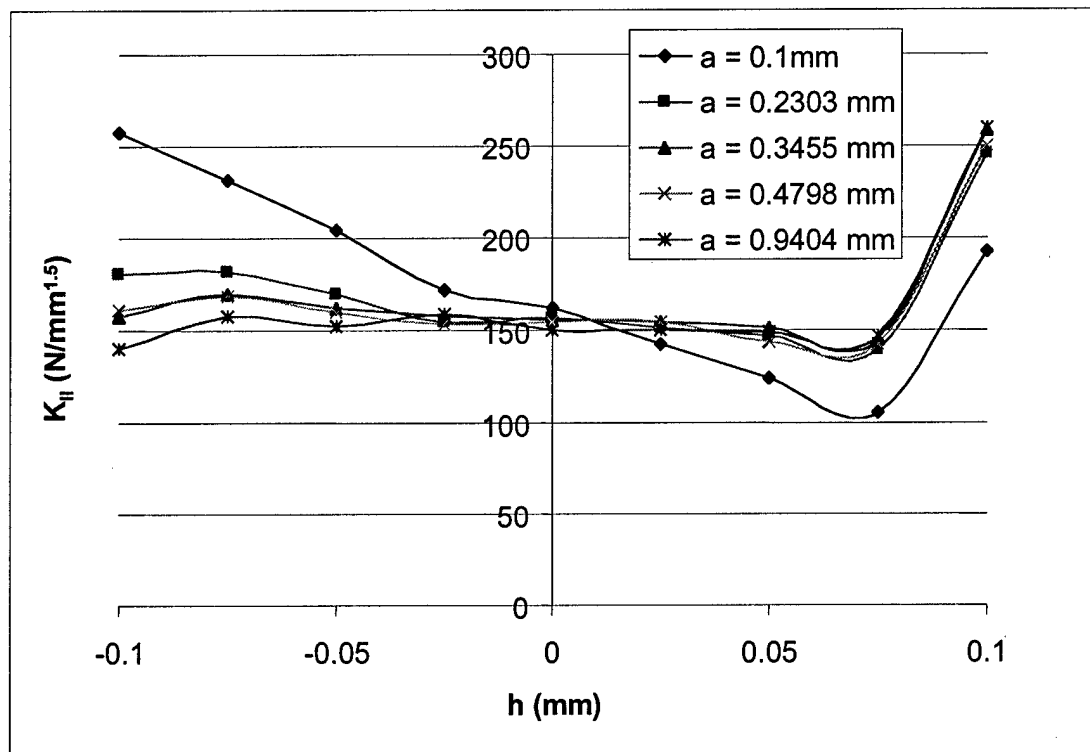
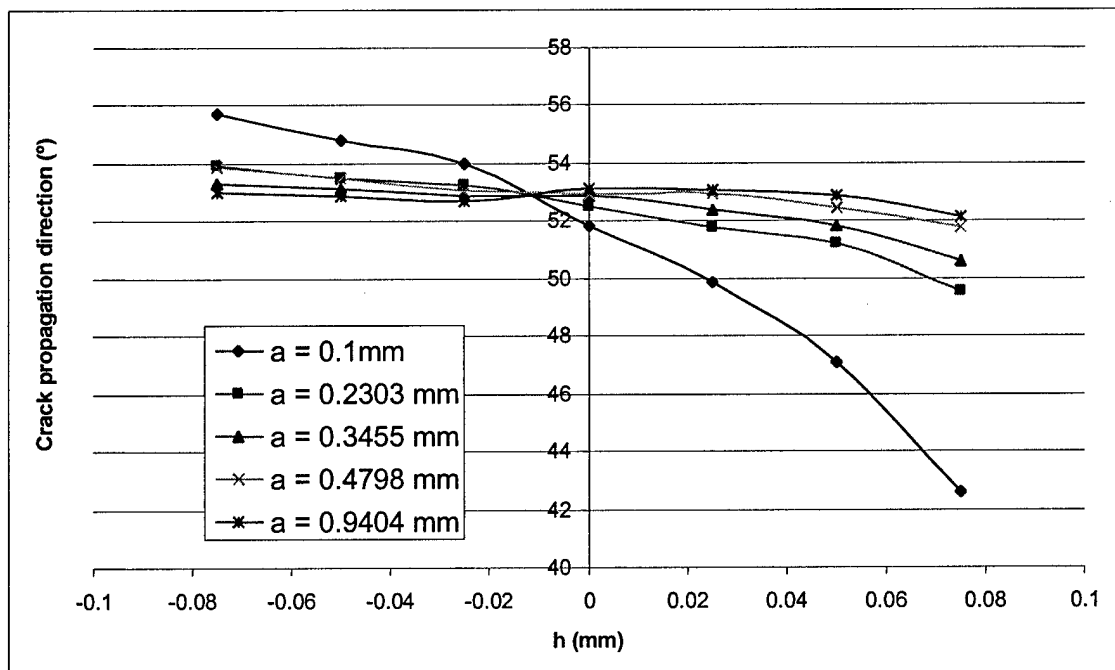


Figure 75. K_I sensitivity of internal crack length and position.

Figure 76. K_{II} sensitivity of internal crack length and position.Figure 77. Crack propagation direction θ sensitivity of internal crack length and position.

From Figures 74 – 77, we can conclude that:

- (1) For most crack positions h , short cracks give a higher energy release rate. The energy release rate decreases rapidly with increasing of the crack length. It tends to be a constant value when the crack length a is larger than 0.5 mm. Equations (28 and 29) show that the energy release rate usually increases with the crack length, but for a single strap adhesive joint, if the crack is located in the center of the joint, it is special. The reason is a single strap adhesive joint itself, without any initial crack, has significant stress concentration in the center (Figures 34 – 36). When the crack is shorter, its crack tip is closer to the central stress concentration region.
- (2) When the crack is located on the bottom adhesive/adherend interface ($h = -0.1$ mm), the energy release rate is highest for short crack length. There are two kinds of stress concentration here: interface stress concentration and structure stress concentration. Interface stress concentration is the stress concentration resulted from the different materials. When materials with different moduli subject to the same load, they have different deformation, so that stress concentration would occur on their interfaces. Structure stress concentration is the results of structure form. Crack is a typical structure of stress concentration.
- (3) The maximum values of the stress intensity factors (K_I and K_{II}) are achieved at both adhesive/adherend interfaces, which is reasonable because the stress intensity is most serious on the interface. K_I always reduces with increasing of the crack length. K_{II} reduces with the crack length when h is bigger than -0.01 mm, and increases with the crack length when h is less than -0.01 mm.
- (4) The crack propagation direction is in the range of 42° - 56° . For short cracks, the crack propagation direction is relatively sensitive to the crack position h . The crack propagation direction is determined by the maximum principle stress direction at the crack tip. The detailed

stress distribution around the crack tip is complex for a single strap joint. It is difficult to explain it physically. This result is constant with our everyday life experience: when a piece of paper is pulled to the right horizontally from the bottom side, the left crack would propagate to the right and upward.

Both of the stress intensity factors (K_I and K_{II}) are significantly increased with the crack at the adherend/adhesive interface ($h = \pm 0.1$ mm). This means the stress concentration is significant on the interface. K_I and K_{II} generally decrease with increase of h , except the interface positions (Figures 75 and 76). It is reasonable. The larger is h , the farther away the crack is from the bottom adherend, where is the loading come from. When the crack length a increases, in most location, K_I tends to decrease but K_{II} tends to increase (Figures 75 and 76). It means peeling effects are significant for short cracks, and shear effects are significant for long cracks. The K_{II} curve of $a = 0.1$ mm (Figure 76) is different from other K_{II} curves. We guess the reason is the crack is too close to the center stress concentration region, which significantly changed the stress distribution around the crack tip for a short crack. Some irregular data distributions are found when their values are close. This is believed to be numerical errors. The curves of energy release rate keep decreasing with the increase of h in Figure 74. It is different from external parallel cracks, which usually have a maximum value close to $h = 0$ (Figure 64). This is because for the center parallel cracks, the stress concentration is significant when the crack lies on the bottom interface. Although the energy release rate is a function of both stress and strain, and the high modulus aluminum adherends restrict the deformation of adhesive, the energy release rate still approach to its maximum at $h = -0.1$ mm (on the bottom interface).

5.5 CONCLUSION

Chapter 5 focuses on finite element analysis of fracture mechanics for single-strap adhesive joints. We discussed 3 problems: (1) mesh density requirement of a rectangular bar and single-strap adhesive joints; (2) singularity problem for single-strap adhesive joints, and (3) effects of initial crack direction, length, and position in single-strap adhesive joints (for both external and internal cracks). The major conclusions that can be drawn from Chapter 5 are:

1. The mesh density required for FEA fracture mechanics study of single strap adhesive joints is such that b/a is less than 0.06. Under this mesh density, the error of energy release rate for rectangular samples is 1.5%, and the error of stress intensity factor K_I is 3%. For single-strap adhesive sample, results show that further increase of the mesh density does not significantly change the results of energy release rate G , stress intensity factors K_I, K_{II} , and the crack propagation direction θ .
2. There are two kinds of singularity problems in single-strap adhesive joints: free edge singularity problem and central singularity problem. The latter is more serious. It shows the stress concentration is more significant in the center of a single-strap adhesive joint. So failure of this kind of adhesive joint usually begins from its center.
3. For both external crack and internal crack, the energy release rate and the stress intensity factors, K_I and K_{II} decrease with an increase in the crack length.
4. Stress intensity factors, K_I and K_{II} are useful in comparing structures (or locations) with different modulus, because stress intensity factors are functions of stress distributions, independent from material modulus. This is the reason that the results of stress intensity factors showed the stress concentration effects on the interface, but the results from the energy release rate did not reveal this important phenomenon.

5. For single-strap adhesive joint, the most possible starting location of joint failure is at the center of the bottom adhesive/adherend interface.
6. Most internal cracks tend to propagate to the top adhesive/adherend interface, but most external crack tends to propagate to the bottom adhesive/adherend interface.

Chapter 5 discussed necessity (singularity phenomenon) and reliability of FEA fracture mechanics analysis for a single strap joint. The suitable mesh density used for FEA fracture mechanics analysis and design of a single strap joint was determined. From Chapter 5, we know that the most possible location of initial joint failure is at the enter of a single strap joint, on the bottom interface. The direction of initial crack has significant effects on the energy release rate and the stress intensity factors, but the effects on the crack propagate direction is more important. Because the crack propagation direction can determine the crack approach to the top interface or the bottom interface, and interface cracks are more common than the adhesive bulk cracks. The energy release rate (G) is an important design parameter in fracture mechanics, but it has a limitation: G is a function for not only stress, but also material modulus. So a lower energy release rate does not always mean lower stress concentration. The stress intensity factors are also important in adhesive joint design.

6 EFFECTS OF ADHESIVE/ADHEREND INTERFACE

This chapter focuses on the aluminum/epoxy interface effects on the global performance of aluminum adhesive joints. Three problems are discussed: nano-indentation tests for aluminum/epoxy interface, FT-IR analysis for aluminum/epoxy interface, and FEA fracture mechanics models including the interface effects. Nano-indentation tests were performed using an Interfacial Force Microscope (IFM). The test results show that the elastic modulus of epoxy changed gradually around the interface. FT-IR analysis shows that the modulus non-uniform distribution comes from non-uniform curing reaction of epoxy adhesive. Static finite element analysis (FEA) was carried out to determine the stress distribution in the adhesive layer of the single-strap adhesive joint, showing that there is a singularity problem in with these joints. In the fracture mechanics FEA, the gradually changing elastic modulus was included. The results show that the interface effects on the energy release rate and stress intensity factors of the whole aluminum adhesive joint are significant. It is thus necessary to take the interface effects into consideration in joint design.

6.1 NANO-INDENTATION TESTS FOR ADHESIVE JOINT SAMPLE

Nano-indentation tests were carried out by an Interfacial Force Microscope (IFM). A parabolic tungsten probe was employed.

A. Experiments

The adhesive used in our research is the FM 300-2 adhesive film, produced by Cytec Industries Inc. It is an epoxy-based film adhesive with the constituents shown in Table 2.

Table 2. Constituents of FM 300-2 film adhesive.

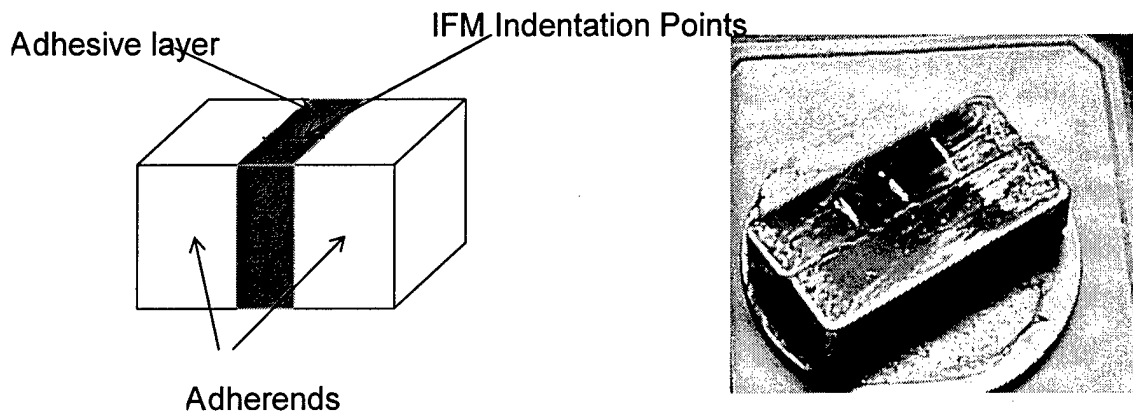
2 Butanone	Tetrabromobisphenol A
Epoxy Resins	Dicyandiamide
Diaminodiphenylsulfone	

The single-strap adhesive joint was comprised of a single layer adhesive film sandwiched between two aluminum adherends. The aluminum adherends (4.0 cm × 1.3 cm × 0.3 cm) required a surface preparation prior to adhesive application, which created an oxide layer that was stable under the conditions to which the adhesive bond was exposed [75]. Foreign substances such as dirt, grease, moisture, and original oxides present on the adherends' surfaces were removed by etching the surface with chemicals or placing an active oxide on the surface by anodizing [76]. Different surface treatments can be employed for aluminum; the Forest Product Laboratory (FPL) etch method [76, 77] was used in this project. Solvent cleaning with acetone (degreasing) was the preliminary step in the cleaning process, and was used to remove the oils and impurities present on the adherend surface. Then these adherends were treated with

Nochromix® (Godax Laboratories, Inc.) solution for about 30 minutes. This chemical treatment involves the creation of a new oxide layer on the surface of aluminum to improve its adhesion qualities. The adherends were taken out from the Nochromix® solution, washed thoroughly with tap water and dried. The metal adherends were not touched with bare hands after their surface treatment and were bonded soon after the cleaning [75]. The adhesive film was taken out from the refrigerator, cut to the required dimensions and was placed on one of the adherends, then the adherends were joined together. This joint was then placed on a Teflon sheet and this whole set up was placed in a mold. The mold was then placed in an oven at 120 °C for 90 minutes. The sample was allowed to cool down for few hours and later taken out from the oven and stored. A JEOL 840A scanning electron microscope (SEM) with a magnification power of 10X to 100,000X was used to measure the thickness of the adhesive layer in the bonded joint. The thickness was found to be approximately 130 µm.

The cured joint sample was cut into smaller pieces of required dimensions using a diamond-wafering blade (Beuhler, Inc., model No. 11-4239) mounted in a Model 11-1180 diamond saw (Buehler, Inc.). The diamond saw allows precise cutting of small samples. The cut sample was then polished manually, in order to reduce the surface irregularities caused due to the cutting. In this project, as distinct interphases were anticipated, polishing of the samples was required for analysis. The procedure for the polishing is discussed elsewhere [78]. This procedure has been proven to be successful for a variety of polymer/inorganic composite samples. The polished samples were then glued to metal discs (15 mm diameter) with the adhesive provided and were stored. The schematic of the final polished sample on which the chemical and mechanical

properties were tested is shown along with the digital image of the polished sample in Figures 78(a) and 78(b).



(a). Schematic of sample used for analysis. (b). Photo of polished sample

Figure 78. Polished sample for IFM nano-indentation.

The probes used in this study were formed by electrochemically etching 100 μ m tungsten wire. The tip of the probe was imaged using a scanning electron microscope (SEM) and the radius of the tip was determined (Figure 79). For the probe in Figure 79, the tip radius was approximately 400 nm.

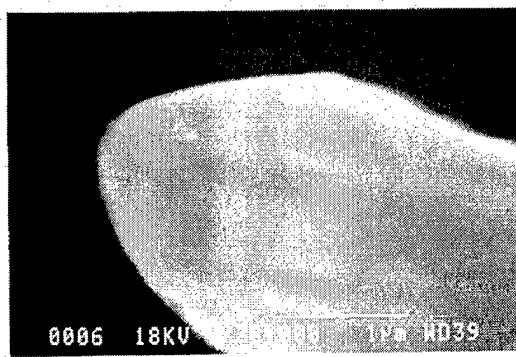


Figure 79. SEM image of an electrochemically etched tungsten probe.

Force profiles were performed under an increasing load up to a maximum of 10 μN with constant displacement rate of 1 angstrom per step. When the final load was reached, the probe backed out of the sample surface with a constant displacement rate. The loading curve was fit to a Hertzian contact model to determine the elastic modulus, which assumes the deformation of an elastic half space is caused by a rigid, non-interacting parabolic probe. A deviation from Hertzian response was indicative of plastic deformation. The deformation can be related to the depth of penetration by Equation (42):

$$P = \frac{4}{3} R^{0.5} E_r D^{1.5} \quad (42)$$

where P is the applied load, R is the radius of the probe tip, D is the depth of penetration, and E_r is the reduced modulus as defined by Equation (43):

$$\frac{1}{E_r} = \frac{1 - \nu^2}{E} + \frac{1 - \nu_i^2}{E_i} \quad (43)$$

B. Nano-Indentation Test Results and Discussion

Figure 80 shows the elastic modulus values obtained by applying Hertzian analysis to the force profiles taken on an adhesive bonded joint. Force profiles were taken starting from one interface to the other interface. A significant variation in the elastic modulus was observed within a 20 μm region next to the adherend. Beyond this region the modulus does not vary significantly. The contact area of probe and surface during the nano-indentation is in the range of 0.015 to 0.03 μm^2 , and the distance between two nano-indentation points is 2 μm . The size of the contact area

was such that the measured modulus was a local modulus at that particular position. At the same time, the maximum load is around 10 μN in the process of an IFM nano-indentation. The tiny indentation area and small indentation load greatly reduced the "fiber bias" effects, which mean the high modulus material restricts the deformation of low modulus material in a non-uniform structure.

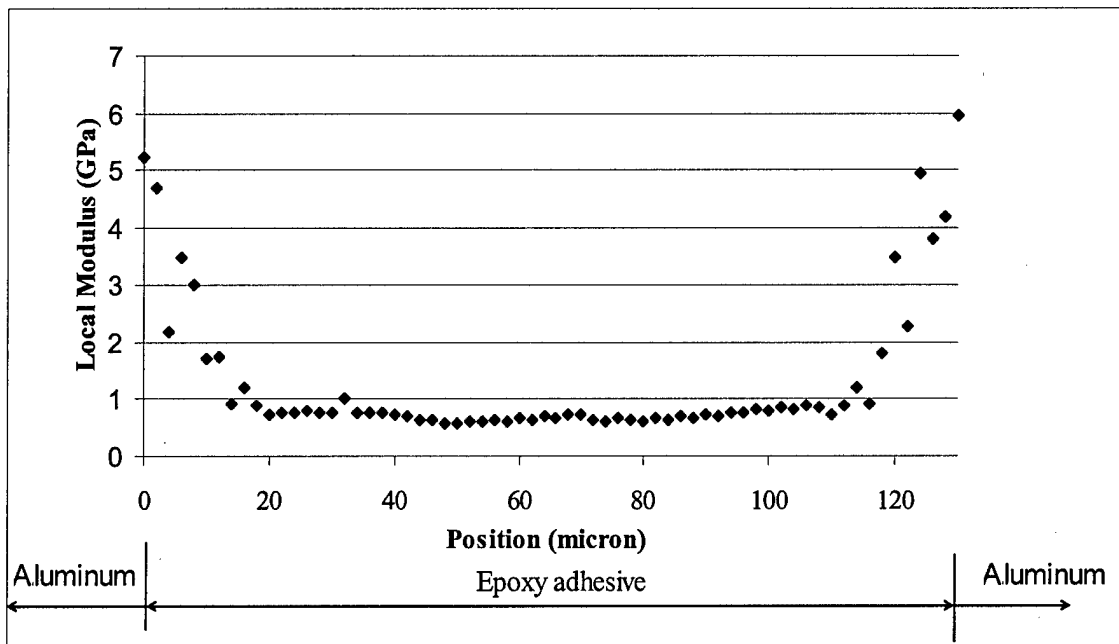


Figure 80. Local modulus across the adhesive layer in aluminum adhesive joint from IFM nano-indentation.

In the region near the epoxy/aluminum interface, the local modulus of the epoxy is obviously higher than that in the center of the adhesive layer. This effect is studied using Fourier Transform Infrared Spectroscopy (FT-IR). It is believed to be the results of variations in the cure chemistry. The interphase shows to be more fully cured and stiffer than the bulk region, with a higher modulus, and this is discussed in the next section. The scattering of modulus values

within the interphase may be due to the roughness of the surface or due to localized curing in the region. Wingard and Beatty stated that changes of ~5% in the stoichiometry ratio of epoxy/amine end groups have a strong influence on mechanical properties [79].

6.2 FT-IR ANALYSIS FOR ALUMINUM/EPOXY ADHESIVE JOINTS

FT-IR analysis was carried to interpret the phenomenon of non-uniform modulus distribution close to the aluminum/epoxy interface. The samples used in this section was cured under a gradient temperature, the details of the curing conditions are shown in Figure 81.

A. Preparation of Temperature Gradient Cured Samples

The schematic of the experimental setup for preparing the temperature gradient sample is shown in Figure 81(a). Figure 81(b) shows the sample with hotplate on one side and the cooling water pipe on the other side. The purpose of preparing this sample was to create a difference in the cure chemistry of the adhesive within the sample and to contrast the results to an adhesive bonded joint where temperature is approximately uniform throughout the sample. In order to achieve this gradient, one adherend was maintained at a higher temperature and other adherend at lower temperature. This was achieved by running water at lower temperature, continuously through a conduit placed on the upper adherend. The adherends were treated in the same way as described in section 6.1-A. As seen in the schematic (Figure 81(a)), the sample was placed on the hotplate. The hotplate temperature is regulated with a controller. A thermocouple (T_c) connected to the controller was placed on the hotplate. Water at 20°C flew in an aluminum square conduit continuously. Two layers of the adhesive were kept between the adherends to ensure proper temperature gradient between the two interphases of the joint sample. The thickness of the

adhesive layer in this sample was $\sim 300 \mu\text{m}$. A heat transfer calculation was performed prior to the experiment and showed that there would be a temperature gradient; the difference was calculated to be $\sim 45^\circ\text{C}$ between the two interphases (represented by T₁ and T₂ in Figure 81(b)).

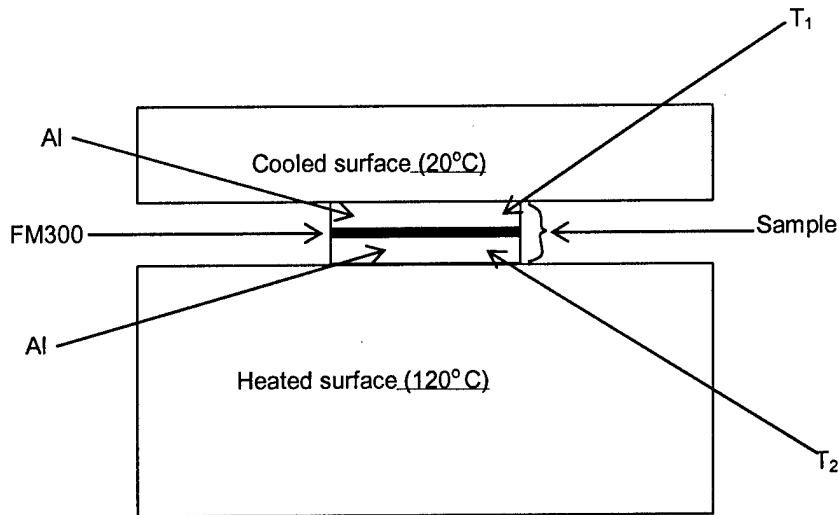


Figure 81 (a). Schematic of the experimental setup for temperature gradient sample.

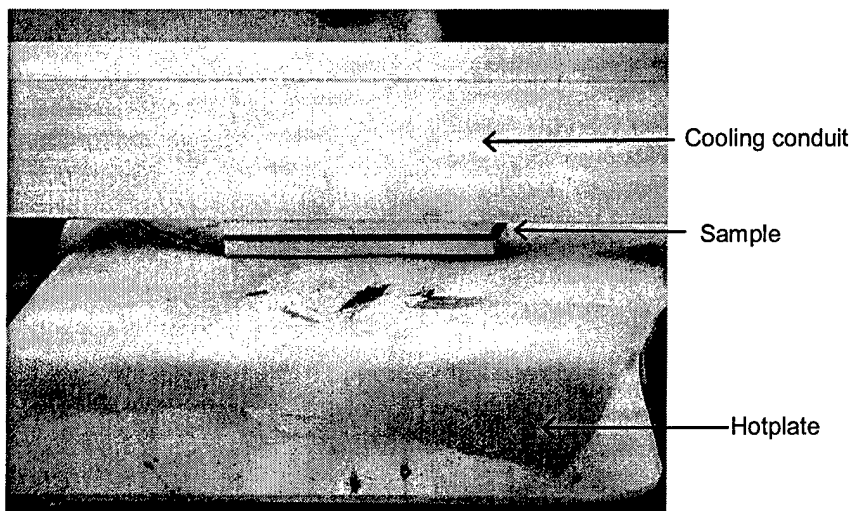


Figure 81 (b). Digital image of the experimental setup for temperature gradient sample.

B. FT-IR Microspectroscopy Results

(1). Baseline calculations

The typical spectra shown in Figures 82(a) and 82(b) of the as-received adhesive (the adhesive film as stored in the refrigerator) and the cured adhesive are used to determine the baseline distribution of the significant peaks and their relative concentrations. The noise level in the spectra is observed to be ~ 0.01 absorbance units. Therefore, the absorbance peak due to the epoxy moiety observed at 845cm^{-1} can be considered for analysis. This is much more confirmed with the peak observed at 845cm^{-1} in Figure 82(b). The reaction between epoxy and dicyandiamide present in the adhesive film is shown in Figure 83. This figure illustrates that the crosslinking reactions between the epoxy prepolymer and amine hardener generally involve the opening of the epoxide ring by reaction with amine hydrogens [80]. Hence, the epoxy concentration will decrease and this was considered the marker for the analysis.

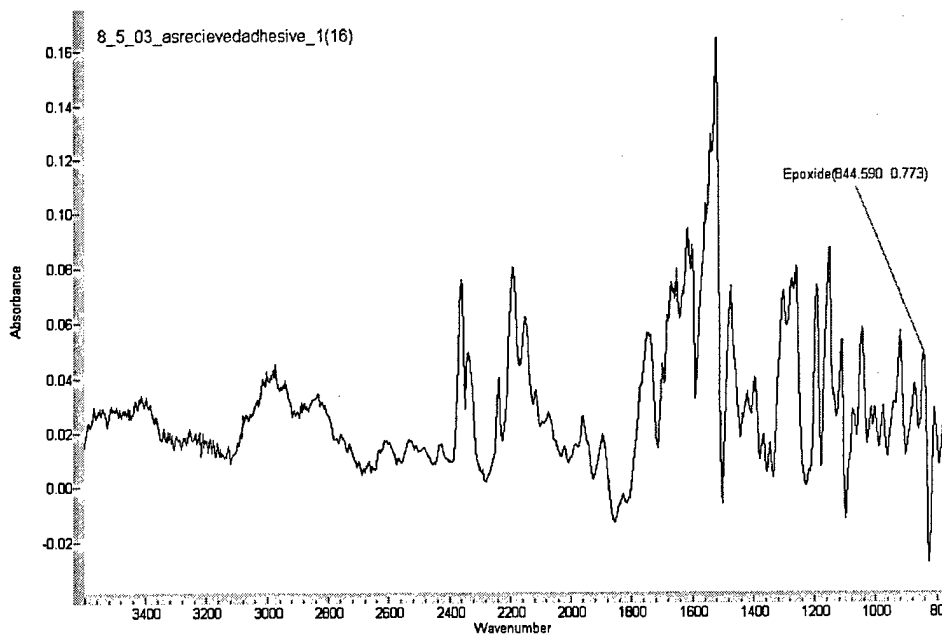


Figure 82 (a). Typical spectrum of as-received adhesive.

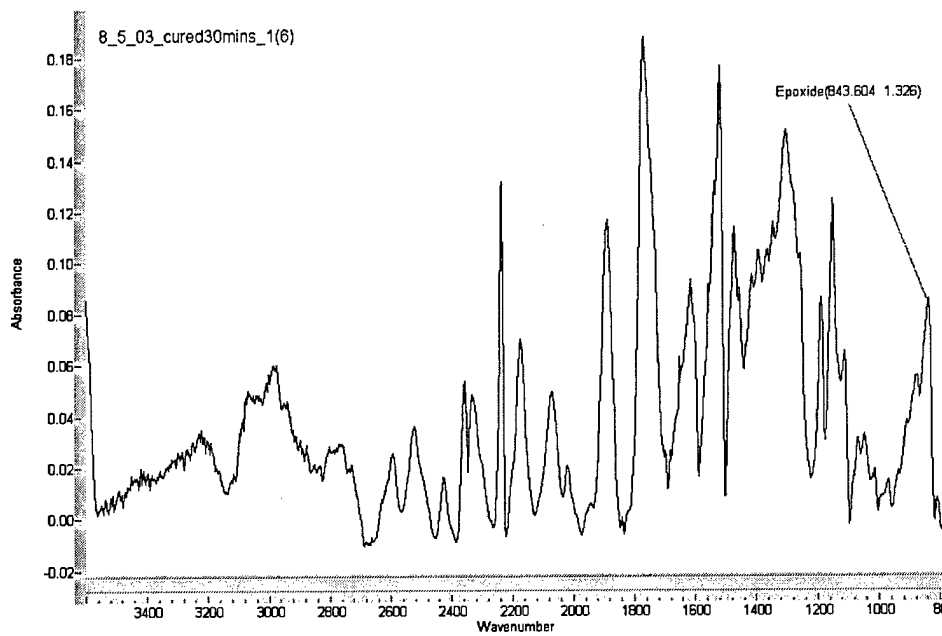


Figure 82 (b). Typical spectrum of cured adhesive.

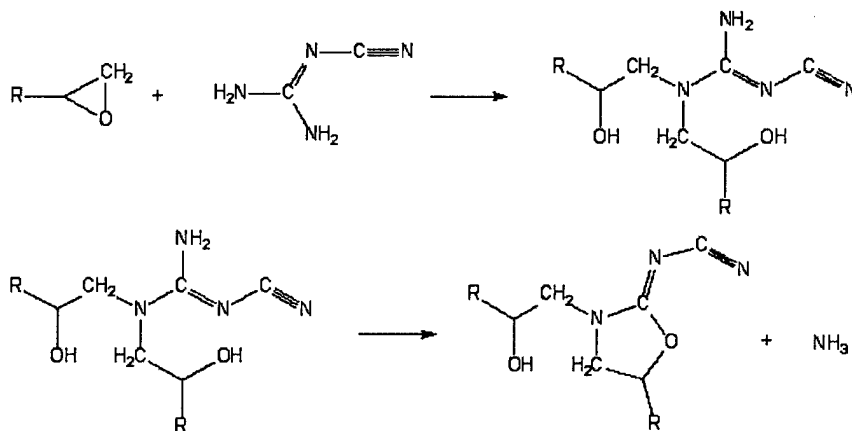


Figure 83. Reaction of epoxide with dicyandiamide.

Studies of epoxy amine cure systems have shown that there is either complete disappearance of epoxy absorbance band or there is a considerable decrease in the absorbance band of the epoxy in the system [⁸⁰⁻⁸⁴]. These studies also show that the epoxy-amine curing depends upon the stoichiometry of the system, the time allowed to cure and the cure temperature. In this baseline study, an attempt to study the epoxy-amine cure system present in the adhesive film, using infrared mapping is done. The epoxy in the reactants was considered here for the spectrum analysis; the concentration of epoxy should decrease as the reaction proceeds resulting in a decrease in the IR absorbance band at 845 cm⁻¹. When the reaction is complete, the epoxy concentration will be zero. Hence, the difference between the as-received and cured adhesive will be reflected in the decrease in absorption band or disappearance of the epoxy absorbance band. The relative concentration of the constituents of the adhesive in the selected area can be determined with infrared mapping. The contour diagrams obtained was representative of the concentration distributions of representative peaks (i.e., absorbance band profiles) in the sample over a selected area. The epoxy peak at 845 cm⁻¹ is considered for the analysis and its typical

distributions in the as-received adhesive, and cured adhesive are shown in the Figures 84 (a) and 84 (b). The contour picture describes that the concentration of epoxy is more in the as-received adhesive compared to the concentration of the epoxide in the cured adhesive. The numbers below the color bar represents the absorbance units which are directly related to concentration through the Lambert-Beer law. Both the profiles are plotted on the same scale. The color of the profile in the entire selected area is uniform representing that the concentration of the functional group in that selected area is uniform and this can be expected in a pure adhesive film.

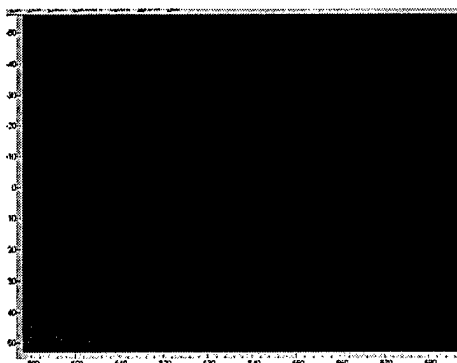


Figure 84 (a). Absorbance profile of the epoxy at 845cm^{-1} in the uncured adhesive.

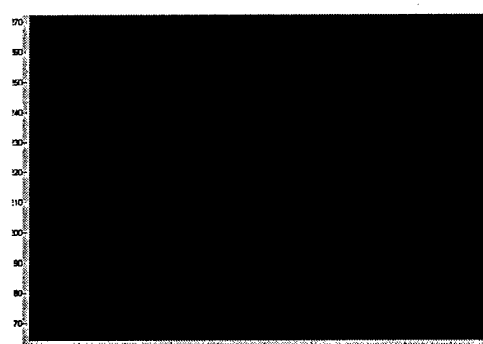


Figure 84 (b). Absorbance profile of the epoxy at 845cm^{-1} in cured adhesive.

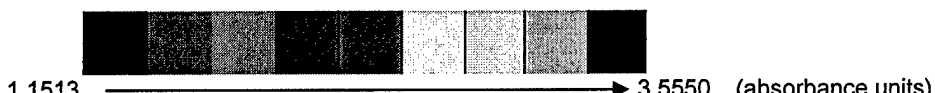
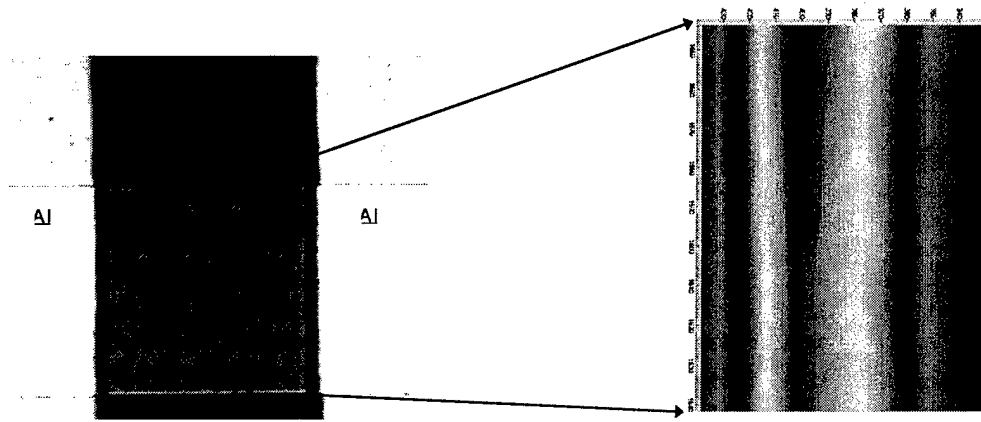


Figure 84. Comparison of absorbance profile of the epoxy at 845 cm^{-1} in the FM300 film adhesive (before and after curing).

(2). Results on temperature gradient cured sample

A temperature gradient sample was created to corroborate the FTIR absorbance profile. The same procedure for the IR microscopy was followed with the same parameters. All the contour

diagrams are plotted on the same scale. The epoxy concentration is observed to be increasing from higher temperature adhesive-adherend interface to lower temperature adhesive-adherend interface as shown in Figure 85 and 86. This figure confirms that the degree of curing results in a detectable difference in the interphase chemistry of the adhesive-adherend system. Hence in this case, since the temperatures at the interphases are different, different interphase chemistry is observed.



(a). Area selected on aluminum bonded joint for IR analysis.

(b). Absorbance profile of epoxy at 845 cm⁻¹. The adhesive film thickness was found to be ~130 μm.

Figure 85. FT-IR detecting points and the combined absorbance profile in the temperature gradient sample.

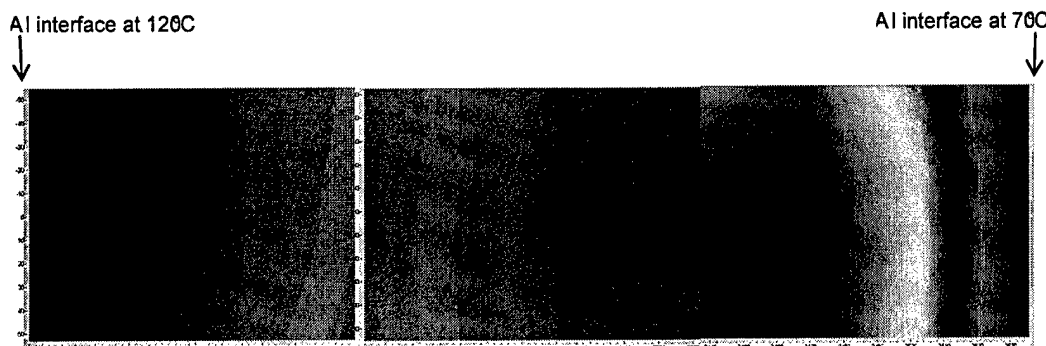
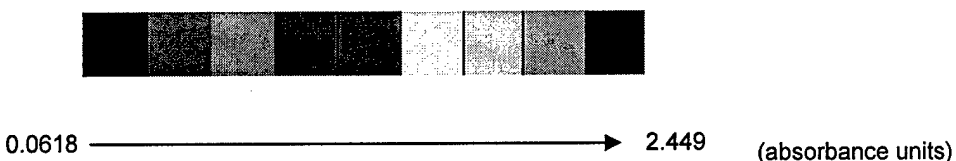


Figure 86. Absorbance profile of epoxy at 845cm^{-1} in temperature gradient sample. The adhesive film thickness was measured approximately $\sim 300 \mu\text{m}$.



(3) IFM Results for Temperature Gradient Cured samples

Figure 87 shows the elastic modulus values obtained by applying Hertzian analysis to the force profiles taken on adhesive bonded joint. Force profiles are taken starting from one interface to the other interface; only half of a typical modulus profile is shown. A significant variation in the elastic modulus was observed within a $20\mu\text{m}$ region next to the adherend. Beyond this region the modulus does not vary significantly, which indicates the bulk epoxy. The scattering of modulus values within the interphase may be due to the roughness of the surface or due to localized curing in the region.

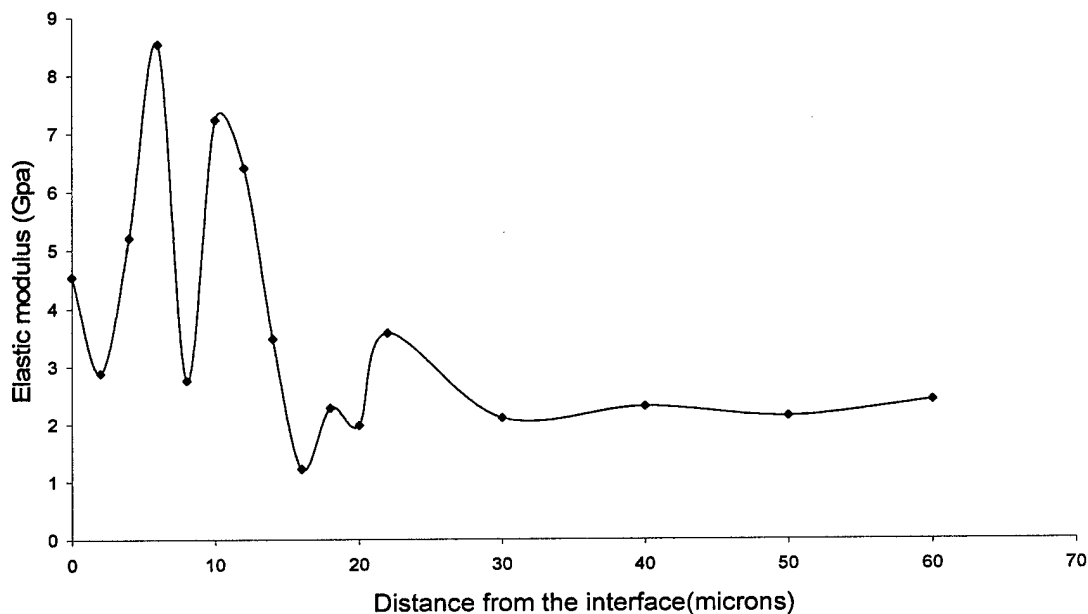


Figure 87. Elastic modulus vs. distance from the adherend which was maintained at 120 °C in the temperature gradient specimen.

(4) Relating elastic modulus to cure chemistry

Epoxy resins have the ability to react via the epoxy end-groups to generate three dimensional networks providing the final material with rigidity, hardness and the inability to reflow. This process of forming a crosslinked / 3-D network occurs during the curing process. The degree of cure of the adhesive in the bonded joints is related to the rigidity of the adhesive in the bonded joint, defined by the modulus. Stiff materials have a higher modulus; flexible materials have a lower modulus. The more crosslinks, the stiffer the material becomes and vice versa. If more crosslinks are formed, the concentration of epoxy would be less as more of the epoxy end groups are consumed in the reaction and vice versa. Crosslink density is one of the parameters used to define the crosslinks formed. It can be defined as the "number of moles of elastically effective

network chains per cubic centimeter of sample”^[86]. Hence, the stiffer the material is or the more crosslinks there are, the higher is the crosslink density. This crosslink density can be related to the elastic modulus by Equation (44) (valid in the rubbery plateau region),

$$\nu_e = \frac{E'}{3RT} \quad (44)$$

where ν_e is the crosslink density (mol/cm³), E' is the storage modulus (dyne/cm²), R is the universal gas constant (cm³atm g-mol⁻¹K⁻¹), and T is the temperature in K. The storage modulus can be approximated by the tensile elastic modulus for temperatures that differ significantly from T_g ^[85]. As a first approximation, we used Equation (42) to determine the relation between cure chemistry and elastic modulus. Figure 88 shows the plot of elastic modulus and crosslink density variation along the adhesive layer in the bonded joints. The elastic modulus profile is obtained from the IFM data and the crosslink density is calculated accordingly from Equation (41). As seen from Figure 88, the elastic modulus and the crosslink density vary in the same manner, and, the adhesive is stiffer within the interphase compared to the bulk. The absorption profile of the epoxy functional group is placed on Figure 88 to relate the modulus to cure chemistry. It is clearly seen that the adhesive is cured more (less concentration) at the interphases rather than the bulk; corresponding to an increase in crosslink density.

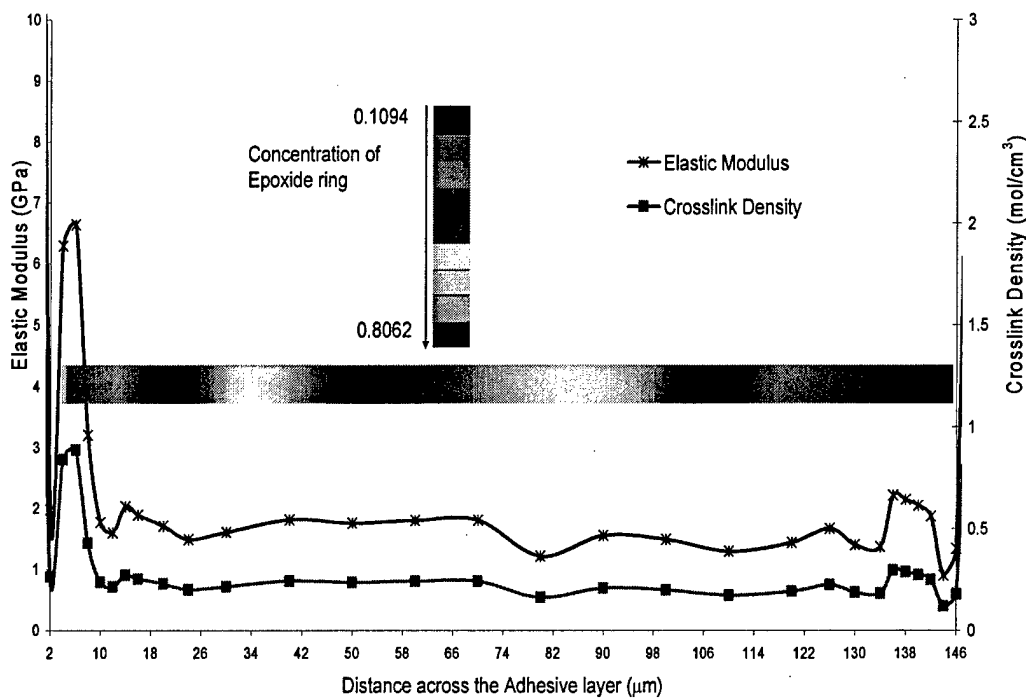


Figure 88. Variation of the properties along the adhesive layer in bonded joint.

It has been showed that there are observable variations in the cure chemistry and the elastic modulus of the adhesive film in the adhesively bonded joints. The interphase properties are shown more fully cured and stiffer than the bulk. The approximation crosslink density is related to observed cure chemistry through the measured elastic modulus.

6.3 FEA ANALYSIS INCLUDING INTERFACE PROPERTIES

A. Step Representation of Elastic Modulus Distribution across Adhesive Layer

In order to make the data in Figure 80 suitable for FEA modeling, the elastic modulus of the adhesive layer was in a stepwise fashion (Figure 89).

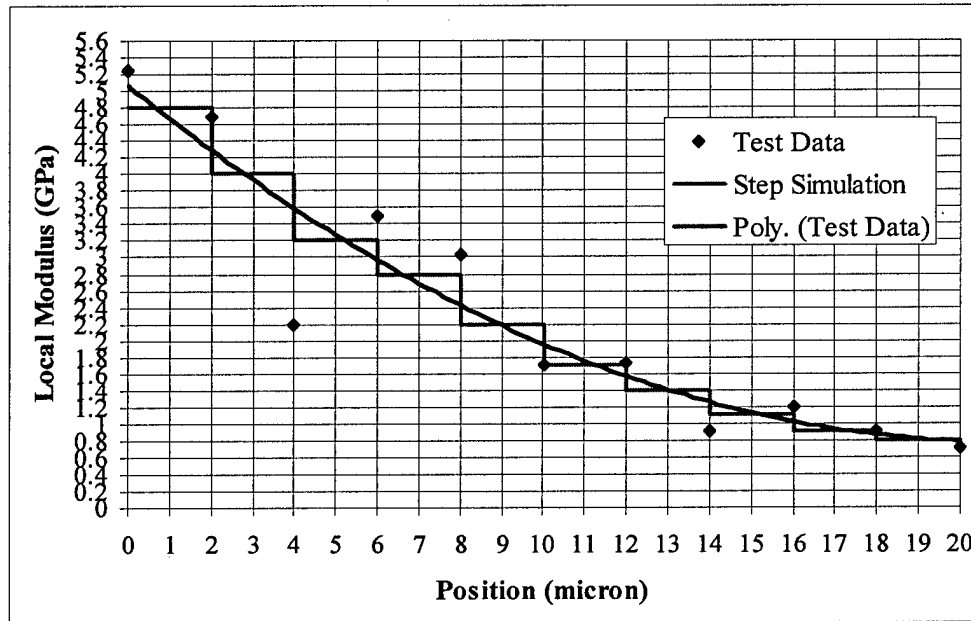


Figure 89. IFM nano-indentation data on interfacial region and its step representation. Data shown is for the first 20 μm of Figure 80.

B. FEA Modeling for External Parallel Crack

In this section, the crack was located on the outer edge of the single-strap adhesive joint ($x = 20$ mm), propagating parallel to the adhesive/adherend interface. The FEA model used in simulating the external parallel crack propagation in the adhesive joint sample is shown in Figure 53. In this model, a is the crack length, h is the crack position to the adhesive layer central line, and Δ is the displacement load. For this model, $a = 0.1$ mm, $\Delta = 0.5$ mm, and h varies. The material properties of adherends are $E = 70$ GPa, $\nu = 0.3$. The material properties of the adhesive layer are given as (1) Uniform model: $E = 0.7$ GPa, $\nu = 0.4$; (2) Non-uniform model: E is distributed as shown in Figure 89 (symmetric according to the centerline of the adhesive layer), $\nu = 0.4$. The FEA results of energy release rate are given in Figure 90.

In Figure 90, the crack position (h) changes from the bottom interface to the top interface. The energy release rates are calculated at different locations for both models. In most locations, the Non-uniform model gives a higher energy release rate. At the interfaces, the energy release rates from two models are similar.

Comparing the results shown in Figure 90, the interface effects are significant, and should be taken into consideration in adhesive joint design. For example, if the crack is located in the center of the adhesive layer, its energy release rate in the non-uniform model is 37% higher than the results in the uniform model.

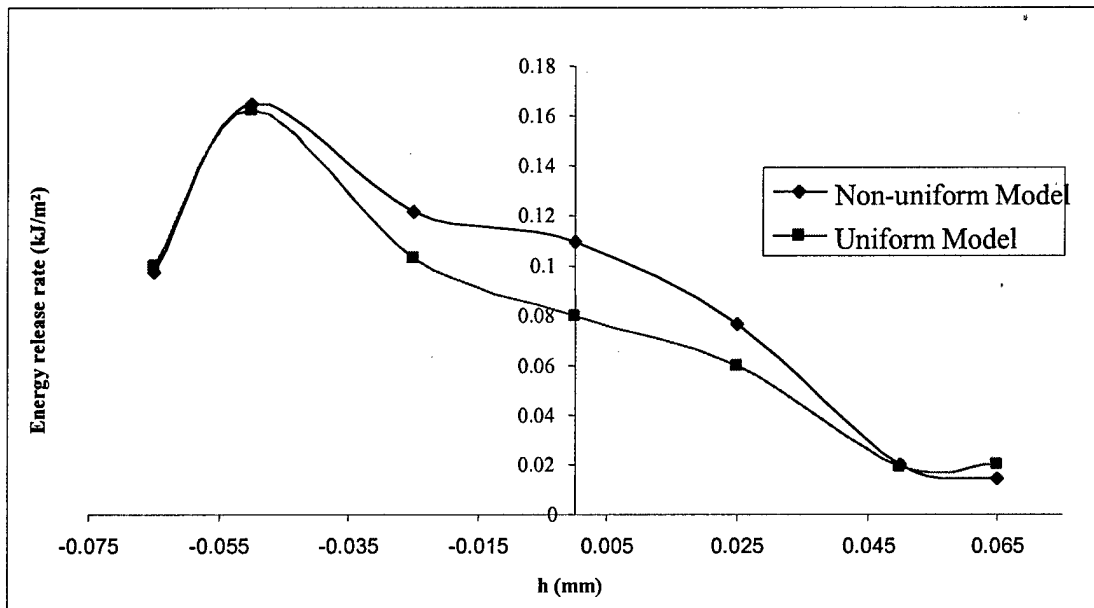


Figure 90. Crack position sensitivity of energy release rate.

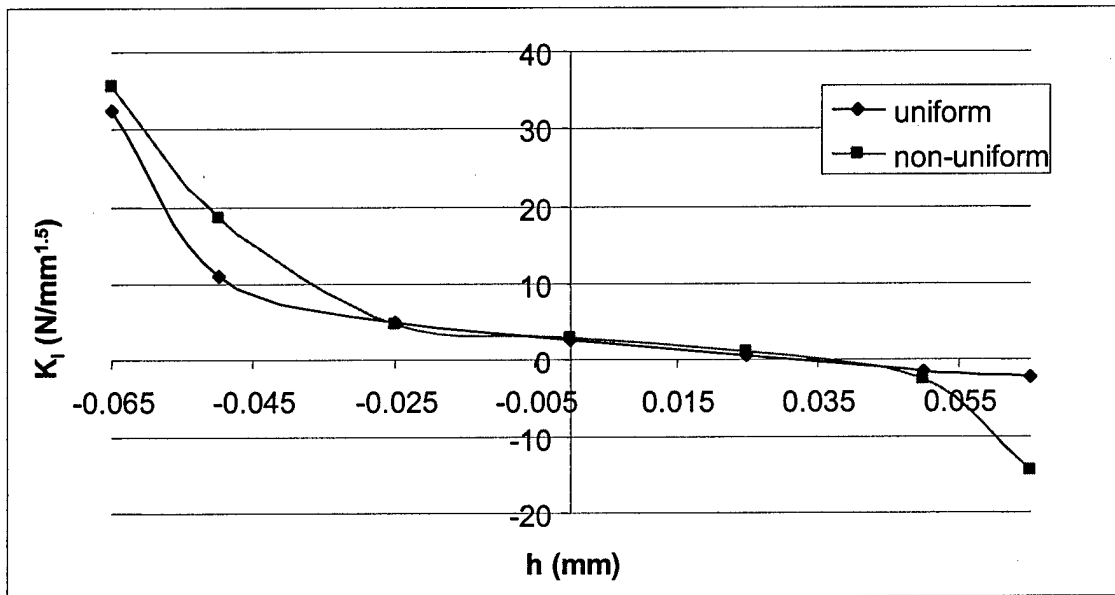
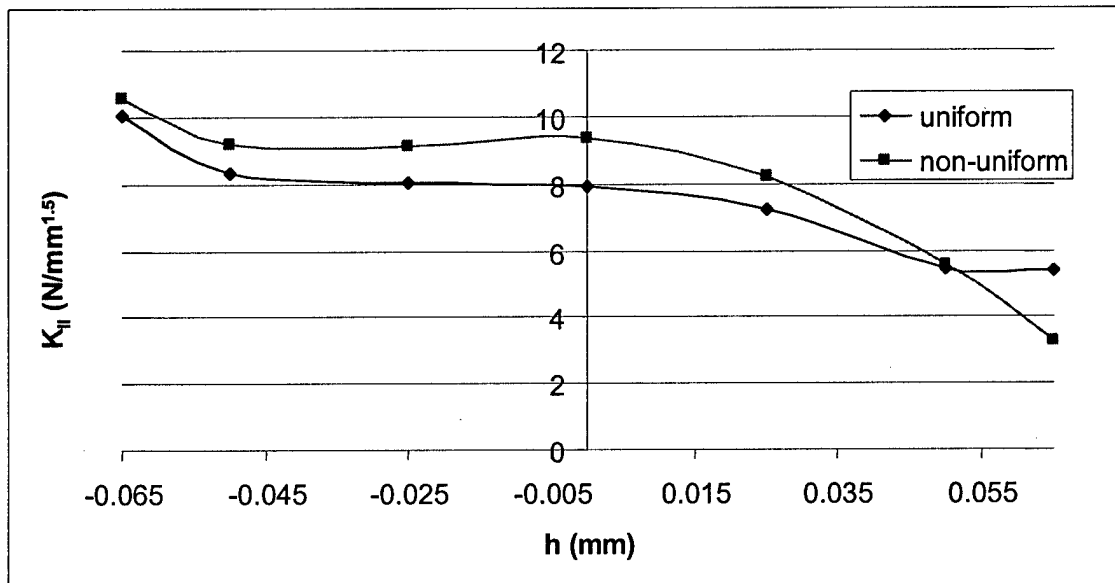
The physical meaning of energy release rate is the energy applied on a unit area of material under a given loading condition. It was determined by both stress and strain. So if two materials

have different modulus, the one with the lower modulus gives a higher energy release rate for the same stress. From this point of view, we think the stress intensity factors may be better design parameters in this case, because the modulus is changing with the location. Figures 91 - 92 give the results of stress intensity factors (K_I and K_{II} , where the subscripts "I" means "Mode I loading" and "II" means "Mode II loading").

Figures 91 - 92 show that:

- (1) When the single strap adhesive joint is pulled horizontally, the outer parallel crack is subject to a mix loading of Mode I and Mode II.
- (2) When the crack position $h/t > 0.25$ (where t is the thickness of the adhesive layer), $K_I < 0$, which means the crack is compressed. In this case the crack can propagate only under the effects of K_{II} .
- (3) When the interfacial adhesive modulus gradient was included, if the crack is located on the centerline of the adhesive layer, K_{II} is 25% higher than that from the uniform adhesive layer model; K_I from those two models are similar.

Both the results of energy release rate, G , and the results of stress intensity factors (K_I , and K_{II}) show that uniform adhesive model has non-conservative error in the design of aluminum single strap adhesive joints.

Figure 91. Crack position sensitivity of K_I Figure 92. Crack position sensitivity of K_{II}

C. FEA Modeling for Internal Parallel Crack

In this section, the location of the crack was analyzed at the center of the adhesive joint ($x = 0$).

We assume it propagates symmetrically with respect to the y axis (Figure 93). The stress

analysis shows that for single strap joints, the stress concentration is significant in the center of the joints (Figures 34 - 36). So it is very possible that the failure of single strap joints may begin from the joint center.

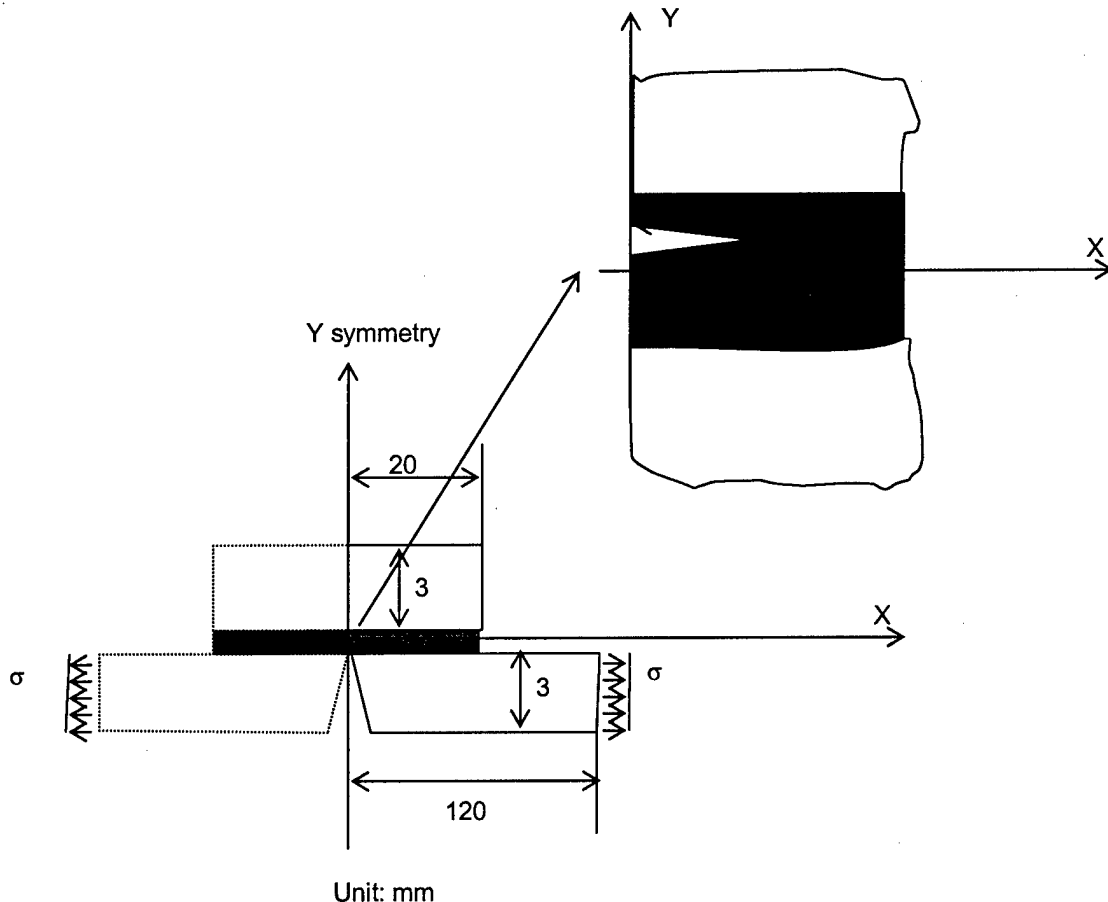


Figure 93 FEA model of an internal parallel crack (crack position: $x = 0$)

Figure 94 shows the effects of adhesive interfacial modulus gradient on the energy release rate of an internal crack (crack length $a = 0.1$ mm; crack location h is variable).

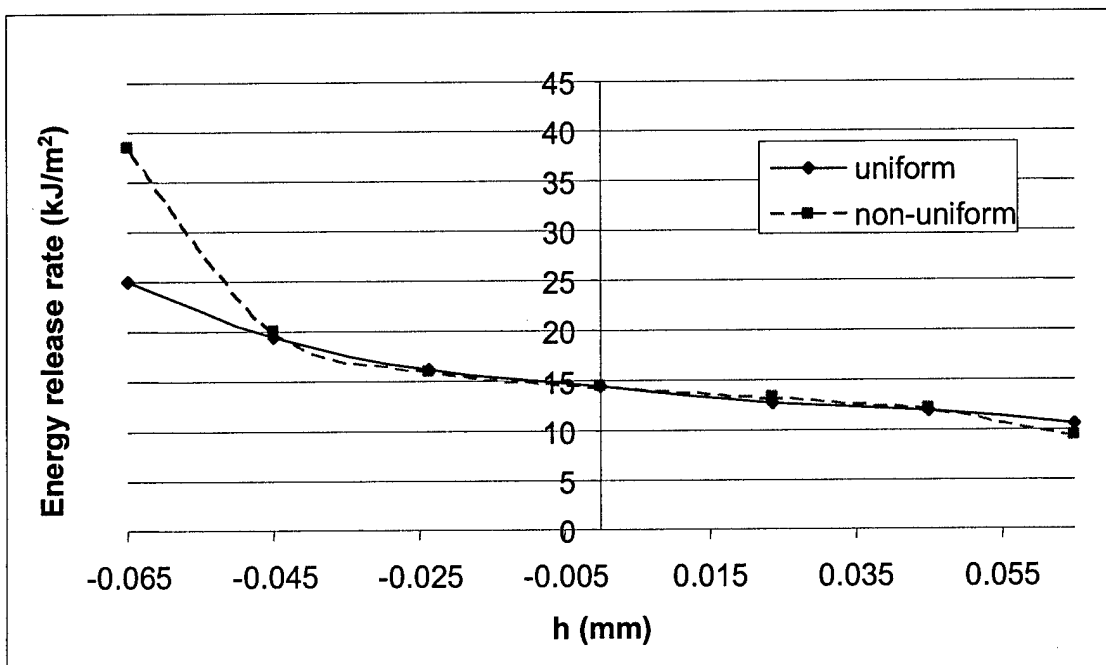


Figure 94. Crack position sensitivity on energy release rate for an internal crack (crack length $a = 0.1$ mm)

In Figure 94, non-uniform adhesive model gives a significantly higher energy release rate on the bottom interface of the adhesive layer ($h = -0.065$ mm). As the bottom interface is also the location of maximum energy release rate, this location should have a maximum chance to be the failure initiation point. At this same location, the uniform adhesive model gives 48% negative error in estimating the energy release rate.

Figures 95 - 96 show the effects of adhesive interfacial modulus gradient on the stress intensity factors of an internal T-shaped crack (crack length $a = 0.1$ mm).

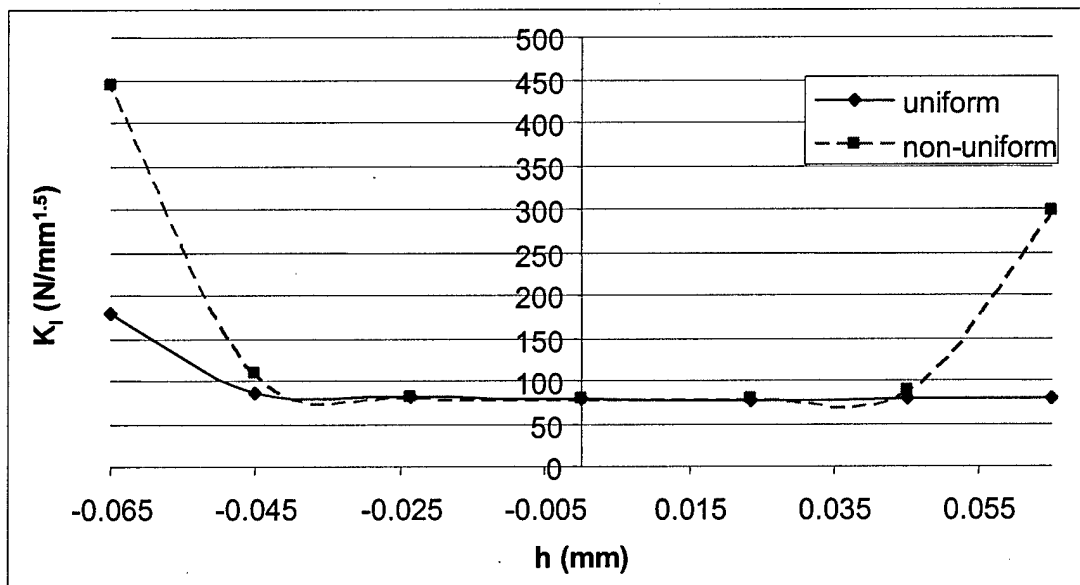


Figure 95. Crack position sensitivity on K_I for an internal T-shaped crack

(crack length $a = 0.1$ mm)

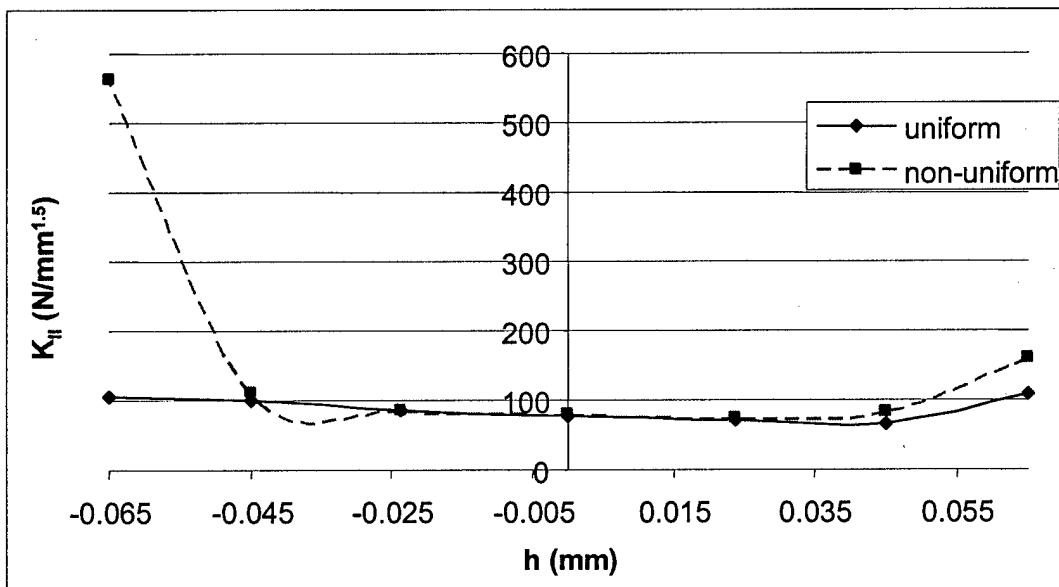


Figure 96. Crack position sensitivity on K_{II} for an internal T-shaped crack

(crack length $a = 0.1$ mm)

From Figures 95-96, we can see the uniform adhesive model greatly under-estimated the stress concentration on the two adhesive interfaces.

We also simulated the effects of the crack length of an internal parallel crack. Figure 97 gives the energy release rate results for different crack length.

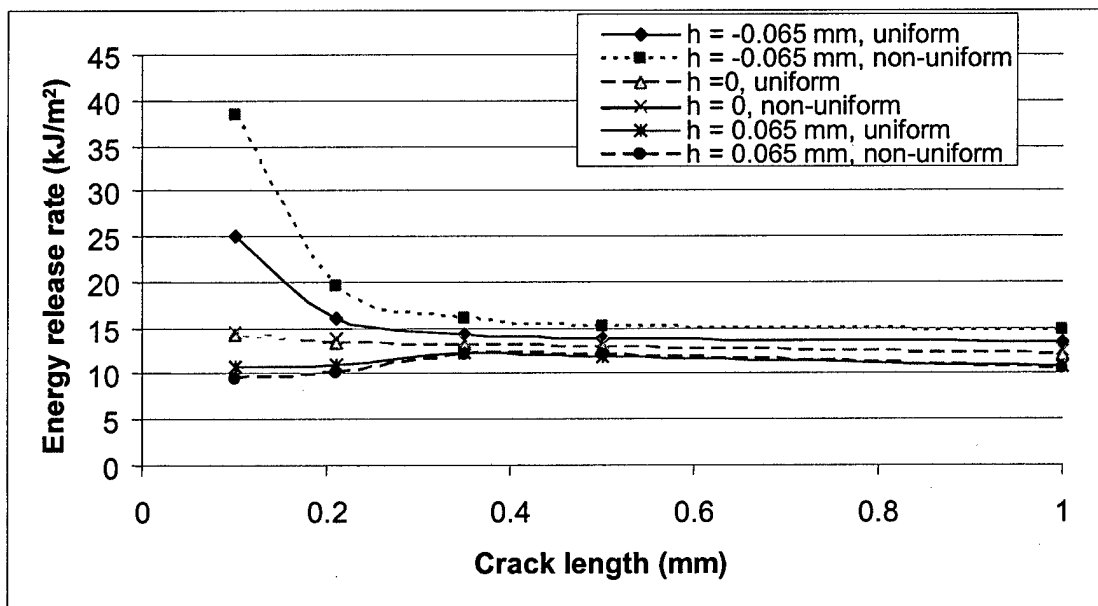


Figure 97. Energy release rate crack length sensitivity of an internal T-shaped crack.

Figure 97 shows that:

- (1). As the crack length increase, the energy release rate tends to a constant.
- (2). When the crack lies on the bottom interface of the adhesive layer ($h = -0.065 \text{ mm}$), small cracks can give a very high energy release rate, because of the high stress concentration here.
- (3). Uniform adhesive model usually gives an under-estimation on the energy release rate, especially for serious stress concentration case ($h = -0.065 \text{ mm}$).

Figures 98-99 show the stress intensity factors results for different crack length.

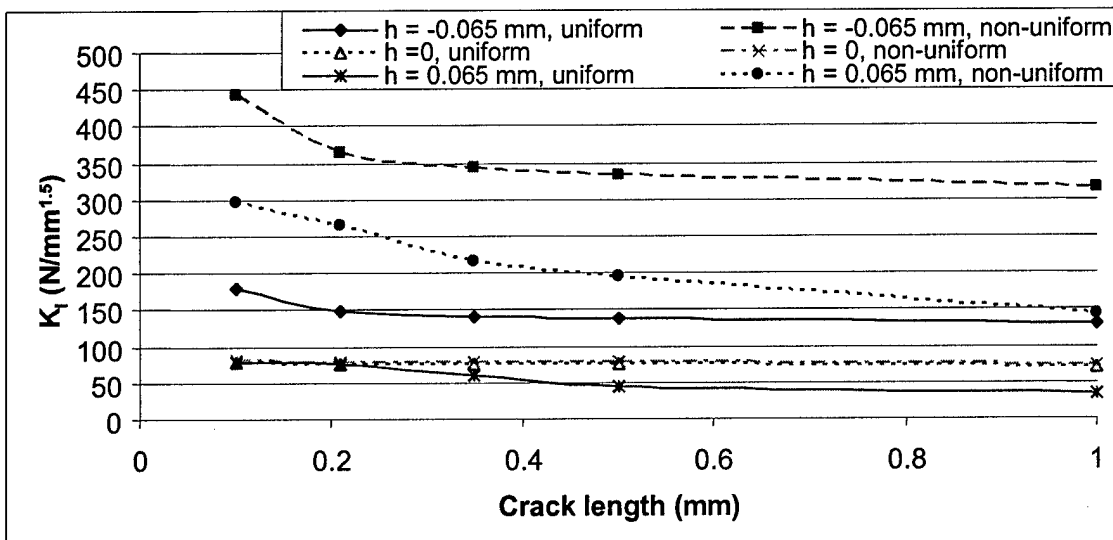


Figure 98. K_I crack length sensitivity of an internal T-shaped crack.

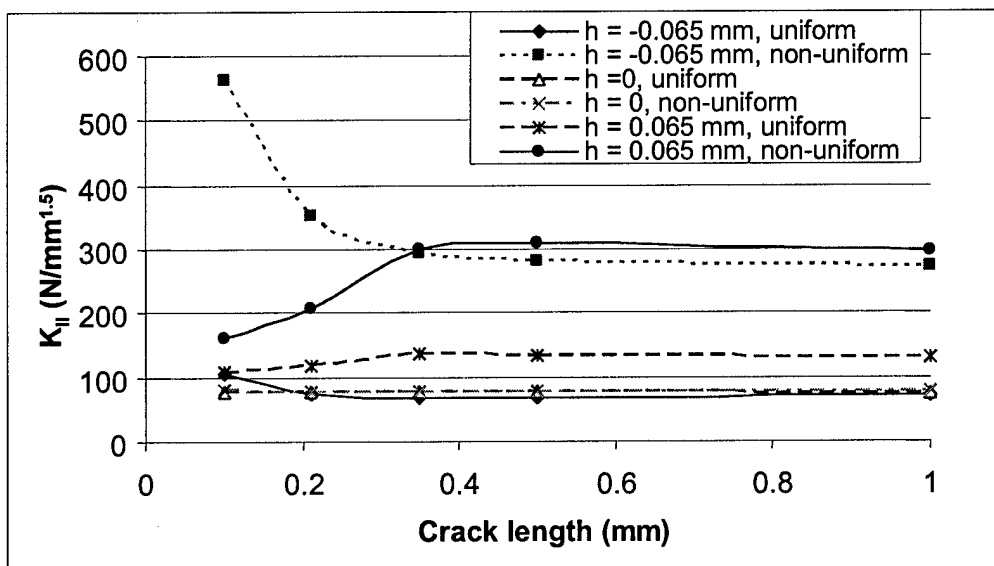


Figure 99. K_{II} crack length sensitivity of an internal T-shaped crack

From Figures 98-99, we can conclude the following:

- (1). For both K_I and K_{II} , non-uniform adhesive model, which includes the adhesive interfacial modulus gradient effects, gives a much higher value than uniform adhesive model does.
- (2). On the bottom interface of the adhesive layer, the stress concentration problem is more serious than that on the top adhesive interface or the centerline of the adhesive.
- (3). K_I and K_{II} are of the same order, so it is a mixed loading case. Both the open and the shear effects are significant.

6.4 CONCLUSIONS

Nano-indentation tests for aluminum/epoxy interface properties, FT-IR analysis of epoxy adhesive curing chemistry, and FEA models including the interface effects are studied in this chapter. From the results discussed above, we conclude the following:

1. The interface effects on the adhesive modulus are significant on the modulus distribution of adhesive in aluminum adhesive joints. The modulus is shown to vary by several hundred percent near the interface.
2. The adhesive modulus non-uniformity near the interface is believed to be the result of the non-uniform curing reaction of the adhesive.
3. The interface effects on the adhesive modulus should be taken into consideration in adhesive joint design. The energy release rate is under-predicted without incorporation of interface effects.

7 NANO-ENGINEERED ADHESIVE JOINTS DESIGNS

In this section, nano-clay reinforced epoxy adhesive was applied in order to improve the performance of adhesive joints. There are already many reports on the performance of uniformly distributed nano-clay/polymer composite systems. In our research, we distribute nano-clay in specific locations of the adhesive layer in order to get the best results. There are mainly two nano-engineered adhesive joint designs discussed: layered, nano-clay reinforced epoxy adhesive joints and joints with adhesive modulus distribution designed along the loading direction. FEA results show that both layered, nano-clay reinforced epoxy adhesive joints and joints with adhesive modulus distribution design along the loading direction can give new methods in reducing the stress concentration for joint structures. FEA results show both methods are effective. An experimental study was done to conform the effects of layered, nano-clay reinforced epoxy adhesive joints.

7.1 CLOISITE® 30B ORGANIC NANOCLAY

The nano-clay used in our research was Cloisite® 30B from Southern Clay Products Co. Cloisite® 30B is a natural montmorillonite modified with a quaternary ammonium salt^[86]. The chemical structure of montmorillonite is $(\text{Na, Ca})(\text{Al, Mg})_6(\text{Si}_4\text{O}_{10})_3(\text{OH})_6 - \text{nH}_2\text{O}$, its chemical name is “Hydrated Sodium Calcium Aluminum Magnesium Silicate Hydroxide”. The structure of this group is composed of silicate layers sandwiching a gibbsite (or brucite) layer in between, in an s-g-s stacking sequence. The variable amounts of water molecules would lie between the s-g-s sandwiches^[87]. There are exchangeable cations (Na^+) lying in the interlayer region. Depending on the ratio of Na^+ and Ca^{2+} , montmorillonite can be divided into sodium rich montmorillonite and calcium rich montmorillonite. As Ca^{2+} is difficult to be exchanged, sodium

rich montmorillonite is preferred in making organic nanoclay. Some mechanical properties of sodium rich montmorillonite were listed in Table 3 [88].

Table 3. Mechanical properties of montmorillonite (sodium rich)

Average bulk modulus, K (GPa)	35.3
Average shear modulus, G (GPa)	20.2
Poisson's Ratio, ν	0.260

The tensile modulus E of this material can be calculated from Equation (45)^[90]:

$$G = \frac{E}{2(1+\nu)} \quad (45)$$

Using the data in Table 3, $E = 50.9$ GPa.

Layered montmorillonite can be treated using mild acid, giving its acidic analogue, which has silanol groups in the interlayer region. Various organic function groups can be grafted onto montmorillonite by reacting with those silanol groups. This process is called intercalation. The intercalation ability of magadiite, which has a similar structure to montmorillonite, has been relatively well investigated ^[90, 91]. The procedure includes 3 steps:

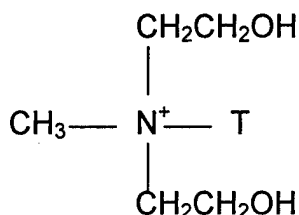
- (i). ion exchange with organic cations,
- (ii). adsorption of polar organic molecules to ions by dipolar interactions and/or to silanol groups by hydrogen bonds, and
- (iii). silylation and esterification of interlayer silanol groups.

In an early stage of investigation on magadiite intercalation, Lagaly et al. [91] mentioned that caprolatam and acrylamide were intercalated into H-magadiite and polymerized in the interlayer space. Sugahara et al. [93] reported intercalation of poly(acrylonitrile) into magadiite. The procedure is:

- (i). Ion exchange. A $\text{C}_{12}\text{H}_{25}\text{N}(\text{CH}_3)_3^+$ -magadiite is prepared by ion exchange.
- (ii). Monomer intercalation. The system is soaked in acrylonitrile monomer containing 0.7 wt % benzoyl peroxide as an initiator for 24 hours.
- (iii). Polymerization. The mixture is heated at 50 °C for 24 hours .
- (iv). Heat treatment. The product is heated to 1300 °C, to get β-SiC ceramics.

Recently, Wang et al. have investigated the exfoliation of magadiite in an epoxy matrix [94-95]. Depending on the kind of interlayer ions, intercalated or exfoliated magadiite nanocomposites are obtained. The exfoliated nanocomposites are typically disordered, but a new type of exfoliated structure is also observed in which the nanolayers are regularly spaced over long distances (e.g., ~8 nm). The tensile properties of the polymer matrices are greatly improved by the reinforcement effect of the silicate nano-layers.

Chemical modification of montmorillonite is similar to that for magadiite. Southern Clay Products Co. used methyl, tallow, bis-2-hydroxyethyl, quaternary ammonium (MT_2EtOT) as the organic modifier [87]. The structure of MT_2EtOT is shown in Figure 100.



T is Tallow (~65% C₁₈, ~30% C₁₆, ~5% C₁₄)

Figure 100. Structure of MT₂EtOT

Some properties of Cloisite® 30B is listed in Table 4 [87].

Table 4. Properties of Cloisite® 30B

Organic modifier	MT2EtOT
Modifier concentration	90 meq/100g clay
% Moisture	< 2
% Weight loss on ignition	30
Typical dry particle diameters (by volume)	10% less than 2μ 50% less than 6μ 90% less than 13μ
Density	Loose bulk: 14.25 lb/ft ³ Packed bulk: 22.71 lb/ft ³ Specific gravity: 1.98 g/cc
X ray results	d ₀₀₁ = 18.5 Å

The epoxy system used in our research is Araldite GY 502 and the amine hardener is Aradur 955-1US, both from Huntsman Advanced Materials Co. The specific gravity of the cured epoxy system is 1.2.

7.2 MEAN FIELD METHOD TO CALCULATE EQUIVALENT MECHANICAL PROPERTY OF NANO-CLAY/EPOXY COMPOSITE SYSTEMS

Assuming the Cloisite® 30B organic nano-clay was randomly distributed in the epoxy system, the equivalent modulus and Poisson's ratios of clay/epoxy composite systems were calculated using the mean field method [94].

The mean-field theory (MFT) is based on the premise that volume averages of inhomogeneities suffice in estimating the transport properties on the macro-scale. It has already been successfully used in simulating the effects of micro-defects on bulk materials [95-97]. The condition to apply mean-field theory is that the inhomogeneities in the system are isolated from each other. For low to moderate concentrations of nanoclay reinforced composite materials, this condition is approximately satisfied.

In this analysis, the nanoclay particles are idealized as disk-shaped inclusions embedded in an isotropic and homogenous elastic media. Each nanoclay particle is idealized as circular in shape with radius R and thickness $2t$ (Figure 101) [98]. The aspect ratio of the disc radius to thickness α is denoted by

$$\alpha = \frac{R}{2a} \quad (46)$$

and for properly prepared nanoclay, $\alpha \gg 1$.

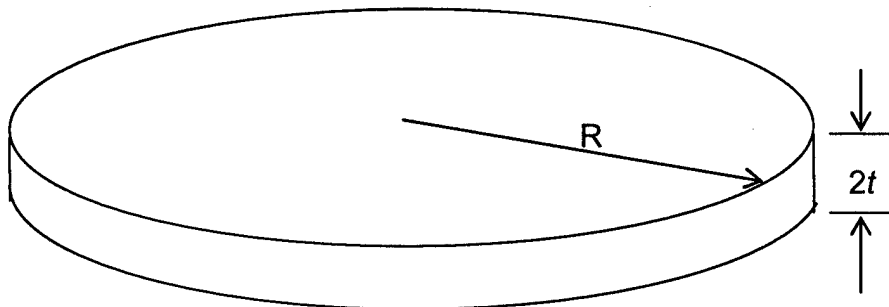


Figure 101. Idealized geometry of nanoclay particles

A popular model belonging to the class of MFT is the self-consistent method (SCM). SCM consists of estimating the elastic parameters of a representative volume element (RVE) by placing successively the inclusions or inhomogeneities (such as nanoclays) in a fictitious homogenous medium with the yet-unknown overall properties of the composite (nanoclay reinforced polymer matrix).

The Mori-Tanaka (MT) method is yet another variation of self-consistent method [100, 101]. In this method all inclusions (nanoclay) are assumed to be embedded in a matrix that is subjected at large distances to the mean strain experienced by the inclusion.

Chen, et al. [101] provide the expressions for overall elastic moduli of a matrix material reinforced with disk-like inclusions, evaluated with the help of the Mori-Tanaka method. The effective moduli are functions of the elastic moduli of the constituents, the matrix and the inclusion, as well as the volume fraction f of the inclusion. In the subsequent expressions, the subscripts 0 and 1 refer to the matrix and the nanoclay inclusion, respectively, while the unsubscripted variables refer to the effective media of the composite.

For a parallel array of inclusions, the equivalent shear modulus (G) and the Bulk modulus (K) of the nanoclay reinforced composite material are given by:

$$G = j \quad (47)$$

$$K = k - \frac{G}{3} \quad (48)$$

where j and k are determined from the following set of nonlinear equations:

$$\frac{1}{j} = \frac{1-f}{j_0} + \frac{f}{j_1} \quad (49)$$

$$k = (1-f)k_0 + fk_1 + \frac{l^2}{n} - (1-f)\frac{l_0^2}{n_0} - f\frac{l_1^2}{n_1} \quad (50)$$

$$\frac{1}{n} = \frac{1-f}{n_0} + \frac{f}{n_1} \quad (51)$$

$$\frac{l}{n} = (1-f)\frac{l_0}{n_0} + f\frac{l_1}{n_1} \quad (52)$$

The parameters j_i , k_i , l_i and n_i define the elastic parameters of transversely isotropic elastic media, and are related to the respective bulk (K_i) and shear modulus (G_i) by Equations (53-56), ($i = 0, 1$):

$$j_i = G_i \quad (53)$$

$$k_i = K_i + \frac{G_i}{3} \quad (54)$$

$$l_i = K_i - \frac{2}{3}G_i \quad (55)$$

$$n_i = K_i + \frac{4}{3}G_i \quad (56)$$

The calculation for randomly distributed nanoclay is based on Equations (57-58) [102].

$$K = K_1 - (1-f) \frac{K_1 - K_0}{1-f \frac{3(K_1 - K_0)}{3K_1 + 4G_1}} \quad (57)$$

$$G = G_1 - (1-f) \frac{G_1 - G_0}{1 - \frac{4}{5}f \frac{G_1 - G_0}{3K_1 + 4G_1} - \frac{2}{5}f \frac{G_1 - G_0}{G_1}} \quad (58)$$

where again K is the bulk modulus, G is the shear modulus, f is the volume fraction of reinforced material (nanoclay), the subscripts 0 and 1 refer to the matrix and the clay, respectively, while the unsubscripted variables refer to the effective material properties for the composite.

The relationships between Young's modulus E , Poisson's ratio ν , bulk modulus K , and shear modulus, G are listed in Equations (59-62).

$$K = \frac{E}{3(1-2\nu)} \quad (59)$$

$$G = \frac{E}{2(1+\nu)} \quad (60)$$

$$E = \frac{9KG}{3K+G} \quad (61)$$

$$\nu = \frac{3K-2G}{6K+2G} \quad (62)$$

The tensile modulus of the cured epoxy system (non-reinforced) is 0.7 GPa (From IFM nano-indentation test), and the Poisson's ratio is 0.4. From Equations (47-48), we can get:

$K_0 = 1.167$ GPa, and $G_0 = 0.25$ GPa. The material properties for Cloisite® 30B nano-clay was listed in Table 3. the relation between clay volume constant f and clay weight constant c is:

$$f = \frac{c / \rho_1}{(1 - c) / \rho_0 + c / \rho_1} \quad (63)$$

where again ρ is the density, the subscripts 0 and 1 refer to the matrix and the clay.

The modulus results of the clay/epoxy composite systems are shown in Figure 102. Table 5 shows the materials properties of clay/epoxy composite systems used in our experiments.

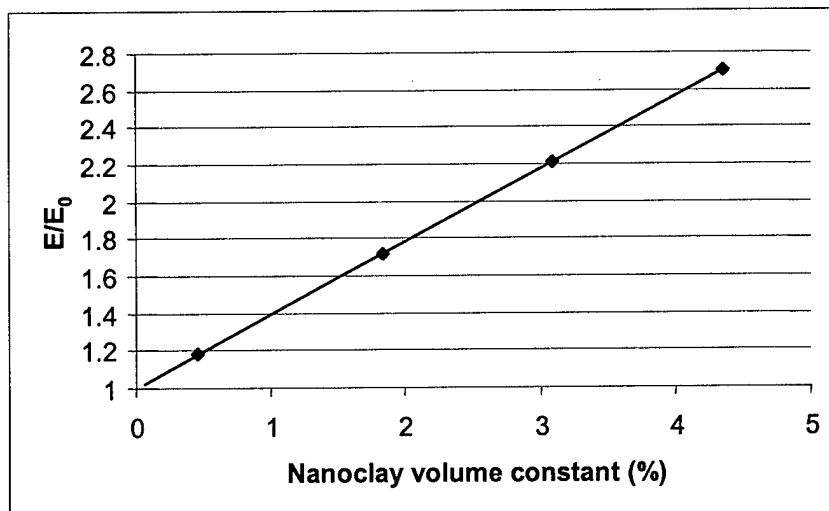


Figure 102. Effects of nanoclay reinforcement on the Young's modulus in clay/epoxy composite systems.

Table 5. Moduli of selected clay/epoxy composite systems

Clay constant (wt%)	Clay volume constant (%)	K (GPa)	G (GPa)	E (GPa)	ν	E/E_0
0.75	0.456	1.237456	0.297361	0.825925	0.38876	1.179893
3	1.84	1.453474	0.442387	1.204915	0.361835	1.721307
5	3.09	1.651445	0.575054	1.545746	0.344001	2.208208
7	4.36	1.855432	0.711511	1.89261	0.329994	2.703729

7.3 LOW/HIGH/LOW 3 LAYERED ADHESIVE JOINT

A. FEA Model in Simulating Low/High/Low 3 Layered Adhesive Joint

In order to improve the performance of a single strap adhesive joint, the Cloisite® 30B organic nano-clay was used to reinforce the adhesive layer. Two types of adhesive design were given. The first one was called “low/high/low 3 layered adhesive joint” (L/H/L). The effects of this design were verified using FEA and experiments. Figure 103 gives the structure of “low/high/low 3 layered adhesive joint”

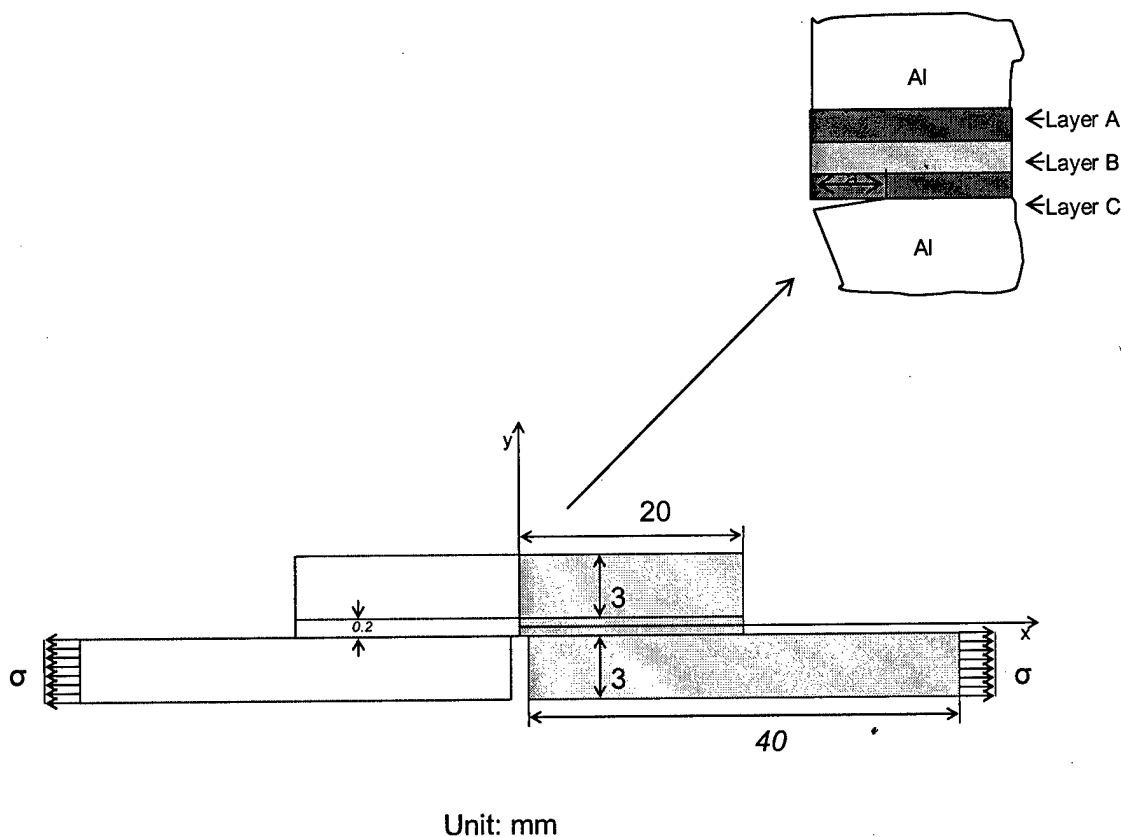


Figure 103. Structure of the low/high/low 3 layered adhesive joint.

In Figure 103, the x-axis is on the centerline of the adhesive layer, and y-axis is the symmetric axis of the single strap joint. In order to make fracture mechanics analysis, there was a pre-

initiated, internal paralleled crack with the length of a in the FEA model of the joints. The adhesive consists of 3 nano-clay/epoxy composite layers with different nano-clay weight constants. The layer thickness is 0.2 mm each. Both Layer A and Layer C always had 0.75% weight constants nano-clay. The nano-clay weight constant in Layer B was varying, using 0.75%, 3 %, 5% or 7%. The mechanical properties of the aluminum adherends are tensile modulus 70 GPa and Poisson's ratio 0.33. The mechanical properties of Layers A, B, and C were given in Table 5.

From stress analysis and the energy release rate analysis discussed for single-strap adhesive joints (Chapter 5), we know the most probable failure initiate position is on the bottom interface of the adhesive layer and in the center of the joint ($x = 0$, $y = -0.1$ mm in Figure 103). So we assume a crack propagation starting from this position. We set an initial crack at this position. This crack doesn't exist in processing of the experimental adhesive joint samples. It would be generated automatically at the beginning of the joints failure. With different nano-clay constants in Layer B, fracture mechanics FEA analysis was carried out. The results were shown in Figure 104-106 (the group of "0.75% nano clay" is uniform adhesive group).

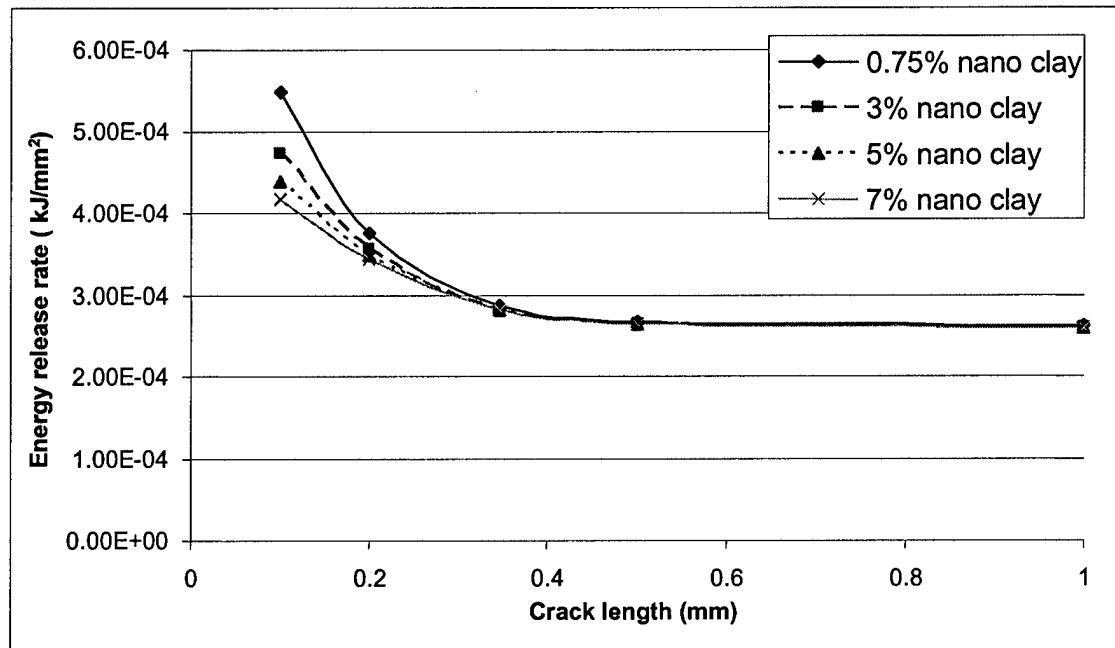


Figure 104. The crack length sensitivity of energy release rate, with respect to different nano-clay constants in Layer B.

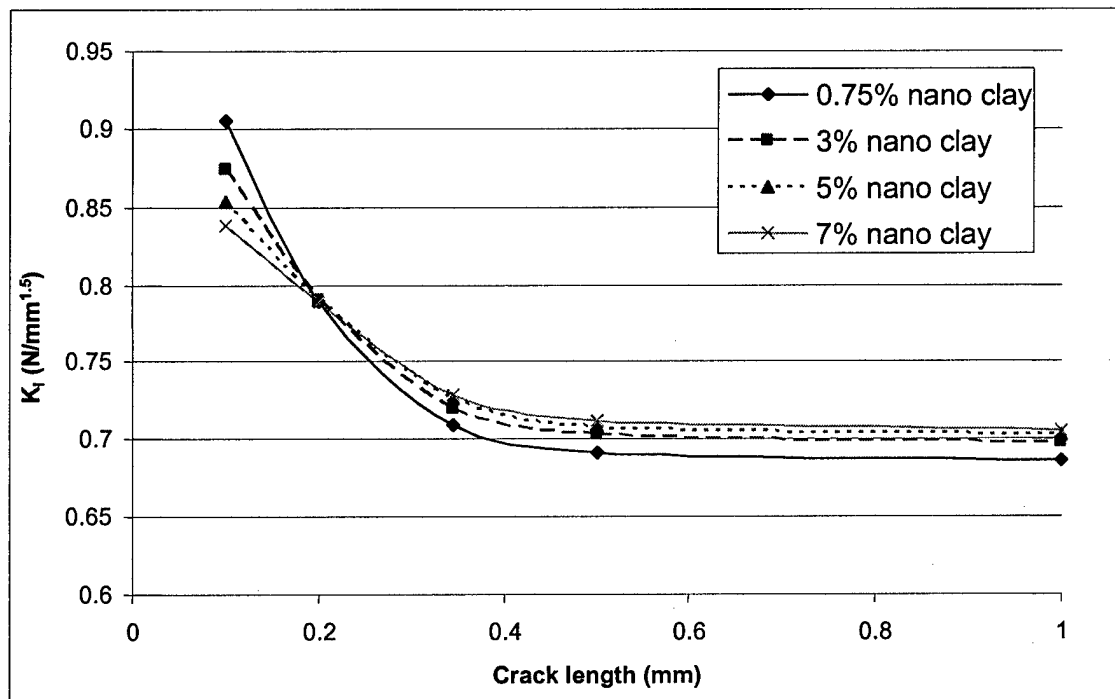


Figure 105. The crack length sensitivity of K_I , with respect to different nano-clay constants in Layer B.

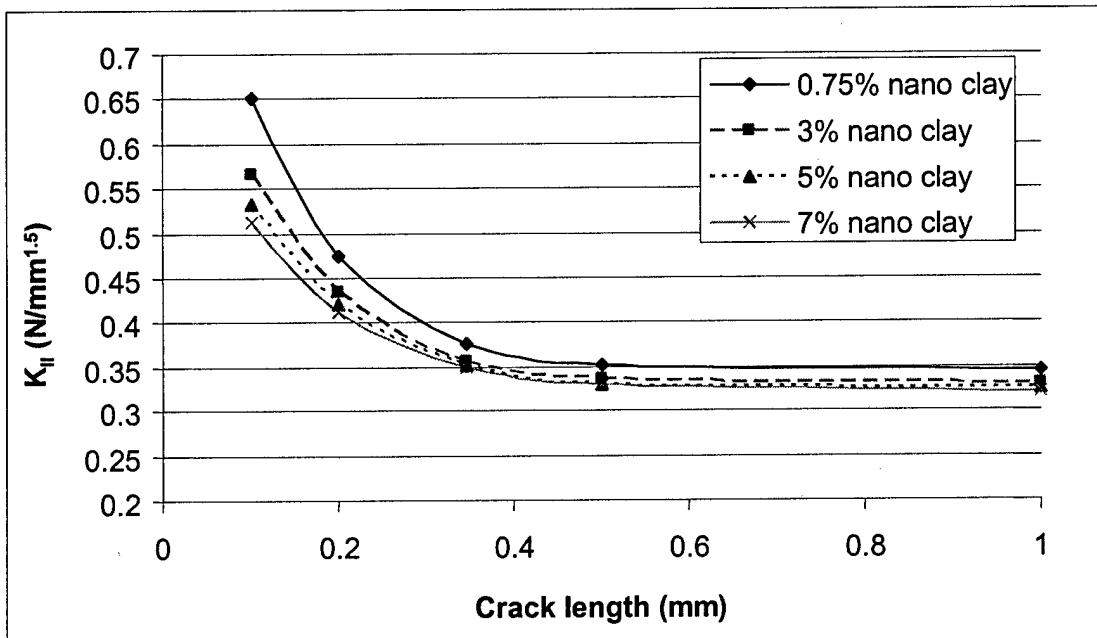


Figure 106. The crack length sensitivity of K_{II} , with respect to different nano-clay constants in Layer B.

From Figure 104-106, we can conclude as following:

1. Horizontal tensile loading results in a mix loading on a single-strap adhesive joint (Mode I and Mode II).
2. The stress concentration effects can be reduced when an internal paralleled crack propagates.

Usually energy release rate increases with the crack length (Equations (28 and 29)), but for a single strap adhesive joint, both energy release rate and stress intensity factors (K_I and K_{II}) are high for small crack length, and decrease with the crack length. Once the crack length reach at 2% of the overlap length, the energy release rate and stress intensity factors approach a constant value.

3. For Mode II loading, a stiffer middle layer always more greatly reduces the stress concentration effects (Figure 106). But for Model I loading, a stiffer middle layer is less effective in reducing the stress concentration effects for long cracks (when crack length is bigger than 1% of the overlap length). See Figure 105.
4. In summary, the layer reduces the energy release rate of the single-strap adhesive joints.

B. Experimental Test of Low/High/Low 3 Layered Adhesive Joint

A tensile test was applied to the low/high/low 3 layered adhesive joint samples using a MTS 860 system. The load speed in the test was 0.2 mm/min. The test results are listed in Table 6 and Figure 107.

Table 6. Tensile test results for low/high/low 3 layered adhesive joints

Mid-layer nano-clay contant (wt %)	Strength (MPa)	Standard Deviation (MPa)
0.75 (uniform adhesive)	10.50	1.067
3	11.47	1.448
5	13.12	1.521
7	13.79	1.217

The outer layers have a 0.75 wt% clay loading.

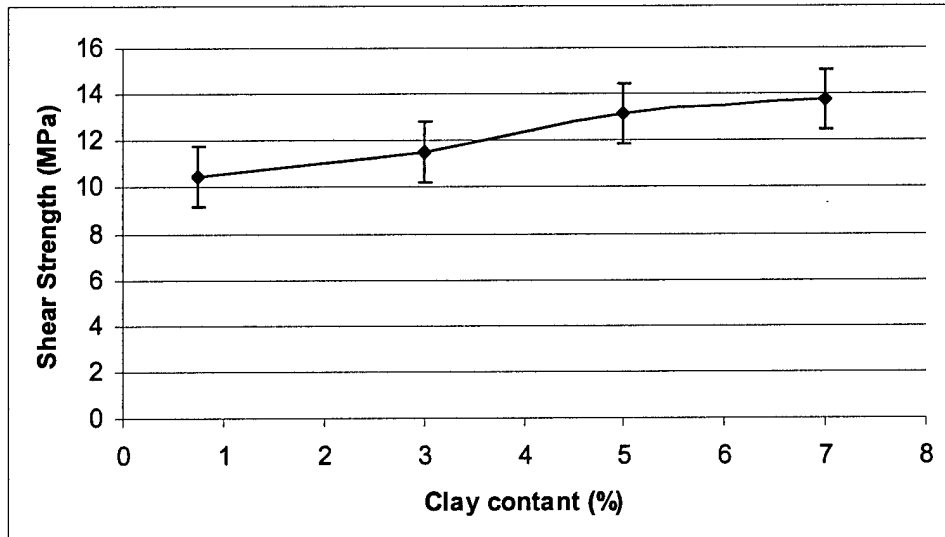


Figure 107. Tensile test results for low/high/low 3 layered adhesive joints

From Table 6 and Figure 107, we see that to reinforce the middle layer obviously improves the adhesive joint performance (around 35% for 7 wt % nano-clay constant). The reinforcement effect is more significant between 0.75% to 5% than that between 5% to 7%. We believe that is because of the increase of defects in the reinforced epoxy adhesive. Similar results on nano-clay/epoxy composites were reported by Lan et al.^[102], which makes us believe that our results are reasonable.

We also tried the “high/low/high” (H/L/H) design for a single strap adhesive joint. FEA results show that under the same tensile loading, it generates a higher energy release rate, and higher stress intensity factors in an H/L/H adhesive joint than in a uniform adhesive joint. So (H/L/H) single strap adhesive joint design is not reasonable.

7.4 LOADING DIRECTION DISTRIBUTED MODULUS (LDDM) ADHESIVE JOINTS

The model used in this section is the same as that shown in Figure 108, without any cracks. The load σ is 1 MPa. The origin of the co-ordinate system is at the center of the joint. The adhesive modulus is distributed along the loading direction (x direction). The material properties for the aluminum adherends are modulus $E = 70$ GPa and Poisson's ratio $\nu = 0.3$.

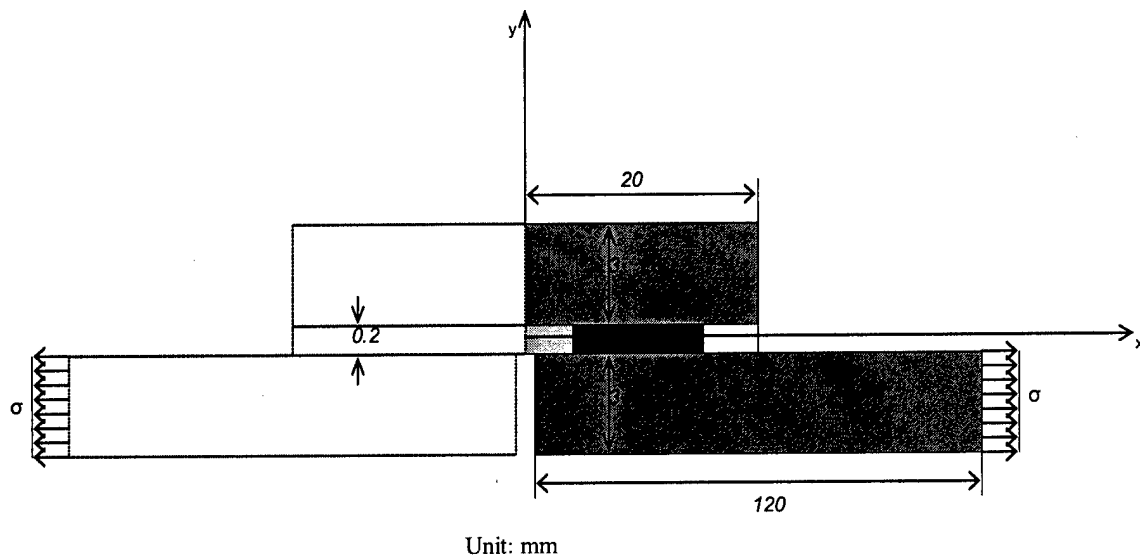


Figure 108. Model of a LDDM joint.

A. Static Stress FEA for LDDM Joints

A joint structure has significant stress concentration. Figure 109 shows the stress distribution for a joint with uniform adhesive. Are there some "internal" methods to make the stress distribution more even? In the method of adhesive modulus distribution design, low modulus materials are applied in the regions originally with high stress concentration, so that larger deformations in these regions occur. Then in the middle part of the joint, which used to support very small stress,

will then have a larger deformation, and higher stress. The total effect should be a more evenly distributed stress field in the adhesive joint.

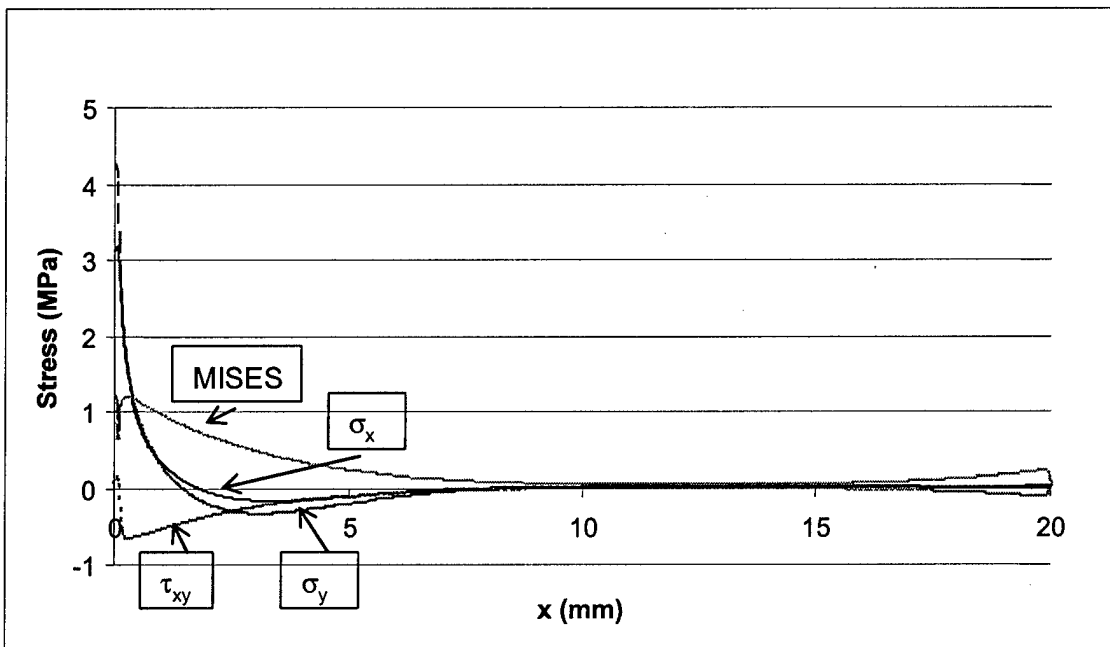


Figure 109. Stress distributions in a joint with uniform adhesive

Table 7 gives the adhesive modulus distribution design for LDDM joints.

Table 7. The adhesive modulus distribution design for LDDM joints.

	modulus (MPa)	Start x co- ordinate	End x co- ordinate
Case 1 design	600	0	4.680674
	1200	4.680674	6.282022
	3500	6.282022	7.214831
	5200	7.214831	18.2087043
	3500	18.2087043	19.7353386
	1850	19.7353386	20
Case 2 design	165	0	4.383371
	625	4.383371	7.641573
	3000	7.641573	9.018876
	5200	9.018876	19.0666947
	735	19.0666947	20

The effects of the adhesive modulus distribution design are shown in Figures 110 -112.

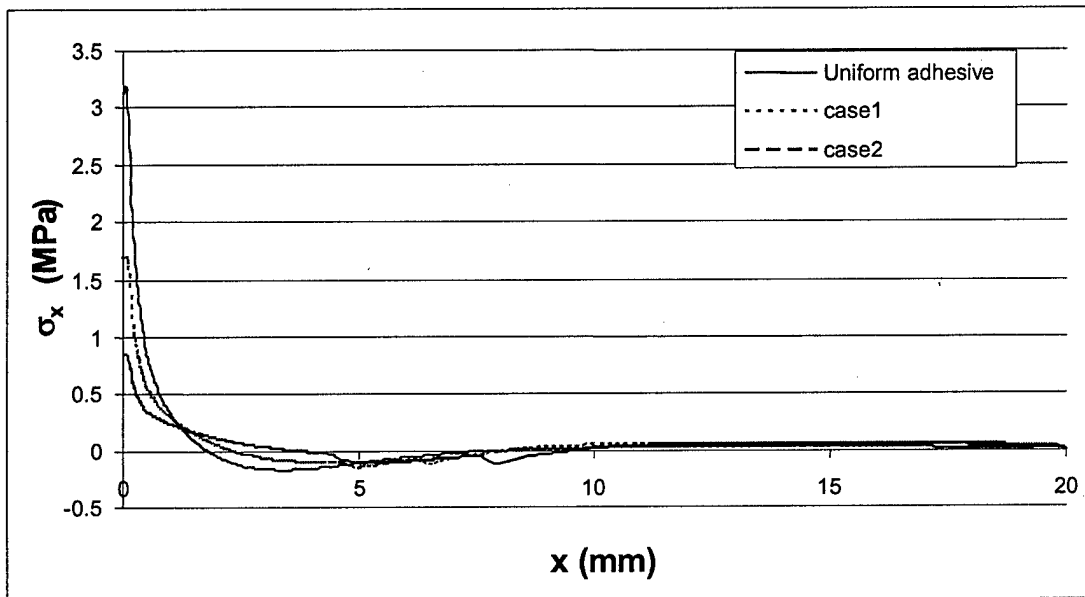


Figure 110. Tensile stress distributions in LDDM joints

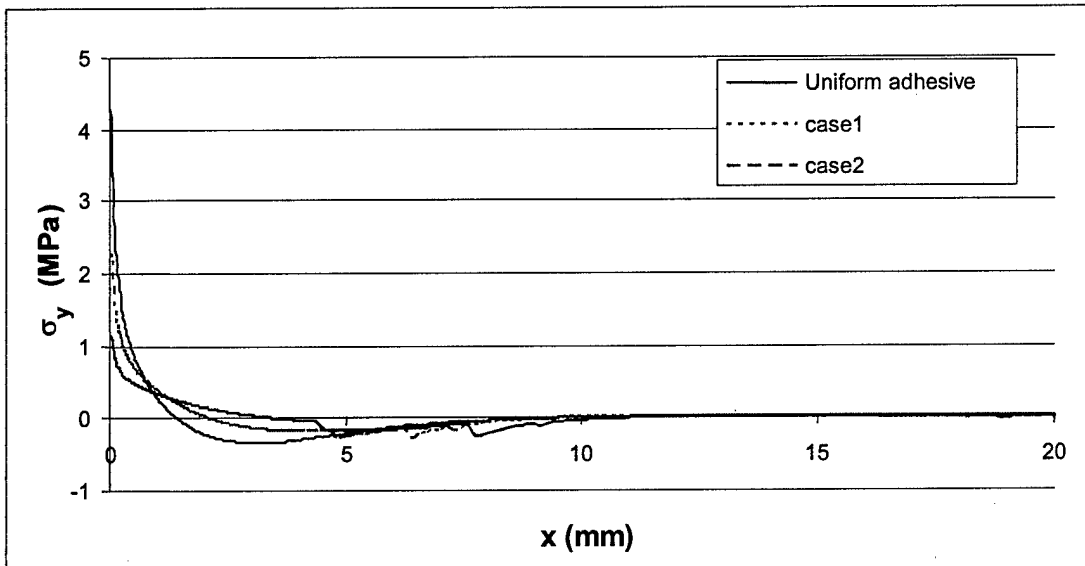


Figure 111. Peeling stress distributions in LDDM joints.

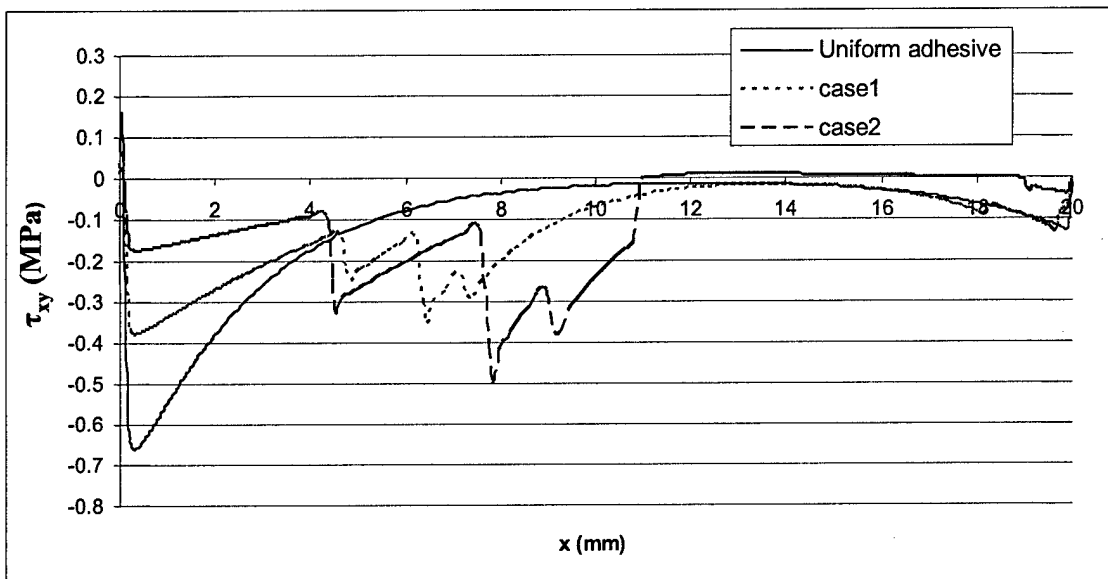


Figure 112. Shear stress distributions in LDDMs.

FEA results shown in Figures 110-112 are encouraging. Both Case I and Case II designs can greatly reduce the stress concentration. The maximum stress was reduced to less than half comparing with the uniform adhesive joints.

B. Fracture Mechanics FEA for LDDM Joints

As there exists the singularity problem in single-strap adhesive joints, stress analysis is not sufficient for joints design. Fracture mechanics analysis was also carried out in our research. The results are shown in Figure 113-115.

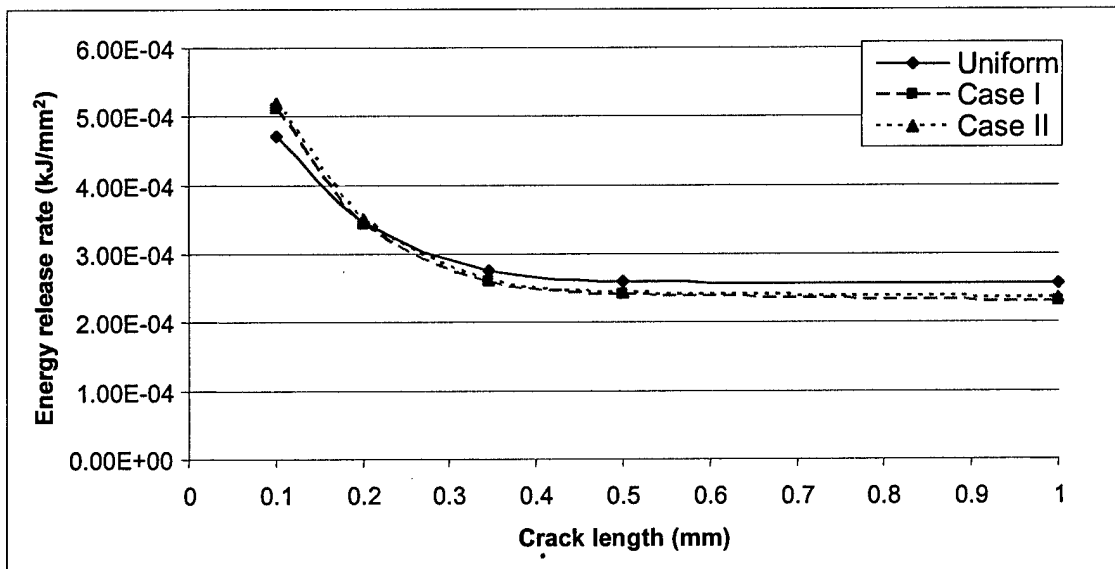


Figure 113. The crack length sensitivity of energy release rate, with respect to different LDDM adhesive design cases.

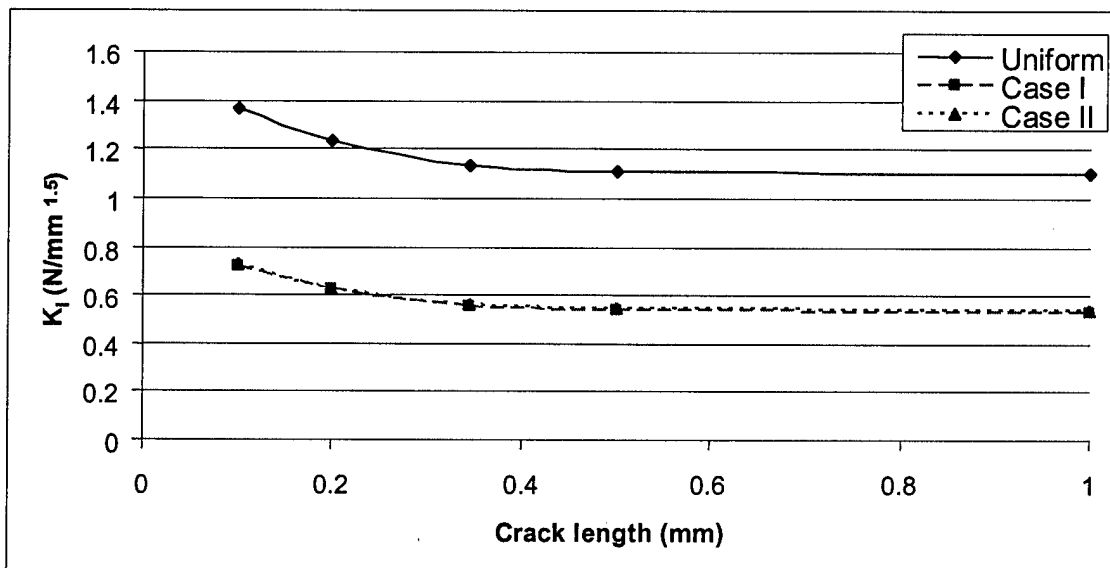


Figure 114. The crack length sensitivity of K_I , with respect to different LDDM adhesive design cases.

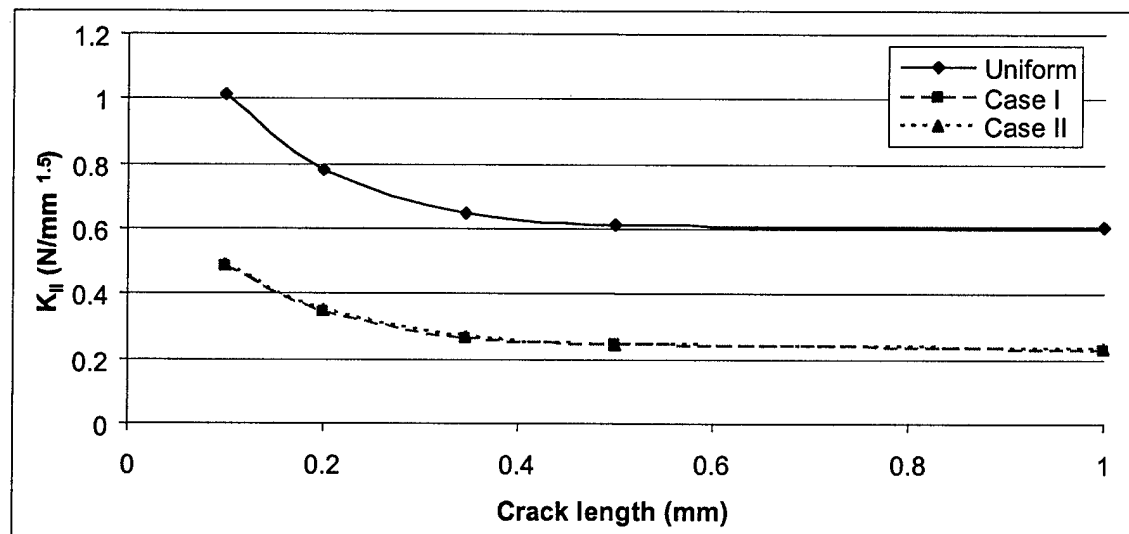


Figure 115. The crack length sensitivity of K_{II} , with respect to different LDDM adhesive design cases.

The loading direction distributed modulus adhesive joint designs (Case I and Case II) can greatly reduce the stress concentration problem, the energy release rate doesn't change a lot (see Figure 113). The reason is that energy release rate was determined by not only stress but also strain. Its physical meaning is the energy applied on a unit area of material under a given loading condition. So if two materials have different moduli, the one with the lower modulus gives a higher energy release rate for the same stress. From this point of view, we think the stress intensity factors may be better design parameters in this case, because the modulus is different for the three adhesive design cases (see Table 7).

Figures 114-115 show the adhesive design effects on reduce the stress concentration is significant. Both Case I and Case II designs reduced concentrations for about 50% stress.

7.5 CONCLUSION

In this chapter, we discussed the design of the adhesive layers, to optimize the overall performance of adhesive joints. Nano-clay reinforcement was one method to adjust the modulus of adhesive layer. The other was loading direction distributed modulus adhesive joints. We conclude the following:

- (1) Suitable design of the adhesive modulus distribution can greatly reduce the stress concentration.
- (2) As a result of (1), adhesive modulus distribution can have significant effects on the energy release rate and stress intensity factors.
- (3) Two types of adhesive modulus distribution designs are suggested in this chapter: low/high/low adhesive design and loading direction distributed modulus adhesive joints. Both of them can significantly improve the adhesive joints' performance.

CHAPTER 8 CONCLUSION

The research presented here included composite material modeling, fracture mechanics modeling of adhesive joints, nano-indentation for Al/epoxy interfacial properties, FT-IR curing chemistry study of epoxy system, fracture mechanics finite element analysis with Al/epoxy interfacial properties, and nano-engineered adhesive joint design. The conclusions we draw from our research are:

- (1) A layered model is more suitable in simulating composite adhesive joint than traditional orthotropic model.
- (2) The method to determine nine engineering constants of composite materials in the layered model was presented.
- (3) Because of the singularity problem, fracture mechanics analysis is necessary in adhesive joint design.
- (4) The suitable mesh density for fracture mechanics analysis in most adhesive designs was demonstrated $b/a = 0.06$.
- (5) Stress intensity factors (K_I, K_{II}) are useful in comparing structures (or locations) with different moduli, because stress intensity factors are functions of stress distributions, and independent from material modulus. This is the reason the results of stress intensity factors showed the stress concentration effects on the interface better than the energy release rate.
- (6) For single-strap adhesive joints, failure begins from the lower adhesive/adherend interface.

- (7) The interface effects on the adhesive modulus are significant on the modulus distribution of adhesive in aluminum adhesive joints. The modulus is shown to vary by several hundred percent near the interface.
- (8) The interface effects on the adhesive modulus should be taken into consideration in adhesive joint design. The energy release rate is under-predicted without incorporation of interface effects.
- (9) Two nano-engineered adhesive designs were given, and they were shown to be effective.

9. FUTURE WORK

In the future, additional efforts would improve our research:

- (1) Combine the layered model for composite materials with the fracture analysis for composite adhesive joints. The fracture mechanics analysis we performed was for metal adherends.
- (2) Include the Al/epoxy interfacial properties in nano-engineered adhesive joints design.
- (3) Look for new methods to adjust the adhesive modulus and improve its strength. POSS is possibly a more effective reinforcing material for the adhesive than nano-clay.

10. ACKNOWLEDGEMENT

The authors would like to express their appreciation to Dr. Charles Lee and the AFOSR for their support of this work. The authors also acknowledgement the contributions to this work of the following persons:

- Dr. Wei Chian, PhD (Post-Doctoral Associate), Chemical Engineering Dept., SDSM&T
- Mr. Lu Min, Doctoral student in Materials Engineering and Science, SDSM&T

- Ms. Sailaja Chada, MS student in Chemical Engineering, SDSM&T
- Mr. Sattesh Battula, MS student in Chemical Engineering, SDSM&T

REFERENCES:

- [1] Klenner, J, "A380- the latest step in structure technology", Keynote Lecture, *45th AIAA/ASME/ASCE/AHS/ASC Structures, Structure Dynamics, and Materials Conference*, April 19-22, 2004, Palm Springs, CA, (2004)
- [2] Debski, D.K.; Debski, M.A.; and Golos, K.M., "Composite joints of aerostructures", <http://www.ilot.edu.pl/STRANG/Designs/CJoA.pdf>, (2004)
- [3] Oterkus, E.; Barut, A.; Madenci, E.; Smeltzer, S. and Ambur, D., "Nonlinear Analysis of Bonded Composite Single-Lap joints", *45th AIAA/ASME/ASCE/AHS/ASC Structures, Structural Dynamics & Materials Conference*, Palm Springs, California, 19 - 23, April, AIAA Paper 2004-1560, (2004)
- [4] Hart-Smith, L.J., "Advances in the analysis and design of adhesive-bonded joints in composite aerospace structure", *SAMPE Process Engineering Series*, **19**, SAMPE, Azusa, p. 722-737, (1974).
- [5] Hart-Smith, L.J., "Adhesively bonded joints in fibrous composite structures", *Douglas Aircraft Paper 7740*, presented to the international symposium on Joining and Repair of Fiber-Reinforced Plastics, Imperial College, London, (1986)
- [6] Hart-Smith, L.J., "Adhesive bonded double lap joints", *NASA Langley Contractor Report*, NASA CR-112235, (1973)

[7] Hart-Smith, L.J., "Differences between adhesive behavior in test coupons and structural joints", *USAF Contract Report AFWAL-TR-81-3154*, Vol. I and II, February, (1982)

[8] Hart-Smith, L.J., "Design methodology for bonded-bolted composite joints", Douglas Aircraft Company, *USAF Contract Report AFWAL-TR-81-3154*, Vol. I and II, February, (1982)

[9] Hart-Smith, L.J., "Induced peel stresses in adhesive-bonded joints", Douglas Aircraft Company, *Technical Report MDC-J9422A*, August, (1982)

[10] Sperling, L.H., "Polymer viscoelasticity and rheology", INTRODUCTION TO PHYSICAL POLYMER SCIENCE, Third Edition, Published by John Wiley & Sons, Inc., P. 433 (2001)

[11] Roy, S.; Reddy, J. N., "Finite element analysis of adhesively bonded composite joints with moisture diffusion and delayed failure", *Computers and Structures* **29(6)** p. 1011, (1988)

[12] Yadagiri, S.; Papi Reddy, C.; Sanjeeva Reddy, T., "Viscoelastic analysis of adhesively bonded joints", *Computers and Structures*, **27(4)** p. 445, (1987)

[13] U.S. Department of Defense, "Adhesive joints", *Military Handbook - MIL-HDBK-17-3F: Composite Materials Handbook, Volume 3 - Polymer Matrix Composites Materials Usage, Design, and Analysis*, P. 5-7, (2002)

[14] Hart-Smith, L.J.; Brown, D.; and Wang, S., "Surface preparations for ensuring that glue will stick in bonded composite structures", *10th DoD/NASA/FAA conference on Fibrous Composite in Structure Design*, Hilton Head Is, SC, (1993)

[15] Hart-Smith, L.J. "Effects of adhesive layer edge thickness on strength of adhesive-bonded joints", Quarterly Progress Report, No. 3, *Air Force Contract F33615-80-C-5092*, (1981)

[16] Hart-Smith, L.J. "Effects of flaws and porosity on strength of adhesively-bonded joints", Quarterly Progress Report, No. 5, *Air Force Contract F33615-80-C-5092*, (1981)

[17] Romanko, J.; Jones, W. B. Jr., "Fatigue mechanisms in adhesively bonded joints", *Int Conf - Adhes and Adhes Sci, Technol and Appl*, Univ of Durham, Grey Coll, Engl, Sep 3-5 1980 Publ by the Plast and Rubber Inst, London, Engl, p. 11. 1, (1980)

[18] Reedy, E. D. Jr.; Guess, T. R., "Composite-to-metal tubular lap joints: Strength and fatigue resistance", *Wind Energy American Society of Mechanical Engineers, Solar Energy Division* (Publication) SED v 14 1993. Publ by ASME, New York, NY, USA. P. 189, (1993)

[19] Bassler, H.; El-Sebakhy, I.; and Malik, D.J., "Weldbonding of structure adhesives for body stiffening", *Worldwide Passenger Car Conference on Exposition*, Dearborn, MI, USA, Sept. 28 – Oct. 1 (1992)

[20] Imanaka, M.; Fukuchi, Y.; Kishimoto, W.; Okita, K.; Nakayama, H.; Nagai, H. (1988), "Fatigue life estimation of adhesively bonded lap joints", *Journal of Engineering Materials and Technology, Transactions of the ASME*, 110(4) p. 350, (1988)

[21] Romanko, J.; Jones, W. B. Jr., "Fatigue behavior of adhesively bonded joints", *Natl SAMPE Symp Exhib Proc 25th, The 1980's - Payoff Decade for Adv Mater*, San Diego, Calif, May 6-8 1980. Publ. by SAMPE (Sci. of Adv Mater and Process Eng Ser v 25), p. 154-166., (1980)

[22] Kim, N.E.; Griffin, J.H., "Special element approach for calculating the vibratory response of adhesively bonded and composite structures", *Journal of Sound and Vibration* v 170 n 3 Feb 24 1994. p. 377-395, (1994)

[23] Habib, M.; Aivazzadeh, S.; Verchery, G., "Analysis of adhesively bonded composite tubes under different loading conditions using axisymmetric interface finite elements", *American Society of Mechanical Engineers, Materials Division* (Publication) MD, 6. Publ by ASME, New York, NY, USA. p. 33-41, (1988)

[24] Roy, S.; Reddy, J. N., "Finite-element models of iscoelasticity and diffusion in adhesively bonded joints", *International Journal for Numerical Methods in Engineering* v 26 n 11 Nov 1988 p. 2531, (1988)

[25] Butkus, L.M., "Environmental durability of adhesively bonded joints", *Report of Air Force Inst Of Tech Wright-Pattersonafb, OH, AFIT-97-028D*, (1997)

[26] Ashcroft, I.A.; Digby, R.P.; Shaw, S.J., "A comparison of laboratory-conditioned and naturally-lathered bonded joints, Part I", *Journal of Adhesion*, **75**(2) p. 175, (2001)

[27] Ashcroft, I.A.; Digby, R.P.; Shaw, S.J., "A comparison of laboratory-conditioned and naturally-lathered bonded joints, Part II", *Journal of Adhesion* **75**(2) p. 201, (2001)

[28] Nishioka, T.; Atluri, S. N., "Analysis of cracks in adhesively bonded metallic laminates by a 3-dimensional assumed stress hybrid FEM", *Collect Tech Pap AIAA ASME ASCE AHS Struct Struct Dyn Mater Conf 22th Pt 1*, Atlanta, Ga, Apr 6-8 1981. Publ by AIAA (CP 811), New York, NY, 1981 Pap 81-0497 p. 66, (1981)

[29] Kyogoku, Hideki; Sugibayashi, Toshio; Ikegami, Kozo, "Strength evaluation of scarf joints bonded with adhesive resin", *JSME Int. J.*, **30**(265) p. 1052, (1987)

[30] Sancaktar, E.; Baldwin, J. F., "Experimental investigation of mixed-mode fracture in adhesively bonded joints", *Abstracts - Eighth Annual Meeting, The Adhesion Society*. Savannah, GA, USA ., Feb 24-27, 1985, Publ by Adhesion Soc, USA p. 24a-24b, (1985)

[31] Hufferd, William L., "Large deformation viscoelastic analysis of adhesive joints", *Abstracts - Eighth Annual Meeting, The Adhesion Society*, Savannah, GA, USA Feb 24-27, 1985, Publ by Adhesion Soc, USA p. 11a-11c, (1985)

[32] Johnson, W. S.; Mall, S., "Fracture mechanics approach for designing adhesively bonded joints", *Delamination and Debonding of Materials*, Pittsburgh, PA, USA, Nov 8-10, 1983, *ASTM Special Technical Publication*, Publ by ASTM, Philadelphia, PA, USA p. 189, (1985)

[33] Imanaka, M.; Nakayama, H.; Morikawa, K.; Nakamura, M., "Evaluation of fatigue life of adhesively bonded CFRP pipe/steel rod joints", *Composite Structures*, 31(3) p. 235, (1995)

[34] Turaga, U.V.R.S., and Sun, C.T., "An investigation of adhesive single-lap joints with attachments", *44th AIAA/ASME/ASCE/AHS/ASC Structures, Structural Dynamics & Materials Conference*, Norfolk, Virginia, 7-10 April 2003, AIAA Paper 2003-1957, (2003)

[35] Potter, K.D.; Guild, F.J.; Harvey, H.J.; Wisnom, M.R.; and Adams, R.D., "Understanding and control of adhesive crack propagation in bonded joints between carbon fiber composite adherends", *International Journal of Adhesion and Adhesive*, 21, p. 435, (2001)

[36] ZENG Q. and SUN C.T., "Fatigue performance of a bonded wavy composite lap joint", *Fatigue & Fracture of Engineering Materials & Structures*, 27(5), p. 413, (2004)

[37] Melograna J.D. and Grenestedt J.L., "Revisiting a Wavy Bonded Single Lap Joint", *AIAA Journal*, 42(2), p. 395, (2004)

[38] Potter, K.D.; Guild, F.J.; Harvey, H.J.; Wisnom, M.R.; Adams, R.D., "Understanding and control of adhesive crack propagation in bonded joints between carbon fiber composite adherends", *International Journal of Adhesion and Adhesive*, **21**, p. 435, (2001)

[39] Joyce, S.A. and Houston, J.E., "A new force sensor incorporating force-feedback control for interfacial force microscopy", *Rev. Sci. Instrum.* **62**(3), p. 710 (1991)

[40] Houston, J.E.; Winter, R.M., "Interfacial force microscopy: application to polymer surfaces", *American Chemical Society, Polymer Preprints, Division of Polymer Chemistry*, **41**(2), p. 1454 (2000)

[41] Pohlenz, F.; Herrmann, K.; Seemann, R.; Menelao, F., "Comparison of different hardness definitions usable for micro- and nanoindentation", *Zeitschrift fuer Metallkunde/Materials Research and Advanced Techniques*, **92**(9), p. 1031, (2001)

[42] Oliver, W.; Pharr, G. "An improved technique for determining hardness and elastic modulus using load and displacement sensing indentation experiments", *Journal of Material Research* **7**(6), p. 1564 (1992).

[43] Sneddon, I. N., "The relaxation between load and penetration in the axisymmetric Boussinesq problem for a punch of arbitrary profile", *International Journal of Engineering and Science*, **3**, p. 47, (1965)

[44] King, R., "Elastic analysis of some punch problems for a layered medium", *International Journal of Solids Structures* **23**(12), p.1657 (1987)

[45] VanLandingham, M. R.; Villarrubia ; Guthrie, W. F.; Meyers, G. F., "Nanoindentation of polymers: an overview", *Proceedings. 220th American Chemical Society National Meeting*, August 2000, Washington, DC. Macromolecular Symposia, Wiley-VCH Verlag GmbH, Tsukruk, V. V. and Spencer, N. D., Editors, p. 15, (2001)

[46] Smith, B.C., "How an FTIR works", Fourier Transform Infrared Spectroscopy, CRC Press, p.16, (1996)

[47] Anderson, D.H. and Wilson, T.E., "Novel approach to micro infrared sample preparation", *Analysis Chemistry* **47**, p. 2482 (1975)

[48] Cournoyer, R.; Shearer, J.C.; and Anderson, D.H., "Fourier Transform infrared analysis below the one-nanogram level", *Analysis Chemistry* **49**, p. 2275 (1977)

[49] Lacy, M.E., "Isolation and molecular identification of ultramicro contaminants by ft-ir spectroscopy", *In Fifth Contamination Control Conference*, (1979)

[50] Lacy, M.E., "Preparation of Ultraclean Gloves for Precision Assembly Operations"

Proceedings of the Institute of Environmental Science, (1982)

[51] Krishnan, K. and Hill, S.L., "FT-IR Microsampling Techniques", Practical Fourier

Transform Infrared Spectroscopy, Academic Press, Inc., P.104, (1990)

[52] Pinnavaia, T.J. and Beall, G., "Preface", Polymer-Clayer Nanocomposites, Wiley Series in Polymer Science, p. 1 (2000).

[53] Komori, Y. and Kuroda, K., "Layered silicate-polymer intercalation compounds", Polymer-Clayer Nanocomposites, Wiley Series in Polymer Science, p. 3 (2000).

[54] Lagaly, G.; Beneke, K., and Weiss, A., "Magadiite and H-magadiite. I. Sodium magadiite and some of its derivatives", *American Mineralogist*, **60**, p. 642 (1975).

[55] Lagaly, G.; Beneke, K., and Weiss, A., "Magadiite and H-magadiite. II. H-magadiite and its intercalation compounds", *American Mineralogist*, **60**, p. 650 (1975).

[56] Sugahara, Y.; Sugimoto, K.; Yanagisawa, T.; Nomizu, Y.; Kuroda, K.; and Kato, C., "The preparation of a magadiite-polyacrylonitrile intercalation compound and its conversion to silicon carbide", *Yogyo-Kyokai-Shi*, **95**, p. 117 (1987).

[57] Wang, Z.; Lan, T. and Pinnavaia, T., J. "Hybrid organic-inorganic nanocomposites formed from an epoxy polymer and layered silicic acid", *Chemistry of Materials*, **8**, p. 2200 (1996)

[58] Wang, Z. and Pinnavaia, T., J. "Hybrid organic-inorganic nanocomposites: exfoliation of magadiite nanolayers in an elastomeric epoxy polymer", *Chemistry of Materials*, **10**, 1820 (1998)

[59] Sugahara, Y.; Kitano, S.; Satokawa, S.; Kuroda, K.; and Kato, C., Synthesis of kaolinite-lactam intercalation compounds, *Bulletin of the Chemical Society of Japan*, **59**, p. 2607 (1986).

[60] Tunney, J.J. and Detellier, C. "Interlamellar amino functionalization of kaolinite", *Canadian Journal of Chemistry*, **75**, p. 1766 (1997)

[61] Seto, H.; Cruz, M.I. and Fripiat, "Long-range organization in the ammonium propionate intercalation complexes of kaolinite", *American Mineralogist*, **63**, p.572 (1978)

[62] Komori, Y.; Sugahara, Y. and Kuroda, K. "Direct intercalation of poly(vinylpyrrolidone) into kaolinite by refined guest displacement method", *Chemistry of Materials*, **11**, p. 3 (1999)

[63] Komori, Y.; Sugahara, Y. and Kuroda, "Intercalation of alkylamines and water into kaolinite with methanol kaolinite as an intermediate", *Applied clay Science*, **15**, p. 241 (1999)

[64] Komori, Y.; Matsumura, A.; Itagaki, T.; Sugahara, Y. and Kuroda, K., "Preparation of kaolinite- ϵ -caprolactam intercalation compound", *Applied clay Scienc.*, **11**, p. 47 (2000)

[65] Kuroda, K.; Hiraguri, K.; Komori, Y.; Sugahara, Y.; Mouri, H.; and Uesu, Y., "An acentric arrangement of p-nitroaniline molecules between the layers of kaolinite", *Chemical Communications*, **22**, p. 2253 (1999)

[66] Wang, M.S. and Pinnavaia, T.J., "Clay-Polymer Nanocomposites Formed from Acidic Derivatives of Montmorillonite and an Epoxy Resin", *Chemistry of Materials*, **6**, p.468 (1994)

[67] Lan, T and Pinnavaia, T. J., "Nanolayer Ordering in an Epoxy-Exfoliated Clay Hybrid Composite", *Materials Research Society Symp. Proc.*, **435**, p.79 (1996)

[68] Lan, T., Kaviratna, P.D. and Pinnavaia, T.J., "Epoxy self-polymerization in smectite clays", *Journal of Physics and Chemistry of Solids*, **57**, p. 1005 (1996)

[69] Lan, T.; Kaviratna, P.D. and Pinnavaia, T.J., "Mechanism of Clay Tactoid Exfoliation in Epoxy-Clay Nanocomposites", *Chemistry of Materials*, **7**, p. 2144 (1995)

[70] Wang, Z.; Lan, T.; and Pinnavaia, T.J., "Hybrid Organic-Inorganic Nanocomposites Formed from an Epoxy Polymer and a Layered Silicic Acid (Magadiite)", *Chemistry of Materials*, **8**, p. 2200 (1996)

[71] Shi, H.; Lan, T.; and Pinnavaia, T.J., "Interfacial Effects on the Reinforcement Properties of Polymer-Organoclay Nanocomposites" *Chemistry of Materials*, **8**, p. 1584 (1996)

[72] Tong, L.; Kuruppu M.; and Kelly, D., "Analysis of adhesively bonded composite double lap joints", *Journal of Thermoplastic Composite Materials*, **10**, p. 61 (1997)

[73] Broek, D, Elementary Engineering Fracture Mechanics, fourth revised edition, Martinus Nijhoff Publishers, p 85 (1986)

[74] Knowles, J.K. and Sternberg, E., "On a class of conservation laws in linearized and finite electrostatics", *Archive for Rational Mechanics and Analysis*, **44**, p 187 (1972)

[75] Pocius,A.V., Adhesion and Adhesives Technology: An Introduction, Hanser Gardner Publications Inc, p 1186, (2002)

[76] Baker,A.A., Bonded Repair of Aircraft Structures, Kluwer Academic Publishers, p 13-14, (1988)

[77] Simpson, G.J.; Sedin,D.L.; and Rowen, K.L., "Surface roughness by contact versus tapping mode atomic force microscopy", *Langmuir*, p 1429, (1999)

[78] Khanna, S.K.; Winter,R.M.; Ranganathan, P.; Yedla, S.B.; Kalukanimuttam, M.; and Paruchuri, K., "Sample Preparation Techniques for Nano-mechanical Characterization of Glass Fiber Reinforced Polyester Matrix Composites", *Composites: Part A* **34**, p 53–65 (2003)

[79] Wingard, C.D. and Beatty, C.L., "Cross linking of an Epoxy with a Mixed Amine as a Function of Stoichiometry. II. Final properties via Dynamic Mechanical Spectroscopy," *J. of Appl. Poly. Sci.*, 41 p 2539-2544 (1990)

[80] Vanlandingham,M.R.; Edulujee, R.F.; and Gillespie, J.W. Jr., "Relationships between Stoichiometry, Microstructure, and Properties of Amine Cured Epoxies", *Journal of Appl. poly. Sci.*, 71, pp 699-712, (1999).

[81] Chiang, C.H.; and Koenig, J. L. " Chemical Reactions Occurring at the Interface of Epoxy Matrix and Aminosilane Coupling Agents in Fiber Reinforced Composites" 35th Annual Technical Conference, Reinforced plastics/composites Institute, The Society of Plastic Industry,Inc, (1980)

[82] Cole, K.C.; Pilon,A.; Noel, D.; Hechler, J.J.; Chouliotis, A.; and Overbury, K.C. "Comparison of Infrared Spectroscopic Methods for the Quantitative Analysis of Epoxy Resins used in Carbon-Epoxy Composite Materials", *Applied Spectroscopy*, 42, 5, (1988).

[83] Liu, H. Investigation of Chemistry and Nano-mechanics at the Interface of Polymer Matrix – Glass Fiber Composites using FT-IR/EWS, AFM, and Interfacial Force Microscopy, PHD thesis, South Dakota School of Mines and Technology, Rapid City, (2002).

[84] Arvanitopoulos, C.D.; and Koenig,J.L. "Infrared Spectral Imaging of the Interphase of Epoxy-Glass Fiber-Reinforced Composites under Wet Conditions", *Applied Spectroscopy*, 50, 1, (1996).

[85] Hill, L.W. "Structure/property Relationships of Thermoset Coatings", *Journal of Coatings Technology*, 64, 808, pp 29-41, (1992).

[86] Southern Clay Products, Inc., "Cloisite ® 30B typical physical property bulletin",
<http://www.nanoclay.com/data/30B.htm>, (2004)

[87] Amethyst Galleries, Inc., "The mineral montmorillonite",
<http://mineral.galleries.com/minerals/silicate/montmori/montmori.htm>, (1995)

[88] Wang, Z.; Wang, H.; Cates, M., "Elastic properties of solid clays", *SEG Expanded Abstracts*, <http://www.seg.org/meetings/past/seg1998/techprog/rp3/papr1474.pdf>, (1998)

[89] Lai, W.M.; Rubin, D.; and Krempel E., "Young's modulus, Poisson's ratio, shear modulus, and bulk modulus", Introduction to Continuum Mechanics, Butterworth Heinemann, p. 229, (1993)

[90] Lagaly, G.; Beneke, K., and Weiss, "Magadiite and H-magadiite. I. Sodium magadiite and some of its derivatives", *A. Am. Miner.*, 60, p. 642 (1975).

[91] Lagaly, G.; Beneke, K., and Weiss , "Magadiite and H-magadiite. II. H-magadiite and its intercalation compounds", *A. Am. Miner.*, **60**, p. 650 (1975).

[92] Sugahara, Y.; Sugimoto, K.; Yanagisawa, T.; Nomizu, Y.; Kuroda, K.; and Kato, C., "The preparation of a magadiite-polyacrylonitrile intercalation compound and its conversion to silicon carbide", *Yogyo-Kyokai-Shi*, **95**, p. 117 (1987).

[93] Wang, Z.; Lan, T. and Pinnavaia, T., J. "Hybrid organic-inorganic nanocomposites formed from an epoxy polymer and layered silicic acid", *Chemistry of Materials*, **8**, p. 2200 (1996)

[94] Mallick, K.; Lake, M. S.; Arzberger, S. C.; Munshi, N.; and Paul, C., "Estimation of the elastic parameters of nanoclay-reinforced polymers using mean-field theory", *45th AIAA/ASME/ASCE/AHS/ASC Structures, Structural Dynamics & Materials Confer.*, 19-22 April, Palm Springs, California, AIAA 2004-1611, (2004)

[95] Mura, T., Micromechanics of Defects in Solids, Martinus Nijhoff, Boston, USA. (1982)

[96] Kunin, I. A., Elastic Media with Microstructure II, Springer Verlag, Berlin, Germany, (1983)

[97] Nemat-Nasser, S. and Horii, M., "Elastic Solids with Microdefects", in Micromechanics and Inhomogeneity – The Toshio Mura Anniversary Volume, Springer Verlag, New York, NY, p. 297- 320, (1990)

[98] Fredrickson, G. H. and Bicerano, J., "Barrier Properties of Oriented Disk composites", *Journal of Chemical Physics*, **110**(4), p. 2181-2188, (1999)

[99] Benveniste, Y., "A New Approach to the Application of Mori-Tanaka's Theory in Composite Materials", *Mechanics of Materials*, **6**, p. 147-157, (1987)

[100] Baptiste, D., "Damage Micromechanics Modelling of Discontinuous Reinforced Composites", in *Continuum Damage Mechanics of Materials and Structures*, O. Allix and F. Hild (editors), Elsevier Science Ltd., New York, USA, (2002)

[101] Chen, T.; Dvorak, G.J. and Benveniste, Y., "Mori-Tanaka Estimates of the Overall Elastic Moduli of Certain Composite Materials", *Journal of Applied Mechanics*, **59**, p.539-546, (1992)

[102] Lan, T. and Pinnavaia, T.J., "Clay-Reinforced Epoxy Nanocomposites", *Chemistry of Materials*, **6**, p 2216 (1994)

APPENDIX:

C⁺⁺ program for Iterative Solution of Accurate local Material Properties for Composites:

```
#include <iostream.h>

real Ei(a, b) //Function to give the initial value of modulus
{
Ei=a/b;
}

real vi(a, b, c, d, e, f, g) // Function to give the initial value of Poisson's ratio
{
vi=(a-b/c)/(-d/e-f/g);
}

real E(a, b, c, d, e, f, g, h) // Function to calculate modulus
{
E=a/(b+c*e/d+f*h/g);
}

real v(a, b, c, d, e, f, g, h) // Function to calculate Poisson's ratio
{
v=(a-b/c+d*e/f)/(-g/h);
}

int main()
{
real ssa11, ssa22, ssa33, sna11, sna22, sna33;
real ssb11, ssb22, ssb33, snb11, snb22, snb33;
real ssc11, ssc22, ssc33, snc11, snc22, snc33;
cout<<"Input stress11 stress22 stress33 strain11 strain22 strain33 of tensile load in x-
direction:"<<endl;
cin>>ssa11>>ssa22>>ssa33>>sna11>>sna22>>sna33;
cout<<"Input stress11 stress22 stress33 strain11 strain22 strain33 of tensile load in y-
direction:"<<endl;
cin>>ssb11>>ssb22>>ssb33>>snb11>>snb22>>snb33;
cout<<"Input stress11 stress22 stress33 strain11 strain22 strain33 of tensile load in z-
direction:"<<endl;
cin>>ssc11>>ssc22>>ssc33>>snc11>>snc22>>snc33;
real Modulus1(10);
real Modulus2(10);
real Modulus3(10);
real Poisson13(10);
real Poisson23(10);
```

real Poisson12(10);

```
int i; //To give the initial value and it is also the value of usual solution
i=0;
Modulus1(0)=Ei(ssa11, sna11);
Modulus2(0)=Ei(ssb22, snb22);
Modulus3(0)=Ei(ssc33, snc33);
Poisson13(0)=vi(snc11, ssc11, Modulus1(0), ssc22, Modulus2(0), ssc33, Modulus3(0));
Poisson23(0)=vi(snc22, ssc22, Modulus2(0), ssc11, Modulus1(0), ssc33, Modulus3(0));
Poisson12(0)=v(snb11, ssb11, Modulus1(0), Poisson13(0), ssb33, Modulus3(0), ssb22,
Modulus2(0));
cout<<"Modulus1("<<i<<")="<<Modulus1(i)<<endl;
cout<<"Modulus2("<<i<<")="<<Modulus2(i)<<endl;
cout<<"Modulus3("<<i<<")="<<Modulus3(i)<<endl;

do // Iterative loop, terminate when the changes of results are very small
{
i=i+1;
Modulus1(i)=E(ssa11, sna11, Poisson12(i-1), Modulus2(i-1), ssa22, Poisson23(i-1), Modulus3(i-
1), ssa33);
Modulus2(i)=E(ssb22, snb22, Poisson12(i-1), Modulus1(i-1), ssb11, Poisson23(i-1),
Modulus3(i-1), ssb33);
Modulus3(i)=E(ssc33, snc33, Poisson13(i-1), Modulus1(i-1), ssc11, Poisson23(i-1), Modulus2(i-
1), ssc22);
Poisson13(i)=v(snc11, ssc11, Modulus1(i), Poisson12(i-1), ssc22, Modulus2(i), ssc33,
Modulus3(i));
Poisson23(i)=v(snc22, ssc22, Modulus2(i), Poisson12(i-1), ssc11, Modulus1(i), ssc33,
Modulus3(i));
Poisson12(i)=v(snb11, ssb11, Modulus1(i), Poisson13(i), ssb33, Modulus3(i), ssb22,
Modulus2(i));
cout<<"Modulus1("<<i<<")="<<Modulus1(i)<<endl;
cout<<"Modulus2("<<i<<")="<<Modulus2(i)<<endl;
cout<<"Modulus3("<<i<<")="<<Modulus3(i)<<endl;
}
while ((Modulus1(i)-Modulus1(i-1)<1)|| (Modulus2(i)-Modulus2(i-1)<1)|| (Modulus3(i)-
Modulus3(i-1)<1)|| (Poisson13(i)-Poisson13(i-1)<0.001)|| (Poisson23(i)-Poisson23(i-
1)<0.001)|| (Poisson12(i)-Poisson12(i-1)<0.001));
return 0;
}
```